SP-1273

X-ray Evolving-Universe Spectroscopy

European Space Agency
Agence spatiale européenne

SP-1273
November 2003

X-ray Evolving-Universe Spectroscopy – The XEUS Instruments

European Space Agency
Agence spatiale européenne

Prepared by the XEUS Instrument Working Group:

Didier Barret, CESR Toulouse, France
Marcos Bavdaz, ESA/ESTEC, The Netherlands
Carl Budtz-Jorgensen, DSRI, Denmark
Enrico Costa, IASF, Italy
Lionel Duband, CEA/SBT, France
Piet de Korte, SRON, The Netherlands
Andrew Holland, Leicester University, UK
Peter Lechner, MPI Halbleiterlabor, Germany
David Lumb, ESA/ESTEC, The Netherlands
Arvind Parmar, ESA/ESTEC, The Netherlands
Luigi Piro, IASF, Italy
Lothar Struder, MPI Halbleiterlabor, Germany
Tadayuki Takahashi, ISAS, Japan
Peter Verhoeve, ESTEC, The Netherlands
Gabriele Villa, IASF, Italy

Previous reports in this XEUS series:

ESA SP-1238	The XEUS Science Case.	March 2000
ESA SP-1242	The XEUS Mission Summary.	May 2000
ESA SP-1253	The XEUS Telescope.	November 2001

Published by: ESA Publications Division
ESTEC, PO Box 299
2200 AG Noordwijk
The Netherlands
Editor: Andrew Wilson

ISBN: 92-9092-977-4
ISSN: 0379-6566
Printed in: The Netherlands
Price: €30

X-ray Evolving-Universe Spectroscopy - The XEUS Instruments

This report was compiled by the XEUS Instrument Working Group (IWG) in two phases. The report covers three baseline instruments: a Wide-Field Imager (WFI) for deep-survey pointed observations, and two Narrow-Field Instruments (NFI1 and 2) for follow-up observations with high efficiency and high spectral resolution. The cryogenics systems required for cooling these NFIs to sub-Kelvin temperatures are also described. The core document finishes with recommendations to ESA for the technology developments required for the mission.

During the XEUS 'Studying the Evolution of the Hot Universe' International Workshop at MPE Garching (D), 11-13 March 2002, the baseline focal plane for the mission received support from the scientific community. However, several instrumental additions to the focal plane were proposed in order to improve and broaden the scientific potential of the mission. After that workshop, the IWG membership was supplemented for a study of the auxiliary instrumentation proposed at the conference. This has resulted in the sections addressing enlargement of the WFI field of view, extension of the XEUS high-energy response via a high-energy X-ray imager, a dedicated sensor for high time-resolution studies with sub-ms timing on bright X-ray sources and a polarimeter for polarisation studies on a fairly large sample of bright sources.

On the basis of the original baseline document, ESA has raised funds to stimulate the technological developments required for the WFI, NFIs and their cooling. The development status of these instruments is promising, and no serious problems are foreseen in the development of the focal plane instrumentation if significant ESA and National funding can be kept in place in the coming years.

Contents

1 Introduction

XEUS, the X-ray Evolving Universe Spectroscopy mission, is a potential follow-on mission to the ESA XMM-Newton cornerstone observatory now in orbit. It was considered as part of ESA's Horizon 2000 plus programme within the context of the International Space Station (ISS). XEUS is the next logical step in X-ray astrophysics after the current set of great observatories (XMM-Newton and Chandra) complete their operational lives. However, the scientific objectives of XEUS are so demanding that the mission is clearly a major technological challenge. The development and ultimate success rely on a key breakthrough in the size of the optics delivered into orbit.

This report provides an initial study of the type of instruments required to achieve the primary mission goals and of their impacts on the overall design of the first detector spacecraft (DSC1). In addition, the recommendations of the XEUS International Workshop in Munich (March 2002) on focal plane instruments to achieve important secondary science objectives are considered.

1.1 Scope

This document provides an initial assessment of the possible types of instrumentation required to make up the focal plane assembly of DSC1, the rationale for a preliminary design specification for the focal plane and its impact at system level on the design of DSC1. It identifies three types of instruments and provides initial estimates of their evolution in terms of the performance capability, characteristics and resource requirements. A number of different types of instruments could have been considered but the three here reflect an initial assessment of possible instruments that may, with further development, achieve the performance required to meet the XEUS scientific objectives. This is therefore simply a possible model payload that can be used to scope the scientific capability of the XEUS mission as well as to establish initial requirements to be placed on the spacecraft.

The XEUS instrument performance requirements described in this report allow instrument developers to focus their efforts in specific areas tuned to the needs of XEUS, and to harness technological development and funds accordingly. In addition, it identifies a clear route to be travelled over the next few years, both for individual instrument development teams as well as National and Agency-based technological research development programmes. The report also identifies those areas of support technology that will have to be developed in parallel.

Finally, the report makes further suggestions for instrumentation to enhance the scientific potential of XEUS, but which does not specifically address the primary science goals. Similarly, identification of their resource requirements leads to higher confidence in the ability to implement the XEUS package in a cost-effective DSC configuration.

1.2 Scientific goals

The primary aim of XEUS is to study the astrophysics of some of the most distant and hence youngest known discrete objects in the Universe. The specific scientific issues are:

— to measure the spectra of objects with redshifts $z > 4$ at flux levels $< 10^{-18}$ erg cm^{-2} s^{-1}. This is 1000 times fainter than the sensitivity of XMM-Newton.
— to determine from the X-ray spectral lines the redshifts and thus ages of these very faint objects, which might not have easily identified optical counterparts.
— to establish the cosmological evolution of matter in the early Universe through the very clear means of heavy-element abundances as a function of redshift, i.e. the role of element evolution as the Universe aged through galaxy formation in the associated early stellar processes.

Based on these themes, important specific requirements for instrument performance can begin to be formed. The angular density of objects at high redshift drives the necessity for angular resolution of ~ 2 arcsec (HEW). The potential rarity of the exceptional high-z objects further requires a maximisation of the field of view. The phenomenon of star-forming galaxies particularly motivates good low-energy response. Conversely, the measurement of low-z obscured AGN with peaked spectral distributions at 20-50 keV demands an extension to higher energies.

The low-energy response will be important for leveraging studies of groups and clusters where the redshifting of oxygen emission lines requires high efficiency at 0.05-0.25 keV. Recent developments place a new emphasis on absorption spectroscopy. For example, low-density columns in O-lines and intense gamma-ray bursters (GRBs) acting as background light sources require velocity dispersion capability of < 2000 km s^{-1}, demanding 1 eV resolution.

Secondary science objectives should also be considered in terms of their requirements for instrument performance. Temporal resolution in the case of photon-limited observations scales with the mirror collecting area, so XEUS offers the best exploitation at sub-ms resolution. Likewise, polarimetric measurements need large collecting areas to extract the relatively small-polarised component. These two examples highlight the fact that the XEUS mirror area uniquely addresses some science issues, so it is important to examine the accommodation of those instrument technologies.

The primary science objectives are detailed in the companion report from the XEUS Science Advisory Committee (ESA SP-1238, 2000). The secondary science objectives are briefly addressed in this report, together with the secondary instrumentation.

1.3 Mission profile

The overall mission scenario is summarised in Fig. 1.1. XEUS employs two

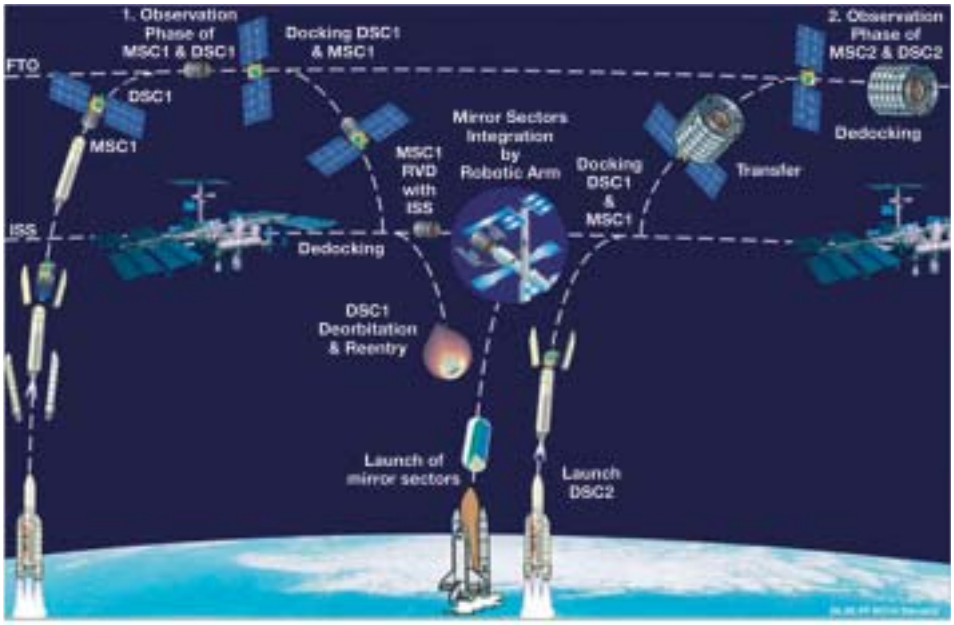

Figure 1.1. The XEUS mission profile shows the various mission phases and interfaces with the ISS.

free-flying satellites: a mirror spacecraft (MSC) and a detector spacecraft (DSC), separated by 50 m and aligned by an active orbit control and alignment system. In the baseline mission scenario, the required large-aperture mirror cannot be deployed in a single launch. It is envisaged to launch an initial 'zero-growth' XEUS mated pair (MSC1 + DSC1) directly into a fellow traveller orbit (FTO) to the ISS using an Ariane-5 or similar vehicle. The FTO is a low Earth orbit (altitude ~ 600 km) with an inclination similar to that of the ISS. The mated pair will decouple in FTO and DSC1 will take up station 50 m from MSC1. After alignment, validation and standard spacecraft and payload checkout, the initial 4-year astrophysics observation programme with this zero-growth XEUS will begin. MSC1 will point at given target fields, maintaining a stable attitude, while DSC1 sits at the focal distance aligned so that the field image on the detectors remains stable.

It must be stressed that XEUS in this scenario is completely autonomous from the ISS. In this initial configuration, MSC1 will contain only the inner core of the final mirror. The XEUS mirror collecting area at this point is already very large (~ 6 m^2 and 3 m^2 at 1 keV and 8 keV, respectively) but with substantial room for growth through the use of the ISS. This growth capability is crucial for the ultimate mission science objectives of studying high-redshift spectra in detail.

The pair of XEUS spacecraft can remate in orbit and, using the orbit control system (OCS) of DSC1, approach the ISS. At this stage, the mated pair can

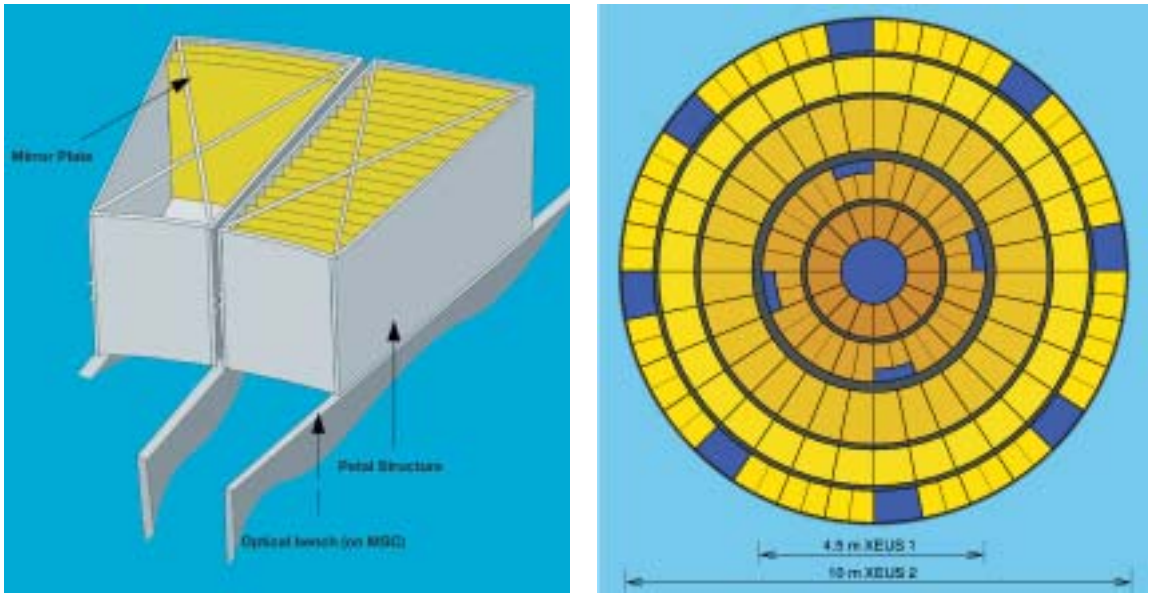

Figure 1.2. A pair of XEUS mirror petals (left) and the overall distribution of the petals across the aperture in the case of the fully-grown mirror MSC2 (right). The inner core MSC1 is also indicated.

wait for up to a year, following the ISS at a safe distance, until the Station is ready to receive MSC1 for refurbishment and mirror growth. DSC1 will separate to leave MSC1 to make the approach and docking at the ISS. DSC1 will then undergo a controlled reentry. The main activities at the ISS are:

— adding eight new mirror sectors to form the expanded fully-grown MSC2;
— adding thermal baffles to MSC2;
— performing checkout of MSC2;
— undocking MSC2 from the ISS;
— transferring MSC2 to FTO.

After MSC2 arrives in its FTO, DSC2 is launched directly to MSC2 and the fully-grown XEUS starts its 'high-redshift Universe' observation programme. The mirror area after growth at the ISS is huge (~ 30 m^2 and 3 m^2 at 1 keV and 8 keV, respectively). The growth is at exactly those energies (< 2 keV) where radiation from objects at high redshift will appear in the observed frame.

It is the objective of this report to establish a baseline payload of instruments for DSC1 in order to ensure a realistic and detailed system study for the initial mission configuration of MSC1 + DSC1.

1.4 The XEUS mirror

To achieve these demanding broad scientific aims, a large X-ray mirror needs to be developed. The basic mirror requirement is:

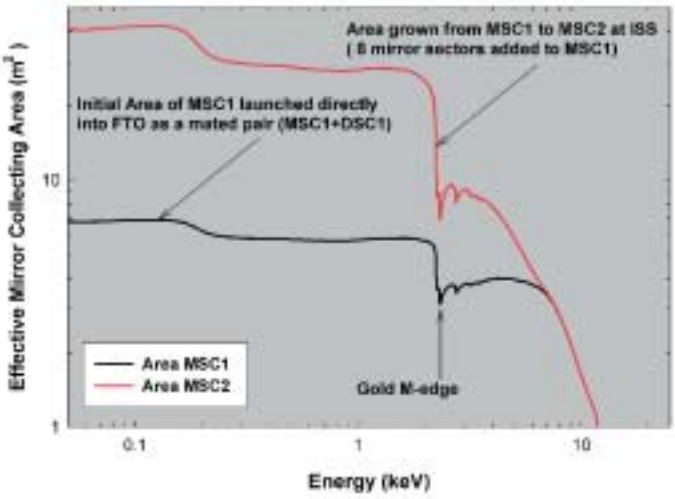

Figure 1.3. The effective area of the XEUS mirror in the initial (MSC1) and final (MSC2) configurations as a function of X-ray photon energy. Note the significant increase in area below ~ 2 keV after the growth of MSC at the ISS. This energy range is key to the exploration of the very high-redshift early Universe.

— a collecting area of 30 m^2 and 3 m^2 at 1 keV and 8 keV, respectively;
— a spatial resolution of < 5 arcsec (HEW), with a goal of 2 arcsec;
— a field of view of ~ 5 arcmin (Section 2);
— an energy range of 0.05-30 keV.

These requirements could possibly be achieved by capitalising on the successful XMM-Newton mirror replication technology. Unlike that mission, however, where a heavily nested Wolter I X-ray mirror was fabricated from closed shells, the XEUS mirror aperture of 10 m diameter is divided into annuli, with each annulus subdivided into sectors. Just as in XMM-Newton, which was based on electroforming nickel technology, the mass requirements of the mirror system both for MSC1 and the individual sectors of MSC2 are a core issue. The replication technology therefore needs to consider not only the difficult optical performance requirements but also a rather low-mass approach. The basic mirror unit consists of a set of heavily stacked thin mirror plates, each retaining the correct Wolter I geometry. This unit is known as a mirror petal and is a complete free-standing calibrated part of the overall XEUS mirror (Fig. 1.2). Each petal has its own set of control motors, so that the overall system can be aligned to an optimum focus.

The effective area of such a mirror system both in its initial (MSC1) and final fully-grown (MSC2) configuration is shown in Fig. 1.3 as a function of photon energy.

Subsequent to the baseline mirror studies described in the Telescope Working Group report (ESA SP-1253, 2001), additional activities have studied the enhancement of the mirror effective area for energies between

10 keV and 100 keV. The inner petals could be coated with graded layers of, for example, platinum and carbon, producing an enhanced effective area of 2000 cm^2 at 30 keV, and relatively flat response to 80 keV or 90 keV. While the effective field of view is not modified at the lower energies, at 90 keV it is limited by the grazing angle to ~ 3 arcmin. Substantial development work is necessary to confirm if such 'super-mirrors' can be implemented without degrading the imaging quality of the underlying mirrors. Nevertheless, such techniques open up the possibility for a large increase in energy dynamic range of the XEUS optics, and the corresponding detector requirements must be addressed.

1.5 The XEUS detector spacecraft

The detector spacecraft (DSC1 or 2) must perform a number of crucial tasks, of which the first is tracking the focus of the MSC X-ray telescope to ±2 mm. This implies that DSC will fly in a non-Keplerian orbit. The orbital characteristics of this MSC-DSC tandem pair are:

Parameter	*Specification*
Altitude (km)	600
Eccentricity	0
Inclination (deg)	51.6
Period (min)	97
Maximum eclipse (min)	35.5
Node spacing (deg)	24
Node precession (deg day^{-1})	–4.5
De-orbit ΔV (m s^{-1})	256
Altitude change ΔV (m s^{-1} km^{-1})	0.54
Plane change ΔV (m s^{-1} deg^{-1})	132
Earth angular radius (deg)	66
Range to horizon (km)	2831

These characteristics refer to the nominal mission start, with XEUS inserted directly into FTO. This orbit will naturally decay with a mean and maximum orbit rate of 0.55 km yr^{-1} and 4.7 km yr^{-1}, respectively. DSC1 will fly in a similar orbit but shifted by 50 m against the pointing direction of XEUS and MSC1. The peak forces required to keep the DSC on station in this orbit depend on the angle β between the XEUS orbital plane and the XEUS pointing direction, with the smallest force being required for the largest β. For $0 < \beta < 90^o$, the average force is 235-360 mN, requiring a ΔV of ~ 0.5-0.3 m s^{-1} per orbit. Thus observations at high declinations will require less propellant. All other forces acting on the DSC are about two orders of magnitude lower than the non-Keplerian orbit forces. These other forces can be compensated for by the DSC orbital control system. The requirements with respect to the DSC orbit control system based on the average of the forces discussed above are:

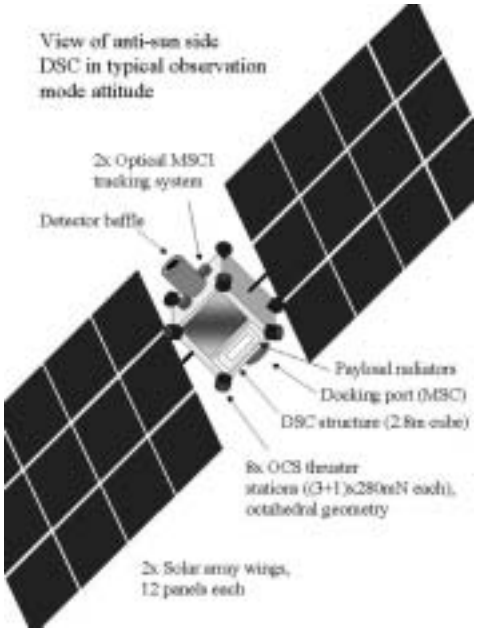

Figure 1.4. XEUS detector spacecraft DSC1.

Parameter	*Specification*
DSC1 mass (kg)	4000
Peak forces (worst-case)	468 mN
Average ΔV over 1 orbit	0.45 m s^{-1}
Average ΔV over 1 day	6.7 m s^{-1}
DSC FTO to ISS ΔV	111 m s^{-1}

Stationary plasma thrusters (SPTs) will provide the force to keep the DSC in its orbit. These thrusters must be distributed such that the thrust axis distribution is as isotropic as possible in order to minimise thruster power and propellant requirements. This need arises from the orbital inclination and its precession coupled to the different pointing directions required by XEUS. This leads to constantly changing forces around the orbit. Issues related to the lifetime, cycle times and thrust control as well as the dynamic range are important for thruster selection. Typically, the mass of xenon propellant used by these thrusters is significant, of the order ~ 1000 kg yr^{-1}.

Figure 1.4 shows a perspective view of DSC1 looking at the anti-solar side, which shows the instrument thermal radiators. Solar panels are sized for the DSC power requirements and are shown in Fig. 1.4 for the case when XEUS is pointing at a low-declination target, i.e. the array is tilted 120º from the XEUS optical axis. The solar array is always kept perpendicular to the Sun. DSC1 is a ~ 2.5 m cube supporting deployable solar arrays spanning 20 m and with a width of ~ 7.5 m. DSC dry mass is estimated to be ~ 2600 kg. Excluding the power for the propulsion unit, it requires ~ 1 kW during the periods of observation. The power requirements of the propulsion system will depend on the thruster configuration , but is estimated to be a maximum, for the worst case during eclipse, ~ 10 kW.

1.6 Overview of the focal plane instruments

The XEUS DSC1 focal plane is shared by three primary instruments:

— a wide-field broadband imaging medium-resolution spectrometer (WFI) based on a silicon semiconductor detector. Spectral resolution is 20-290 eV for the 0.05-30 keV energy range. The baseline instrument covers a field of 5 arcmin;
— a narrow-field imaging spectrometer (NFI1) optimised for the energy band 0.05-3 keV, but having some response (10% efficiency) up to ~ 7 keV. FWHM energy resolution is 2 eV at 1 keV;
— a narrow-field imaging spectrometer (NFI2) optimised for the energy band 1-7 keV (90% efficiency) but with good response up to 15 keV. FWHM energy resolution of 5 eV at 7 keV.

The basic strategy for the XEUS core science is to use the narrow-field instruments to obtain follow-up high-resolution spectra of objects detected by the wide-field instrument. The energy resolutions for the narrow-field instruments is a few eV, while the field of view is restricted to ~ 30 arcsec. The WFI instrument should, from its broadband spectra or colour indices, allow XEUS to identify those candidates that may be at high redshift.

An important output of the accommodation studies will be to define if parallel survey science can be achieved by operating the imaging camera while a spectrometer is measuring an on-axis target. This depends not only on available operating resources of the spacecraft, but also on the ability to collocate the separate detectors physically within an acceptable distance of the nominal telescope axis.

The instrument complement that has been considered to address important ancillary science goals include:

— a fast timing instrument based on a silicon drift detector to provide spectrally-resolved counting information for point sources, at Mcount s^{-1} rates. This instrument will enable tests of general relativity in the strong field regime through observations of the brightest X-ray sources in the sky (X-ray transients and bursters).
— a hard X-ray detector co-axially aligned with the on-axis imaging instrument. This should offer a modest spectral resolution over the core of the field of view in order to support the identification and analysis of extremely obscured or hard spectral objects, to identify the sources contributing to the peak of the cosmic diffuse background spectral power, and to measure spectral features such as cyclotron lines. It would be implemented as a compound semiconductor detector pixel-array located behind the WFI.
— an enhanced wide-field instrument, to increase the field of view of the baseline imager in order to maximise the survey potential for locating the most extreme objects in the high-redshift Universe. A doubling of the number of sources detectable at high redshift is anticipated using an array of more conventional CCDs located around the on-axis imager.

— a polarisation detector is considered, comprising a micropattern gas chamber to sense the photoelectric polarisation effect. Polarisation measurements are the last of the traditional astronomical tools that have not yet been significantly employed in X-ray astronomy.

1.7 The cooling strategy

XEUS has a long overall mission duration, with access to the DSC or replacement of DSCs assumed to be every 4-5 years. The basic thermal concept for XEUS is therefore not to provide cooling through normal cryogenic consumables such as liquid helium or liquid nitrogen but rather to ensure that the technology is developed for autonomous closed cycle operation. This crucial issue is addressed in Sections 6 and 8.

For DSC1, the XEUS focal plane detectors have very different cooling requirements. The wide-field instrument requires a temperature of ~ 200K, which can be achieved passively with a radiator and Peltier cooler. For the narrow-field instruments, the base temperatures are below 1K, thus requiring a mechanical cooler stage to achieve a base temperature of 2.5K followed by further stages such as a closed ^{3}He sorption cooler (0.3K) and an adiabatic demagnetising refrigerator (ADR) to provide the second sub-Kelvin capability (20-35mK).

2 Core Science and Focal Plane Choice

2.1 Introduction

The specific science goals addressed in the XEUS Science Case document (ESA SP-1238, March 2000) demand the development of a large X-ray telescope. The basic top-level features of this telescope are:

— an X-ray mirror with an effective collecting area at 1 keV of 30 m^2 in its final configuration (MSC2);
— the spatial resolution of the mirror needs to be ~ 2-5 arcsec (HEW; a goal of 2 arcsec at 1 keV is specified) in order to avoid source confusion at these faint flux levels;
— an energy resolution of 1-10 eV is required to measure the spectral lines, line cores and line profiles from specific sources in order to determine the redshift as well as the physics associated with the emission mechanism.

In addition to the core science objectives, considerable auxiliary science will be performed on selected field sources. In general, these sources will be much brighter, thereby placing significant further constraints on the count rate requirements of the various instruments.

Based on these broad technical requirements, a three-instrument focal plane package is considered:

— a wide-field broadband imaging solid-state camera (WFI) covering the complete field of view and energy range, while adequately sampling the mirror point spread function (PSF). This instrument combines a high imaging sensitivity with modest broadband spectral resolution. This instrument is primarily used to make extremely deep surveys (10^{-18}-10^{-19} erg cm^{-2} s^{-1}), thereby positioning sources and measuring their broadband medium-resolution spectra, or at least giving an estimate of their colour indices.

— two narrow-field high-resolution imaging spectrometers (NFI1/2) that focus on the soft and medium X-ray bands respectively, and are used as follow-up spectrometers on specific sources. Two types of NFI detectors are considered here and are based on rather different technologies: the superconducting tunnel junction (STJ) and the transition edge sensor (TES). Given the large dynamic energy range required for the XEUS science, two NFIs are necessary in order to meet the few eV energy resolution requirement with high efficiency over the complete energy band. NFI1, based on STJ technology, will be optimised below 2 keV. NFI2, based on TES technology, will be optimised above 1 keV, so that there is significant overlap in the intermediate energy range.

The overall characteristics of these instruments are:

Parameter	*WFI*	*NFI1*	*NFI2*
Detector type	Active Pixel DEPFET	STJ	TES
Field Coverage	5 arcmin	30 arcsec	32 arcsec
Number of pixels	1000 x 1000	48 x 48 (option 1 of 3)	32 x 32
Pixel size (arcsec)	0.3	0.6	1
Energy resolution (eV)	125 eV	3 (< 1) eV	2 & 5 eV
	@ 6 keV	@ 1 keV	@ 1 & 8 keV
Detection efficiency (%)	100% @ 6 keV	90% @ 1 keV	>90% @ 6 keV
Time resolution	< 5 ms	< 5 μs (< 1 ms)	< 5 μs
Count rate limit	200-1000 Hz/PSF	25000 Hz/PSF	250 Hz/PSF
Operating temperature	180 (210) K	300 (30) mK	35 (20) mK

( ) option to be decided during technology demonstration phase

2.2 Field of view and focal length

The focal length for the XEUS telescope has been chosen as 50 m. The rationale for this choice is:

— the response at 1 keV must be maximised and matched to the diameter of the optics (~ 10 m). This diameter is itself based on a number of mission-specific considerations, such as launcher envelope and mirror expansion logistics, as well as the key scientific requirement to derive spectra of sources as faint as 10^{-18} erg cm^{-2} s^{-1}.
— the DSC-MSC alignment maintenance budgets are not over-stringent and can be achieved with current technology.
— with this diameter, the field of view for the WFI is taken to be ~5 arcmin, based on arguments that the long focal length implies a relatively flat point spread function over a field up to 10 arcmin in diameter, as well as a decrease in area that is only modest over such an angular scale.
— the WFI could achieve a size of order 10 cm with a development of the envisaged silicon-based semiconductor detector technology, comprising a 2 x 2 mosaic of the baseline camera.
— the XEUS mission operates in a unique mode in which it is sensitive to stray light because there is no structure linking the mirror to the focal plane. This means that the mirror and detector spacecraft rely on very effective baffling at the unit level. A narrower field would therefore be important for reducing the stray light.
— the minimum field of view for the NFI instruments (~ 30 arcsec) is based on the specification for the spacecraft attitude and orbit control system (AOCS) together with a reasonable extrapolation of the future development of the size of the NFI detectors (~ 7 mm for a focal length of 50 m).

As a result of these issues, a field of view of ~ 5 arcmin was considered to be reasonable at this stage in the XEUS definition. This also allows comparison of the XEUS deep fields with optical fields such as HST (HDF-N & -S), Chandra (CDF-S), SIRTF (GOODS) and JWST. Extension of this field by tiling additional areas with, for example, MOS CCD detectors placed around the DEPFET array is also considered, in order to maximise the survey area

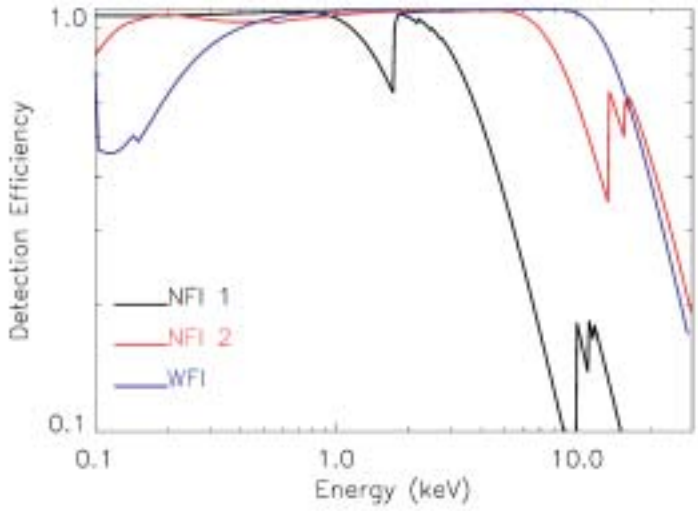

Figure 2.1. The efficiencies of WFI, NFI1 and NFI2 as functions of photon energy. No filters or mirror efficiencies are included in this figure.

for detecting the rare or extreme objects. This field coverage issue is clearly major and requires considerable study as the system-level design matures. A related topic is the effect of stray light, both X-ray and optical. Given the lack of a conventional closed optical bench, the potential for contamination by off-axis sources of radiation is severe, and must be addressed in detail.

2.3 Energy range and efficiency

The focal length of the XEUS mirror provides an energy range from the Extreme-UV (XUV) (40 m^2 at 100 eV) up to quite hard X-ray energies (100 cm^2 at 20 keV).

The low-energy response is constrained by the need to be able to detect helium-like oxygen emission and the Fe-L complex out to significant redshifts. Naturally, this also has to be considered in conjunction with the absorption introduced by the interstellar medium. However, to detect an O VII line out to a redshift of 3 would require a response down to ~ 150 eV. In addition, to ensure a good estimate of the continuum emission at energies below this redshifted line, the low-energy response needs to be at least down to 100 eV and possibly as low as ~ 50 eV.

The high-energy response is constrained by the requirements to model accurately the continuum of sources at energies well above that required for ionised iron emission (> 7 keV). Since there is considerable telescope area at energies up to 20 keV, as a result of the inner shells of the XEUS mirror and the long focal length, the upper energy response has been fixed at ~ 30 keV. This will therefore provide adequate spectral coverage for the lower z and brighter field sources.

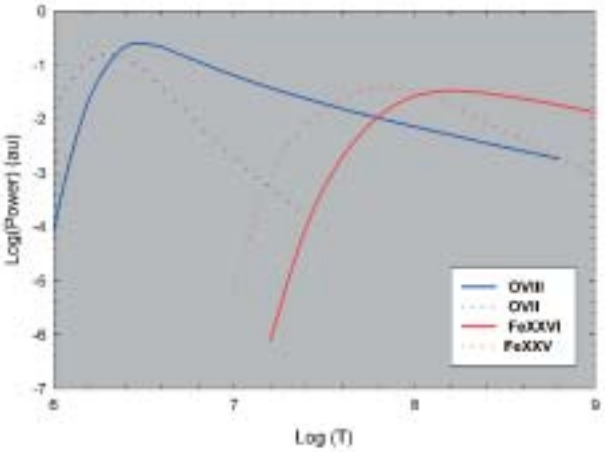

Figure 2.2. The relative intensities of some of the principal transitions from highly ionised oxygen and iron as a function of plasma electron temperature.

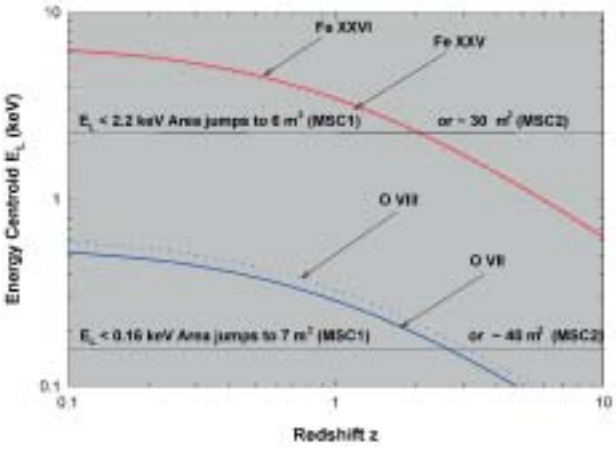

Figure 2.3. The energy centroids of the helium and hydrogenic ions of oxygen and iron as a function of redshift.

Given the energy range of 0.05-30 keV, it was considered that no detector could cover effectively the complete band and the field of view while achieving a high spectral resolution. Efficient field coverage and moderate energy resolution over the full energy band can be obtained using the WFI, although the low-energy response is currently limited to ~ 100 eV. This lower energy limit is an obvious development area, and is discussed in Section 3. To ensure adequately efficient high spectroscopic performance, the two narrow-field instruments are optimised to cover two overlapping energy bands, albeit with a restricted field. NFI1 will cover 0.05-3 keV, while NFI2 will cover 0.5-7 keV. NFI2 should have some response up to 15 keV, albeit with a poorer energy resolution.

2.4 Energy resolution

High-temperature plasmas, $T > 10^6$K, radiate their energy in the X-ray band. At temperatures below 10^7K, the bulk of this emission is in the form of collisionally excited emission lines from the most abundant elements such as helium-like oxygen (O VII) at ~ 600 eV and emission from iron ions (Fe XXIV and below) at ~ 1 keV. At temperatures above 10^7K, a significant fraction of the emission is continuum radiation, although particularly strong hydrogenic and helium-like lines are present from Si (1.8 keV), S (2.4 keV) and Fe (6.7 keV).

Figure 2.2 shows the variation of the relative line strengths of some of the key ions, as a function of temperature, in an optically thin plasma. In this case, cosmic abundances were assumed. The energy centroid of these important hot plasma diagnostic ions as a function of redshift is shown in Fig. 2.3.

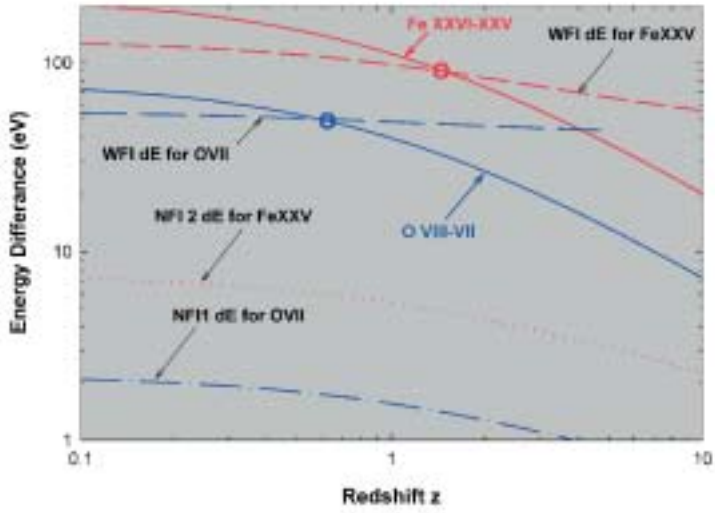

Figure 2.4. The energy differences between the centroids of the helium and hydrogenic ions of oxygen and iron as functions of redshift. The resolution of the three instruments to their lines and their limits are indicated.

Figure 2.4 shows the variation of the energy difference between a hydrogenic and helium-like resonance transition from iron and oxygen as a function of redshift. The medium-energy resolution required for XEUS is based on the requirement to resolve emission lines of helium-like iron and oxygen from hydrogenic species of the same elements or with lines arising from fluorescent emission from cooler material. Such a requirement can be satisfied in general by conventional silicon-based devices such as the WFI out to a redshift of $z \sim 1$. Beyond this redshift, the line cannot be resolved or uniquely identified without recourse to one of the NFI instruments.

Although the intensities of the hydrogenic and helium-like lines from the same element are an important ion temperature indicator, the ability to resolve the helium-like triplets of the most abundant elements in a simple single-temperature optically thin plasma allows the derivation of the key characteristics of the emitting plasma in a model-independent manner. High-resolution spectroscopy provides the ability to determine the electron and ion temperatures, the electron density and the relative abundance of the elements, as well as to establish the degree of thermal and ionisation equilibrium. So the resolution of the NFI spectrometers needs to resolve the resonance, forbidden and intercombination lines of the He-like triplets from the most abundant elements. The principal line transitions of the most abundant helium-like lines are:

Element	*$1s^2 - 1s2p^1P$ (R)*	*$1s2 - 1s^2p^3P$ (I)*	*R-I (keV)*	*$1s^2 - 1s2s^3S$ (F)*	*I-F (keV)*
Iron	6.702	6.669	0.033	6.641	0.028
Sulphur	2.460	2.447	0.013	2.431	0.016
Silicon	1.864	1.853	0.011	1.840	0.013
Oxygen	0.574	0.569	0.005	0.561	0.008

R: resonance line; I: intercombination line; F: forbidden line transition. All line energies in keV.

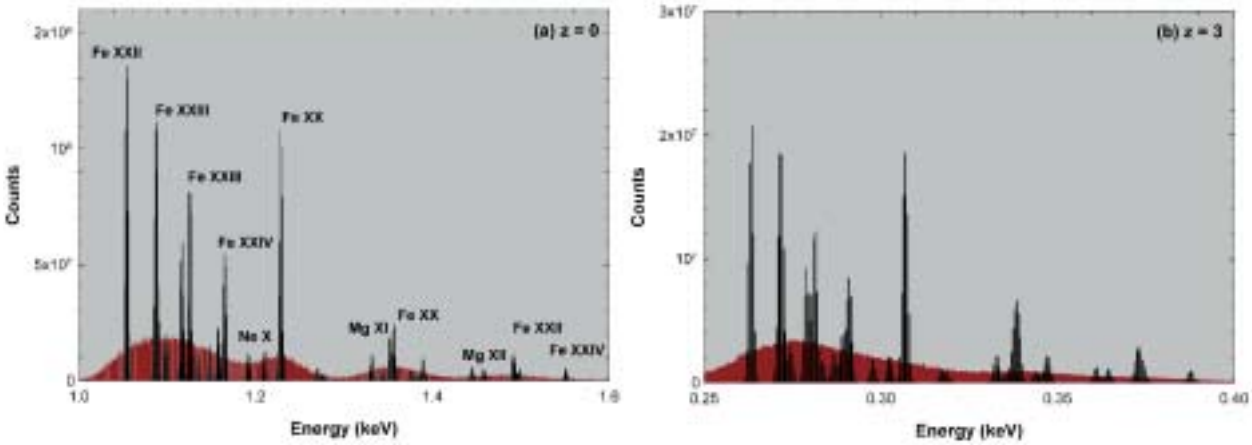

Figure 2.5. The simulated response of NFI1 to the Fe-L complex of lines around 1 keV from a hot optically thin plasma at a temperature of 10^7K, for the case when the redshift changes from (a) $z = 0$ to (b) $z = 3$. The WFI response is also shown for comparison. NFI1 was assumed to have a tunnel-limited resolution based on a tantalum STJ, while WFI was taken as Fano-limited. At a redshift of 3, no line complexes are resolvable with the WFI over this energy range from a 10^7K plasma.

Adequate separation requires a resolution of about 2 eV for oxygen and 10 eV for iron. However, dielectronic and inner-shell satellite lines very close to the lines of the triplet can be resolved only by an appreciably higher resolution.

In addition, sufficient resolution is required to resolve the multitude of lines within the Fe-L complex around 1 keV from a hot plasma. To illustrate these cases, Fig. 2.5 shows the response of the proposed NFI1 instrument, based on tantalum STJs, to the large number of lines from the Fe-L complex, expected to be radiated by an optically thin plasma at a single temperature of 10^7K. For comparison, the response of WFI is also shown. In this example, solar abundances and ionisation equilibrium were assumed and, for clarity, the continuum emission has been suppressed. Here we show the relative line intensities (arbitrary units) that include the detector efficiency and the mirror collecting area for MSC1 coupled to DSC1 (the initial focal plane instrument package) as a function of X-ray photon energy. The intensity and associated energy shift of these lines owing to the effect of redshift is shown for the cases where z is 0 and 3. Clearly, from Fig. 2.5, the majority of lines are easily resolvable with such an NFI instrument, allowing (assuming a single-temperature optically thin plasma), through the measurement of the relative intensity of the lines from the same ion, the temperature to be uniquely determined. In addition, through the relative intensity of lines from different elements, such as Fe and Ne, the relative abundances can be established. The intensity ratio of resonance lines from different ions of the same element together with line centroids allows the degree of ionisation equilibrium to be deduced, as well as the distance to the object through the determination of the redshift. A high spectral resolution is required for such observations. This can be achieved using either one of the two proposed XEUS narrow-field instruments, depending on source conditions and

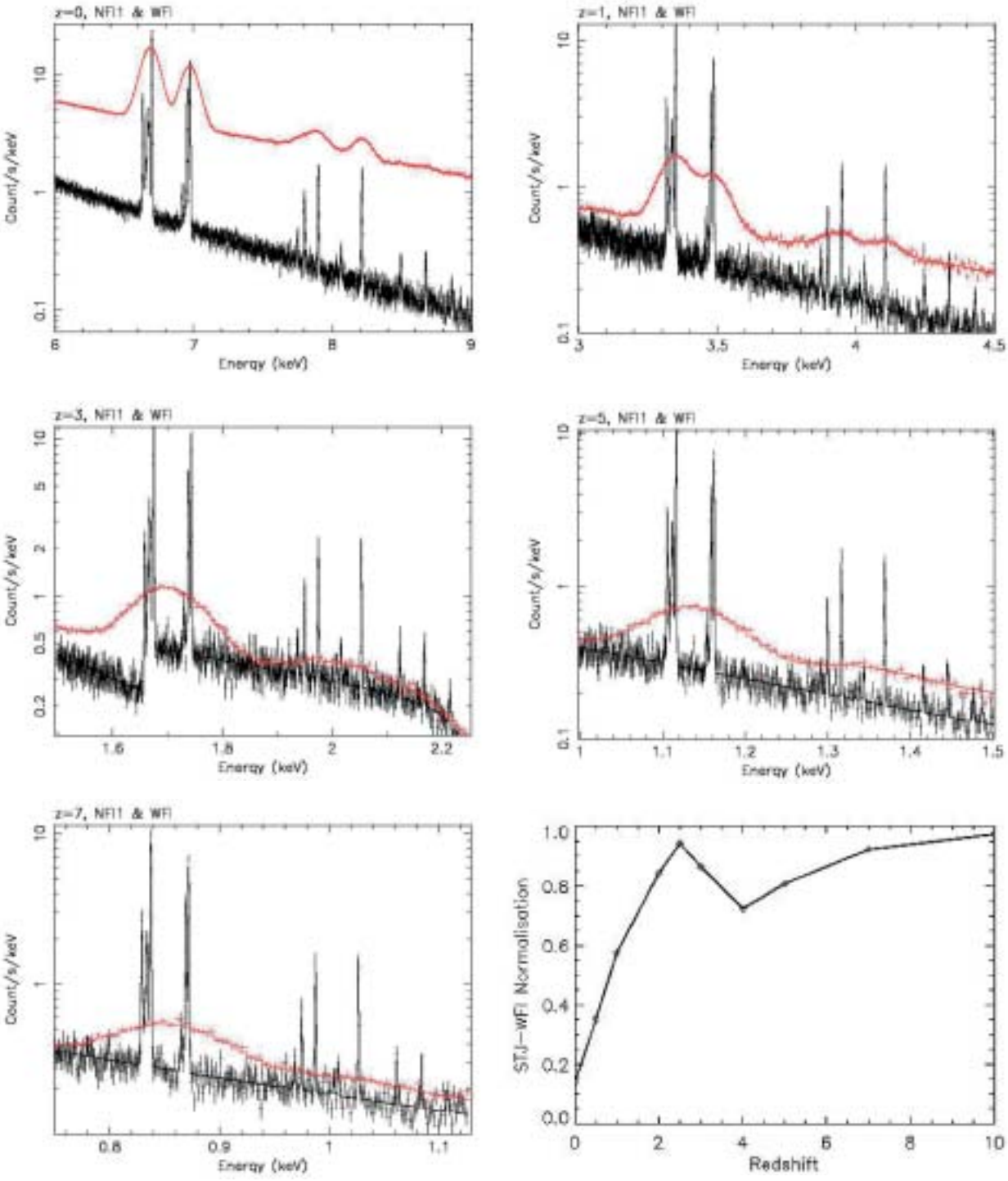

Figure 2.6. The response of NFI1 (black), a tunnel-limited Ta-based STJ, to the iron lines around 6-9 keV (rest frame) from an optically thin plasma with solar abundances having a temperature of ~ 10^8K. Comparison with WFI response (red) for redshifts of 0, 1, 3, 5 and 7.

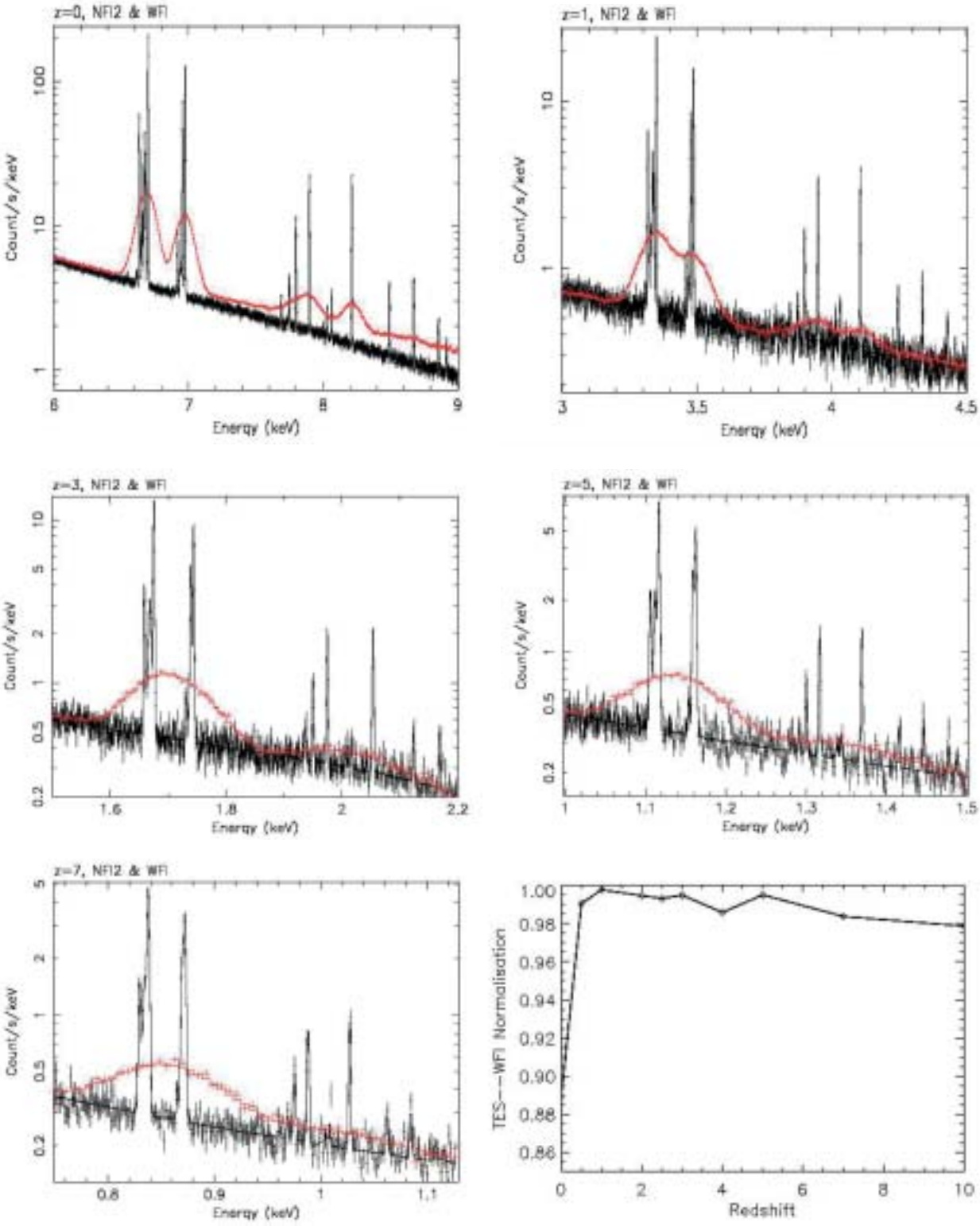

Figure 2.7. The response of NFI2 (black; a bismuth absorber TES) compared with WFI response (red) for redshifts of 0, 1, 3, 5 and 7. In contrast with NFI1, the higher sensitivity of NFI2 matches WFI for all redshifts, although the worse energy resolution at the lowest energies prevents the resolution of the hydrogenic triplet at the highest redshifts.

redshift, but it is impossible with conventional solid-state devices such as WFI. The solid-state semiconductor-based spectrometer (WFI) does, however, provide both the full-field coverage essential for XEUS and the overall spectrum (and possibly an estimate of the redshift) for all the deep-field sources detected before their detailed study by the NFI instruments.

Figures 2.6 and 2.7 show the response of NFI1 and NFI2 (compared with WFI) to the Fe-K lines at 6-9 keV in the rest frame (the helium and hydrogenic Kα and Kβ lines including the various satellite lines) for the case of a plasma temperature of ~ 10^8K in a source of luminosity 2 x 10^{45} erg s^{-1} (e.g. a bright cluster). They account for intensity changes via the luminosity distance scaling in a concordance cosmology, though without a cluster luminosity evolution.

NFI1 resolves all of these lines (including the satellite lines) out to all redshifts. By $z > 3$ the Fano-limited WFI cannot resolve the helium line complex from that of the hydrogenic line. In fact, with a suitable value of noise included for WFI, this redshift limit is more like $z > 1.5$ (Fig. 2.4). The last panel shows rates of the NFI to WFI total counts observed in these lines at 6-9 keV as a function of redshift. Note how, as the redshift increases, the actual peak counts in the line complexes as observed by NFI1 maintain a roughly constant value as the powerful low energy response of the mirror system compensates. This compensation is further assisted by the efficiency of the NFI1 detector at low energies. The WFI clearly finds it difficult to resolve the He-H Kα lines as the redshift increases beyond 1.

2.5 Position resolution

The spatial resolution of the detectors is based on the need to over-sample the mirror PSF, assumed to be the goal resolution of ~ 2 arcsec (HEW). This means that the spatial resolution of any detector must be below 480 mm. In the case of WFI, the over-sampling of the PSF is ~ 5; for NFI1 & 2 it is ~ 3 and ~ 2, respectively.

2.6 Count rate limits and time resolution

The required time resolution is governed by the auxiliary field source science. A source with a typical flux of $Fx \sim 10^{-14}$ erg cm^{-2} s^{-1} will lead to a photon flux of ~ 1 Hz at the focal plane. This assumes a standard AGN spectrum with a photon index of ~ 2.0 and a column density of 5 x 10^{22} H-atom cm^{-2}. For WFI, covering the complete field of view and the broadest possible band, the count-rate limit has been set at ~ 200 s^{-1}, falling within the PSF of the mirror (~ 10^{-12} erg cm^{-2} s^{-1}) for a pile-up of 1%. If the event rate exceeds this rate, the number of pile-up events simply increases. This is therefore not a hard limit with respect to detector safety but it is rather a limit imposed on spectral quality. The probability of the WFI obtaining a random source away from the galactic plane brighter than 10^{-12} erg cm^{-2} s^{-1} in its 5 arcmin FOV is less than 10^{-3}.

For NFI1, a rate of ~ 25 kHz/PSF (~ 10^{-10} erg cm^{-2} s^{-1}) is considered to be possible. This corresponds to a pile-up of ≤ 1%. For NFI2, the limit is considered to be ~ 250 Hz/PSF (~ 10^{-12} erg cm^{-2} s^{-1}). The time resolutions of the various detectors were summarised in Section 2.1.

2.7 The overall instrument capability

XEUS will be able to measure with no significant spectral contamination:

— the broadband moderate resolution spectra and position of all sources in its 5 arcmin field using WFI up to a flux level of ~ 10^{-12} erg cm^{-2} s^{-1} and down to a source as weak as 10^{-18} erg cm^{-2} s^{-1};
— with high resolution, the spectra of selected sources using NFI1 in the energy range 0.05-3 keV up to a flux level of ~ 10^{-10} erg cm^{-2} s^{-1} and down to a source as weak as ~ 10^{-17} erg cm^{-2} s^{-1};
— with high resolution, the spectra of selected sources using NFI2 in the energy range 0.5-15 keV up to a flux level of ~ 10^{-12} erg cm^{-2} s^{-1} with no significant spectral contamination, and down to a source as weak as ~ 10^{-17} erg cm^{-2} s^{-1}.

2.8 Secondary requirements

The high throughput of the XEUS mirror system also enables the study of a wide range of scientific topics unrelated to the primary objectives. The large area guarantees good photon statistics, which facilitates the analysis of temporal variations on unprecedented timescales. Likewise, the detection of faint signals opens up the possibility of exploiting polarimetric investigations for the first time. An extension of this large area to energies of tens of keV would dramatically enhance the leverage of energy range in spectroscopic measurements, and allow high-resolution imaging for the first time in the hard X-ray range. These natural advantages of the XEUS mirror system, over those of previous missions, naturally drive a demand for novel instrumentation to exploit these important secondary science investigations. Chapter 9 therefore highlights a package of instruments to complement the baseline payload in these areas.

3 The Wide Field Imager

3.1 Introduction

Of the three scientific instruments in the focal plane of the X-ray telescope, the Wide-Field Imager offers the largest FOV, of about 5 arcmin. The large collecting area (up to 30 m^2) and high angular resolution (2-5 arcsec) of the X-ray optics require new detector technologies. The physical quantities of interest are imaging (position resolution) and spectroscopy (energy resolution) with a high detection probability (quantum efficiency) in a single-photon counting mode at a high photon rate (time resolution without pile-up). The first choice for WFI is driven by its count rate capabilities and flexibility of operation. As the collecting area of XEUS in the zero-growth phase is already a factor of 20 larger than XMM-Newton's and a factor of 100 in the fully-grown configuration, it is clear that a new device concept is needed rather than improvements of existing schemes. Active Pixel Sensors (APS) will be the focus of consideration, being able to match the relevant physical parameters of WFI. The p-channel Depleted Field Effect Transistor (DEPFET) allows measurement of position, arrival time and energy with a sufficiently high detection efficiency in the range 0.1-30 keV.

As a fallback solution, fully depleted backside-illuminated frame store pn-CCDs and frame-store MOS CCDs are considered. Both have proved their feasibilities and reliabilities throughout the development and commissioning phases of XMM-Newton. They are described briefly in Sections 3.7 and 3.8. Two possible extensions to the WFI focal plane are a fast timing channel and an expanded field of view detector, and both were recommended at the XEUS International Workshop in Munich, March 2002. They would increase the power of the instrument for transient and serendipity observations.

WFI is (in most cases) a pathfinder for the two NFIs, each with a restricted FOV of the order 0.5 arcmin. Once a selected target is found and characterised in terms of position, energy and variability with WFI, detailed spectroscopic studies can be made with one of the NFIs, with an $E/\Delta E$ up to a factor of 50 better than the Fano-limited WFI.

3.2 The device and system concept

In all CCD-type concepts, charges are transferred slowly over large distances. They are intrinsically sensitive to radiation damage and to metallic contamination of the base material, because of the presence of traps in the bulk silicon. In addition, because of the relatively slow charge transfer, X-rays might hit the CCD during the readout time. This gives rise to events with positions erroneously assigned ('out-of-time' events).

In the DEPFET active pixel sensor, every pixel is a complete single detector sub-unit – detector and amplifying electronics in one. The DEPFET readout concept allows flexible windowing on the detector during the readout. Up to 1000 full frames per second can be processed, so most of the constraints inherent to CCDs are overcome.

The XMM-EPIC pn-CCD system is limited with pile-up at count rates of the order of 10 counts per HEW and per second. (The pile-up limit is given by the product of pixel area and readout time per pixel. This is correct as long as the signal charge cloud is significantly smaller than the pixel size). With a projected collecting area of up to 30 m^2, several hundreds of counts per HEW and second are expected for comparable observations. This means that a factor of 20 or more improvement in the XEUS zero growth phase (and a factor of about 100 when XEUS is fully grown) in frame speed is needed in comparison to the pn-CCD camera on EPIC-XMM, in order to exploit the capabilities of the XEUS mirror system.

The challenge of the WFI system is that 10^6 pixels must be read out 1000 times per second, delivering several GB of data. This is the unavoidable drawback of detection systems with high position resolution and simultaneous fast readout. This requires efficient data reduction immediately after the analogue-to-digital conversion.

Perspectives of the DEPFET system

The DEPFET detector system belongs to the family of active pixel sensors. Every pixel has its own amplifier and can be addressed individually by external means. This results in a high degree of operational freedom and performance advantages. The major advantages of DEPFET type devices are:

- operation with high spectroscopic resolution at temperatures as high as –50ºC, keeping the total readout noise below 5 electrons (rms).
- the charge does not need to be transferred parallel to the wafer surface over long distances. That makes the devices very radiation-hard, because trapping, the major reason for degrading the charge transfer efficiency, is avoided.
- the ratio between photon integration time and readout time can be made as high as 1000:1 for a full frame mode. That means the out-of-time events are suppressed to a large extent.
- as the integration time per event will be of the order of 1 ms and the readout time per line about 1 µs, more than 1000 counts per HEW per second (2 arcsec, i.e. 7 x 7 pixel) can be detected with a pile-up < 6 %.
- no additional frame store area is needed; the device is as large as the processed area.
- any kind of windowing and sparse readout can be applied easily and different operation modes can be realised simultaneously.
- the DEPFET transistor amplifier structure offers the possibility for a repetitive non-destructive readout (RNDR). Under those conditions, the readout noise can be reduced to < 1 electron (rms) by a repetitive reading of the physically same signal charge. This readout mode can be applied in selected areas, while the rest of the device is operated in the standard readout mode.

From the conceptual point of view, this is the most advanced semiconductor X-ray pixel detector because it offers a lot of additional features like the analogue storage of 2D X-ray images.

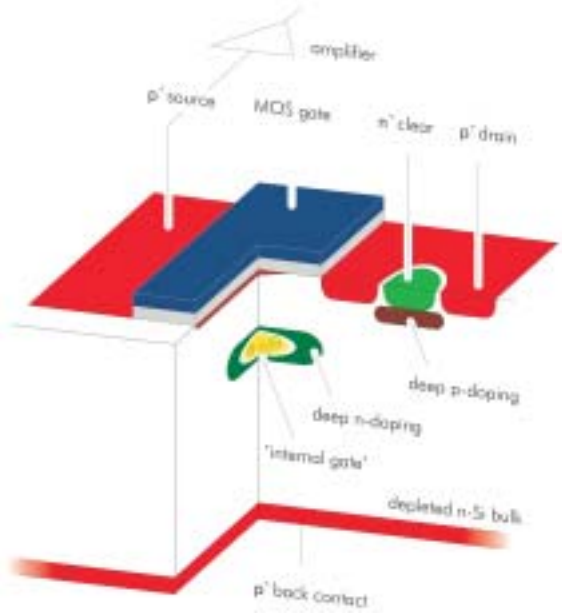

Figure 3.1. Cross-section of a DEPFET structure based on an enhancement mode MOSFET .

The standard DEPFET and DEPMOS devices are p-channel devices on n-type material. The use of p-type base material is very interesting for the DEPFET devices because the use of n-channel JFETs and MOSFETs becomes possible by using holes as the signal charges. This offers an increased transconductance of the transistors by a factor of three, improving the equivalent noise charge at least by a factor of 1.5.

Device concept and functional principle

The proposed DEPFET concepts are based on a detector-amplifier structure, which consists of a field effect transistor working on a depleted high-resistivity substrate. The cross-section of such a device is shown in Fig. 3.1.

The device makes use of the sideward depletion principle. Assuming that n-type semiconductor material is used, a detector chip can be depleted in such a way that there remains a potential minimum for electrons under the channel of a field effect transistor. It is capable of storing the signal charges for a long time – if needed, up to several seconds, depending on the operating temperature. It is straightforward to use such a device as a detector, where signal charges (electrons) are collected in the potential minimum, from where they can steer the transistor current, acting as an 'internal gate'. The signal charges change the transistor current by inducing charges inside the p-type channel of the DEPFET. The result is a simultaneous integration of the first amplifier stage on the detector chip, with a detection fill factor of 1. Fig. 3.2 shows an APS layout plot, based on DEPFET structures with hexagonal outline.

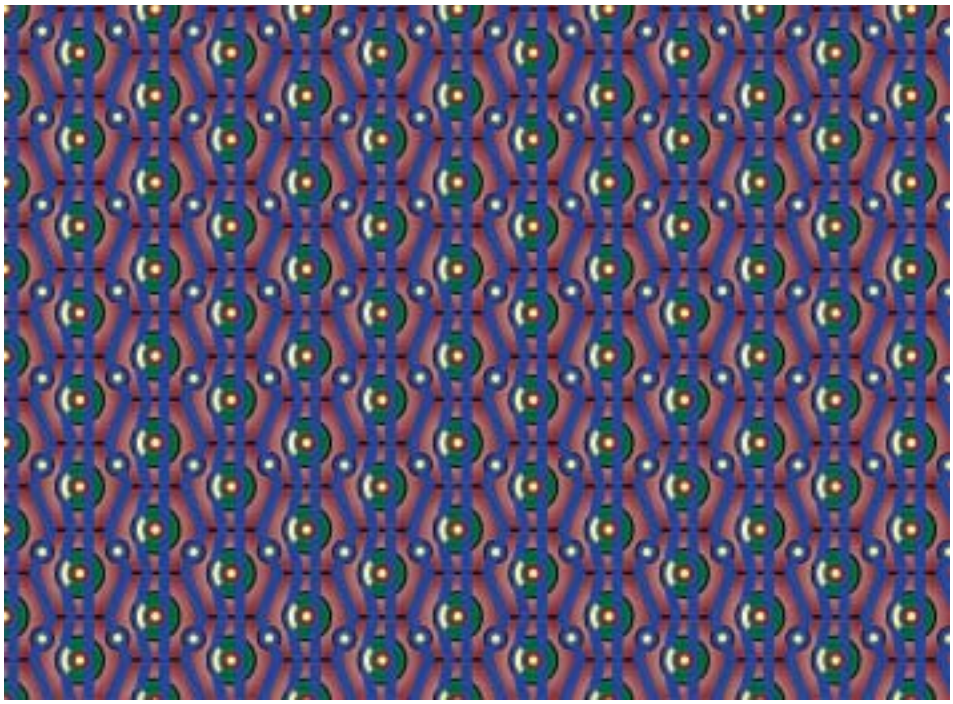

Figure 3.2. Layout plot of an Active Pixel Sensor with hexagonal pixel outline. Each hexagon is a DEPFET with cylindrical symmetry: the source in the centre of each pixel (red) is enclosed by the circular gate (green) and drain (red). The blue lines are metal connections; the yellow regions are contact holes for inter-layer connections.

The potential distribution in the device, calculated by the 2-D TOSCA code, is shown in Fig. 3.3. The potential maximum of the internal gate (minimum for electrons) is clearly visible and is separated from the external gate by the p-channel. The potential difference in the pixel area to its direct surroundings is about 1 V, sufficient to collect more than 100 000 electrons in one pixel.

Since the electrons are collected in a potential maximum (signals as well as leakage current), the device has to be reset from time to time by emptying the corresponding internal gate. One straightforward way is to apply a positive voltage to an adjacent n^+ contact, which acts as a drain for electrons.

In a first approach, devices were built in which periodically (hundreds of μs) all charges are removed from the potential minimum beneath the transistor. This is done by applying, for a short time (hundreds of ns), a positive voltage at the substrate contact. The result of a 2-D simulation shows the continuous rise of the bulk potential between the region under the transistor and the substrate contact for this particular case (Fig. 3.4). After the clearing procedure, signal electrons can be collected and stored in the electron potential minimum under the transistor channel. As the signal charges have

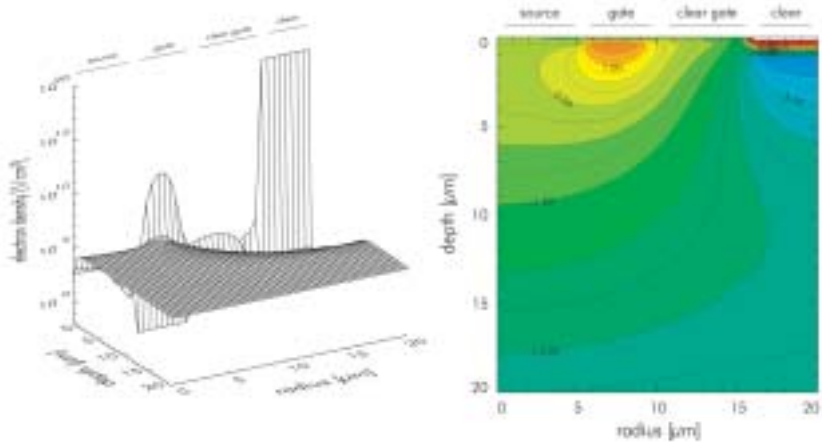

Figure 3.3. 2-D simulation showing the potential maximum (minimum for electrons) of the internal gate, in which electrons generated in the bulk are collected. The simulation was performed with the TOSCA program for a DEPFET with cylindrical symmetry where the source is in the centre of the structure. The view is from the top of the device into the bulk.

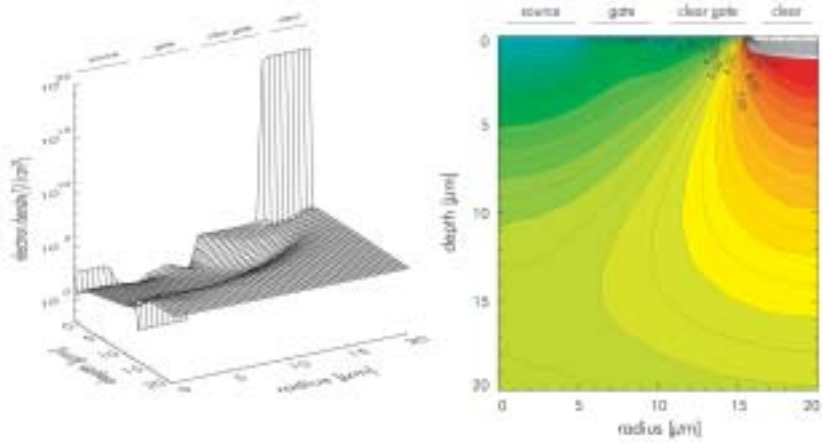

Figure 3.4. Result of a 2-D simulation of the clearing procedure. The potential inside the detector chip is visible while there is a positive voltage pulse (+15 V) applied to the substrate contact. The simulation was performed with the TOSCA program for a DEPFET with cylindrical symmetry, where the source is in the centre of the structure. The view is from the top of the device into the bulk.

to be removed explicitly and as the internal gate is continuously filled up with thermally generated electrons, the clearing procedure can be applied upon request or repetitively. The clearing mechanism acts locally where the clearing pulses have been applied. The information about the amount of signal charges stored can be recorded by measuring the rise of the transistor current. This measurement does not disturb the stored charges, so the readout process can be repeated several times and opens the option for a multiple non-destructive readout. If a row of DEPFETs is activated by the selective application of the external gate voltages, the charge content can be

measured, a clearing pulse could be applied and the charge measurement repeated without having signal electrons in the potential minimum. The difference between both measurements is the net signal of electrons in the internal gate.

3.3 System performance

The key parameters of the DEPFET system are listed below. Their values are derived from prototype measurements or, if transferable, from measurements with the XMM-Newton pn-CCDs. The main properties are summarised in the sections *Energy Resolution and Noise*, *Position Resolution*, *Count Rate Capabilities* and *Quantum Efficiency*.

Parameter	*Value*
Integration +Readout	
read time per row (128 channels)	2.5 μs
total read time	1.25 ms
integration: read time	800:1
Window mode	160 ms for 128 x 128 pixels
Response to Radiation	
QE @ 100 eV	100%
QE @ 110 eV	85%
QE @ 272 eV (C Kα)	90%
QE @ 1.740 eV (Si Kα)	100%
QE @ 8050 eV (Cu Kα)	100%
QE @ 10.000 eV	96%
QE @ 20.000 eV	45%
depletion depth	500 μm
Rejection efficiency of MIPs	100%
Spectroscopy	
Fano noise at 5.9 keV	118 eV FWHM
system noise	3-5 e^- (rms)
system noise with NDR	≈ 1 e^- (rms) for n = 16
^{55}Fe resolution	125 eV
C Kα resolution	50 eV
Radiation Hardness	
no change up to (@260K)	10^{10} p cm^{-2}
Focal Plane Geometries	
Device size	7.5 x 7.5 mm
Device format	1000 x 1000
Pixel size	75 x 75 μm^2
Position resolution	30 μm
Fill factor of focal plane	1
operating temperature	220K

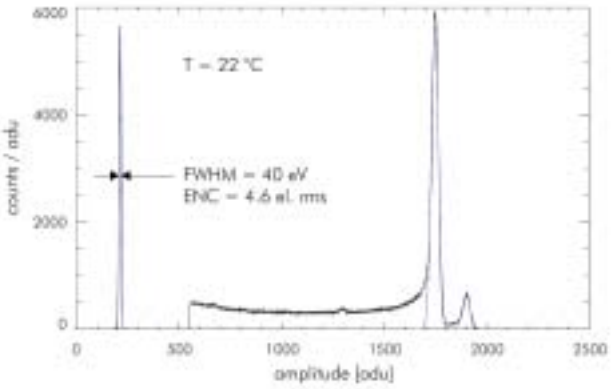

Figure 3.5. ^{55}Fe spectrum recorded with a DEPFET structure at 22°C.

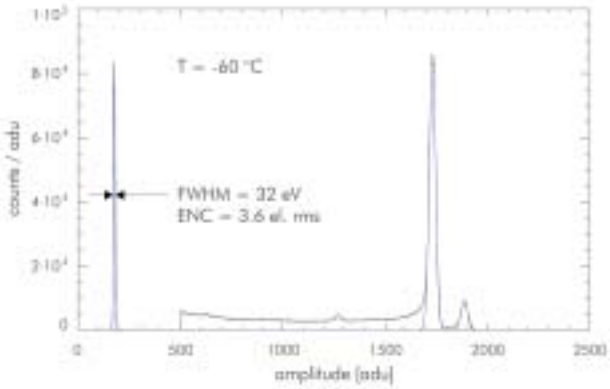

Figure 3.6. ^{55}Fe spectrum recorded with a DEPFET structure at –60°C.

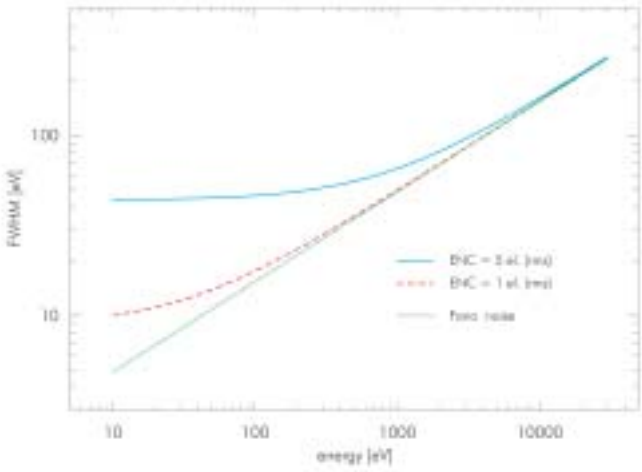

Figure 3.7. Calculated energy resolution as a function of the photon energy. The Fano noise is taken into account, as well as 5 el. rms and 1 el. rms equivalent noise charge, respectively.

Energy resolution and noise

Beside the statistical fluctuations of the ionisation process (Fano statistics), electronic noise is the dominant limitation of the energy resolution. The physical models of the devices used to understand the basic noise sources are therefore of great importance.

Considering the noise behaviour of the DEPFET, the 'total detector capacitance' of conventional detector-amplifier combinations can be neglected. Only the capacitance of the internal gate is relevant, as all kinds of stray capacitances and the capacitance of the external gate can be neglected. This leads to very low equivalent noise charges for the series noise contribution. The parallel noise of the structure originates in the volume generation of charges inside the fully depleted substrate and surface-generated currents.

To examine the noise characteristics, measurements of the energy resolution were performed using an ^{55}Fe source. Figs. 3.5 and 3.6 show spectra recorded with a DEPFET at room temperature, and at –60°C, with the Mn-Kα and Mn-Kβ lines at 5895 eV and 6495 eV.

The noise peaks in the spectra of Figs. 3.5 and 3.6 were measured separately while the detector was not exposed to radiation. The energy calibration was performed by comparing the position of the Mn-Kα line with the position of the noise peak. The electronic readout noise at room temperature (22°C) is 4.6 el. (rms). Reducing the parallel noise contribution of the leakage current by cooling the device to –60°C results in an improved noise figure of 3.6 el. (rms). Both spectra were obtained at shaping times of a few μs.

The obtainable energy resolution with a DEPFET detector is shown in Fig. 3.7. In the standard full-frame mode, with pixel read times of about 1 μs, the FWHM resolution, including readout noise and Fano fluctuations, is shown. Down to 1 keV incident photon energy, the energy resolution is determined mainly by the Fano noise. The improvement in energy resolution from 50 eV up to 500 eV with the RNDR is clearly seen in the dashed curve, indicating the 1e^- read noise.

Position resolution

Owing to the diffusion of the signal charges during their drift from the conversion point inside the silicon into the potential minimum of the pixel, the spatial measurement precision can be improved substantially, with relatively large pixel sizes. The improvement is significant, if the signal charge cloud diameter is of the order of the pixel size. Taking into account the thicker silicon wafer (500 μm thickness in the 15-cm version) and the longer transit times, i.e. collection times for the generated electrons, the charge cloud, containing 96% (±2σ) of all signal charges will have a diameter of about 40 μm. For a pixel size of 75 μm, about 70% of all events will be split events and 30% contained within one pixel. Under these conditions, the position resolution will always be better than 20 μm, but for most cases better than 5 μm. A position resolution of 0.2 μm for X-ray photons absorbed at the pixel boundaries was verified experimentally. Those values may be changed by the temperature, pixel layout and operating voltages. The relatively weak photon energy-dependence of the position precision is neglected for this estimation.

Theoretical and experimental studies of the position resolution using the charge-spreading technique and the impact on energy resolution must be considered. It seems reasonable that a pixel size of 75-100 μm is adequate for the anticipated angular resolution and focal length. This pixel size can even handle the expected FWHM of the point spread function below 1 arcsec.

Figure 3.8 demonstrates the effect of charge spreading and position reconstruction of the incident photon. The improvement of the position resolution because of the extension of the electron charge cloud is equally true for the pn-CCD detector. The x-axis indicates the position of the photon

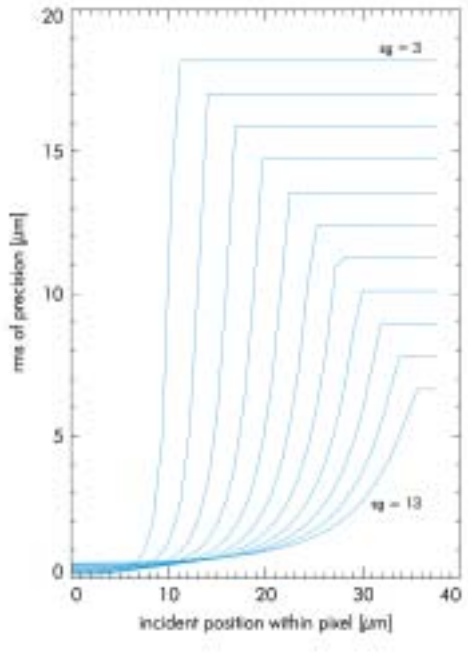

Figure 3.8. Improvement of the position precision as a function of the Gaussian spreading of the electron charge cloud. The typical sigma of the Gaussian ('sg') of the Gaussian electron distribution is 7 µm. The assumed pixel size is 75 µm. 1000 el. have been generated and processed with a noise level of 5 el. (rms).

hit. At $x = 0$, the photon hits the pixel exactly at the boundary to the neighbouring pixel. Here, the position resolution is optimum. As the physical situation is symmetrical with respect to the centre of the pixel, the x-axis ends at half the pixel size. On the ordinate is plotted the position resolution (rms). This number must be multiplied by a factor of three, if the position precision of more than 90% of the photons is to be better than the rms value on the ordinate. The parameter 'sg' (sigma of the Gaussian) scales the lateral signal spread before arriving in the pixel well. The upper curve indicates sg = 3 µm and increases to sg = 13 µm at the bottom. For a 500 µm-thick detector, the typical sg is between 7 µm and 9 µm.

Count rate capabilities

As WFI count rate capabilities are of major importance to the overall performance of XEUS mission, the flux losses and pile-up behaviour are treated in more detail. The calculations shown below take into account a PSF similar to XMM-Newton's, but with an angular resolution of 1 arcsec.

With preliminary parameters describing the envisaged telescope performance, it is possible to simulate the effect of pile-up for the CCD as focal plane instrument. Pile-up is the effect of changing either a pattern type and/or the energy information of a photon event owing to the occasional hitting of adjacent (or the same) pixel by more than one photon in a readout cycle.

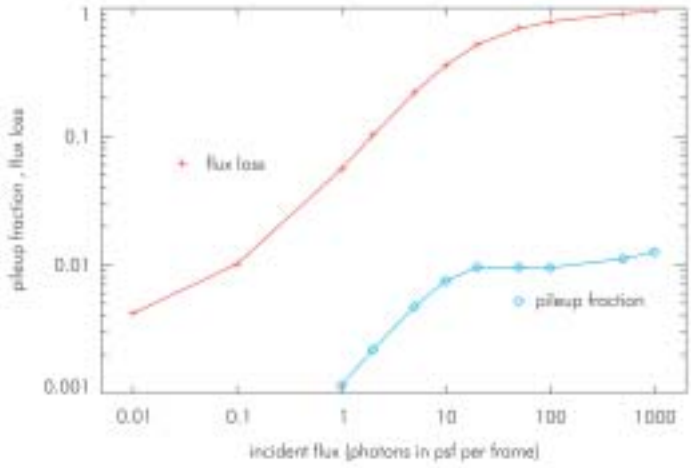

Figure 3.9. Flux loss and pile-up fraction as a function of the incoming photons. Around 1000 frames will be read out each second.

For the case of the DEPFET detector together with the XEUS-telescope (Fig. 3.9), for a rate of one photon per readout cycle (1000 photons per frame), only 6% of the incident flux is lost, and the contamination of the spectrum is about 0.1% (1000 photons per second correspond roughly to a source of 5 mCrab for the Phase-A telescope configuration). A telescope with 1 arcsec angular resolution and focal length of 50 m is assumed, corresponding to 10 pixels HEW on the detector.

The flux loss is a scalar correction factor that can be rather easily handled, while the more complicated case of spectral contamination owing to conventional pile-up is more than an order of magnitude smaller.

Quantum efficiency

As the XEUS mission intends to achieve high sensitivity from the very low energies (around 50 eV) up to 30 keV, the detector entrance window and the sensitive thickness must be optimised. The practical thickness of such a detector is limited to 500 µm because the background from Compton events in the spacecraft increases with detector thickness. On the low-energy side, the studies on <100>-oriented silicon will continue, in order to improve the spectroscopic response down to 50 eV. The limiting quantity for the low-energy response is clearly the optical blocking filters. As a baseline, we propose a 100 Å-thick monolithically integrated Al filter on the radiation entrance side.

For X-rays in the range 0.1-30 keV, the response is shown in Fig. 3.10. It is remarkable that the change of absorption depth in silicon over 5 orders of magnitude is reduced to a quantum efficiency variation of less than 30% in the detectors.

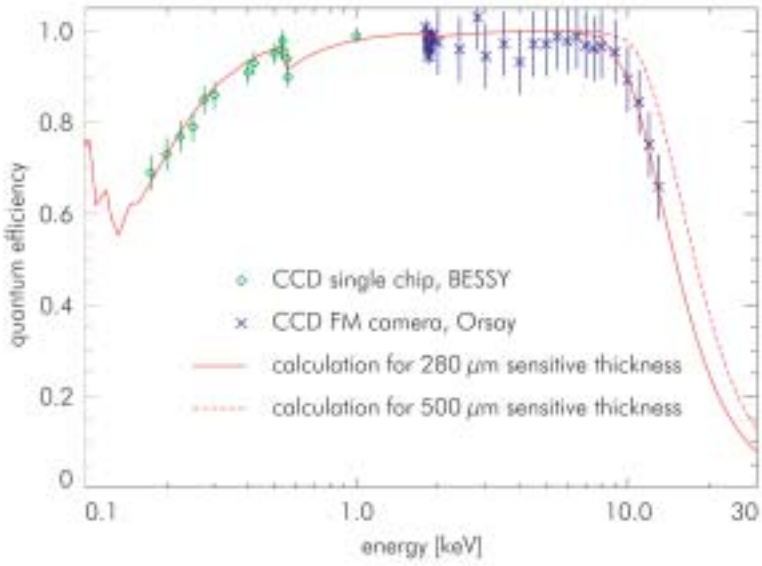

Figure 3.10. Quantum efficiency (QE) measured with pn-CCDs in a single photon-counting mode at the synchrotron facilities BESSY in Berlin and LURE in Orsay. The lines show the QE calculated from the photon absorption coefficients for 280 µm- (solid) and 500 µm- (dashed) thick detectors. The calculated QE for a 500 µm-thick detector is still 35% QE at 20 keV.

The experience with XMM-Newton has revealed the advantages of avoiding very thin optical blocking filters: free-standing 7 x 7 cm pinhole-free filters of thickness < 0.2 µm are difficult to fabricate, calibrate and operate throughout the integration, test and launch of the camera. Technical precautions for preventing the destruction of the filter by acoustic noise load during transport and launch are necessary. As X-ray observations without any light filter would not produce the desired spectral resolution because of the optical loading, it would be advantageous to integrate a thin aluminum layer directly on to the radiation entrance window of the detector, such that the detector itself serves as the mechanical support for the filter.

First tests of very thin Al layer deposition on silicon detectors have been made and show very promising results with respect to homogeneity and layer thickness. It seems that a 500 Å-thick Al deposition can be made reliably.

Future research in this field will include the test of the light-tightness of the filters as well as their uniformity and long-term stability. Depending on the astrophysical X-ray input spectrum through the telescope and on the ionising particle background in orbit, the fluorescence light generated in the on-chip filter must be studied.

Both proposed camera systems (DEPFET active pixel sensors and frame store pn-CCDs) will be equipped with the integrated aluminium filters. As

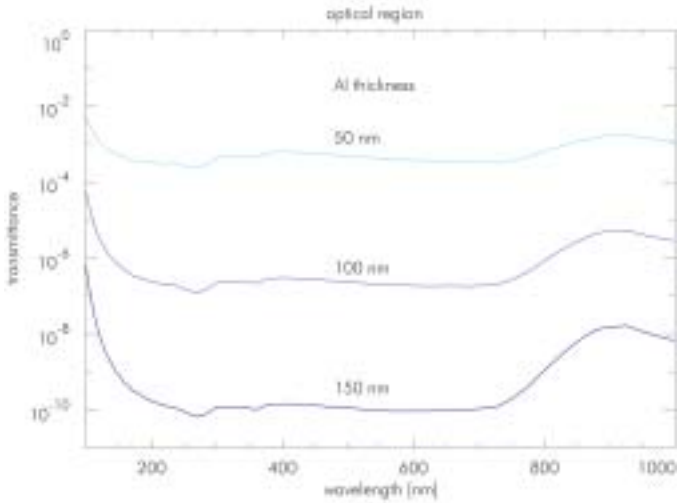

Figure 3.11. Attenuation of optical photons from the UV to the near-IR as a function of wavelength. The transmissions of Al layers of 50 nm, 100 nm and 150 nm were calculated. It is assumed that the Al layers are integrated directly on to the CCD's entrance window.

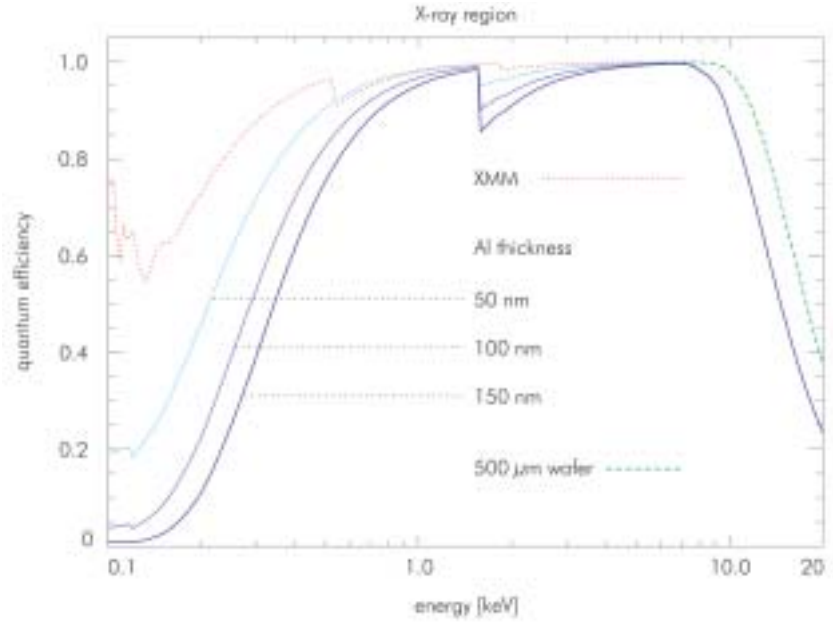

Figure 3.12. Reduction of quantum efficiency as a function of X-ray energy and Al thickness. The upper curve shows the XMM pn-CCD performance with no Al on the CCD. The assumed detector thickness is 300 µm and 500 µm.

the thickness of the aluminium layer strongly affects the quantum efficiency up to 2 keV (Fig. 3.12) a thin on-chip filter could be envisaged, while a thicker, mechanically more stable filter may still be required to block the visible light from very bright sources in the field of view.

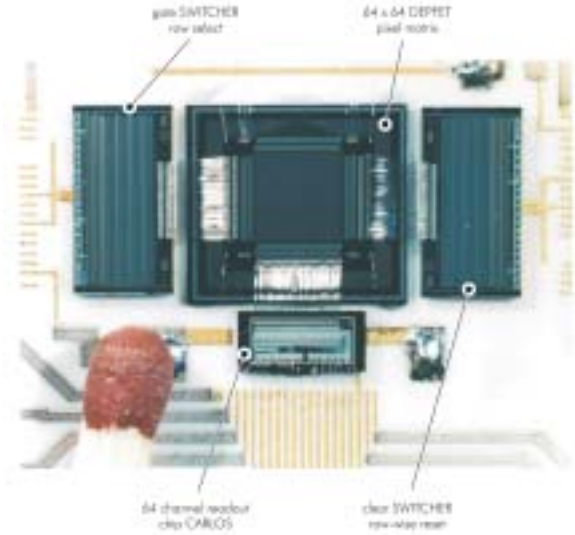

Figure 3.13. APS prototype with 64 x 64 pixels and 50 x 50 µm pixel size.

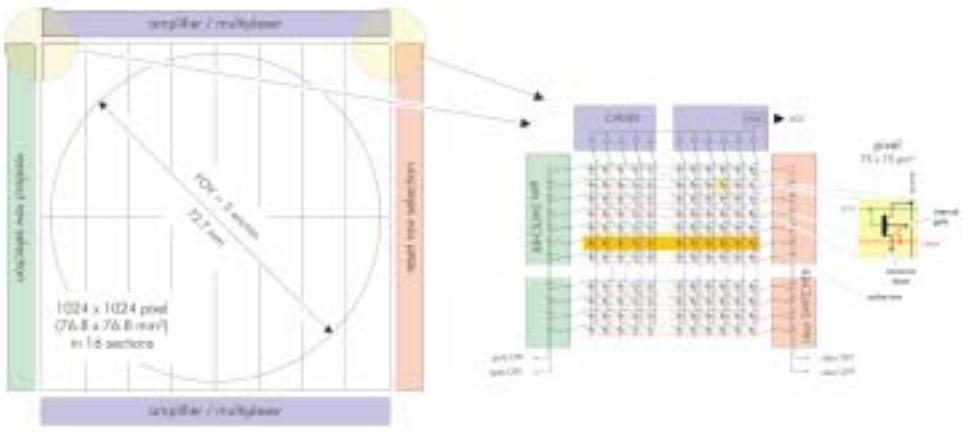

Figure 3.14. Layout of the focal plane pixel matrix system, consisting of the detector chip and surrounding readout and control electronics. The figure shows the sensitive area and its logical division.

3.4 Pixel matrix system

Experience indicates that a monolithic focal plane of up to 8 arcmin is possible; the XEUS design is based on a 5 arcmin FOV.

Focal plane layout and mechanics

Figure 3.13 shows a small DEPFET-based APS prototype of 64 x 64 pixels and a pixel size of 50 x 50 µm. In normal operation, the transistors of each row in turn are activated, read and cleared by CMOS control chips ('SWITCHER'). While the DEPFETs of the one active row are read in parallel by a multi-channel CMOS preamplifier/multiplexer ('CARLOS'), the rest of the pixels are turned off and in integration mode, thus keeping dead time short and power consumption low.

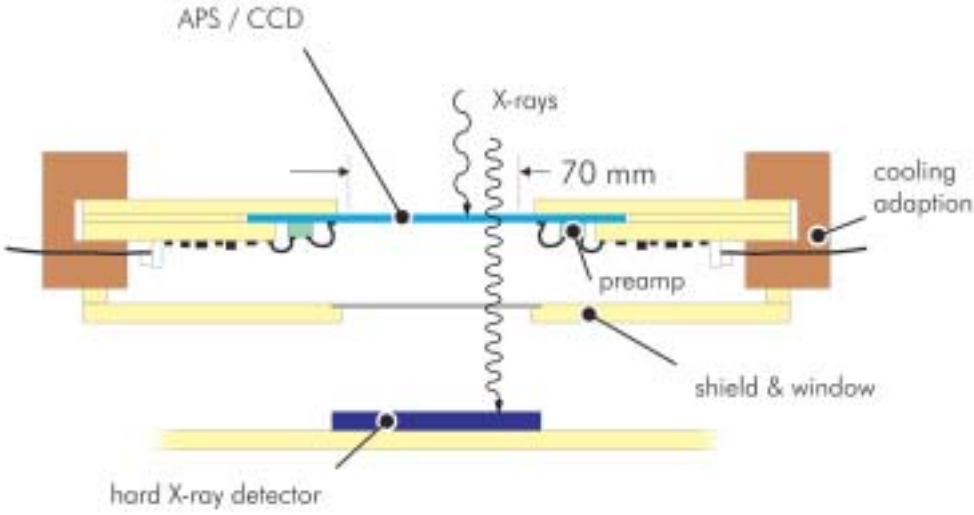

Figure 3.15. Cross-section through the mechanical arrangement of the focal plane.

As shown in Fig. 3.14, the layout of the XEUS focal plane is the same, but with the size and number of pixels scaled up. The central part is the pixel matrix chip. It is logically divided into 16 sections according to the control and readout scheme (see below). However, its internal design remains completely uniform.

The readout (upper and lower sides) and control (left and right sides) chips are placed around the sensitive area. The pixel size is 75 x 75 µm. The matrix of 1024 x 1024 pixels results in a sensitive area of 76.8 x 76.8 mm. The exposed area, assuming a FOV of 5 arcmin and a resulting diameter of 72.7 mm, is totally covered by the detector's geometry. The number of spatial resolution elements is at least 4000 x 4000 (see Section 3.3).

A cross-section of this arrangement is sketched in Fig. 3.15. Connections to the ASIC chips and to further signal processing components are realised by wire bonding. An additional detector layer for hard X-rays, which have a high probability of passing the APS or CCD without interaction, may be placed underneath.

Electronic control and analogue read-out

The pixel matrix system is divided into two identical monolithically integrated subunits (upper and lower), each having their independent control and analogue readout electronics. The following description refers to one such unit. All actions mentioned may happen in both subunits simultaneously. The pixel matrix needs a control scheme to activate selectively a row of pixels for readout or reset. These units are placed along the left and right sides of the matrix in Fig. 3.14. From the left side, one (horizontal) row of pixels is selected for readout. This is achieved by applying an appropriate gate voltage to all pixels of this row, which switches on the

transistor currents. From the other side, a clear pulse can be sent to a selected row. The control chips are identical, but a dedicated voltage supply and timing scheme has to account for either clearing or selection-for-readout.

Each column (512 pixels) of a subunit is fed into one channel of a multiplexing pre-amplifier chip. This ASIC has 128 inputs and one output. A sub-unit is such subdivided into 8 readout units of 128 x 512 pixels each. The analogue readout is done in four steps:

— current to voltage conversion and amplification;
— multi-correlated sampling/filtering with offset subtraction;
— storage of the amplified analogue signals in sample-hold stages;
— output of these signals.

The first three steps are done for n x 128 pixels (channels) in parallel, n being the number of amplifiers readout (1-8). In step 4, the signals are sequentially output into ADCs (1 ADC/readout unit).

Read-out modes

The readout has high flexibility arising from:

— its non-destructive character;
— random access to single rows and columns (channels);
— independent and parallel readout of sub-units;
— readout units.

Depending on the scientific goal of an observation, different readout modes can be selected, such as:

— full-frame readout: search for regions of interest (ROIs, can have arbitrary shapes);
— masked full-frame readout: after ROIs have been defined, all other pixels are either suppressed or readout at much lower frequency;
— timing mode: a selected image region is read out at the highest possible frequency;
— mixed mode: different readout modes can be applied to dedicated image regions.

Data processing

As described above, each of the 2 x 8 readout units is fed into a multiplexing amplifier followed by an ADC. One readout unit operating at maximum speed generates 32 Mpix s^{-1} (assuming a frame rate of 500 Hz). Data processing mainly aims to reduce this to a manageable rate in several steps:

— according to the selected readout mode, only part(s) of the pixel matrix is read out and AD-converted at maximum speed;
— after AD-conversion the data are masked, i.e. only pixels in ROIs are further processed. Bad pixels and pixels outside the exposed area are rejected;

— necessary correction is applied, such as offset subtraction and gain factors;
— an event filter is applied, i.e. only pixels above an individual threshold are accepted.

This chain of data processing will be performed in parallel for each of the 16 readout units.

Calibration

As a first calibration step, each pixel is read out an appropriate number of times (typically 100), with the detector matrix shielded from any incoming radiation. The average offset and fluctuation (noise) of each pixel are calculated by statistical evaluation. Pixels with excess noise are stored in a 'bad pixel map'. For 'good pixels', the offsets and event thresholds are recorded.

In the second calibration phase, the matrix will be flat-field exposed to an onboard X-ray source. Another set of calibration frames are taken and evaluated to determine and store each pixel's gain factor. 'Blind' pixels are identified and added to the bad pixel map.

Power consumption

An active pixel (i.e. one selected for readout) delivers a current of typically 200 mA into 5 V. At maximum, 2 x 1024 pixels can be simultaneously active, resulting in a power consumption of about 2 W for the pixel matrix. Amplifier/multiplexer chips consume about 16 x 1 W, clearing and readout selectors about 2 x 1 W. Total power dissipation in the focal plane adds up to about 20 W.

3.5 The repetitive non-destructive readout (RNDR)

In cases where the count rates does not exceed the pile-up limit and/or the area of interest is restricted to a smaller window, e.g. 2 x 2 cm, the same signal charge can be read out several times. The field of interest for RNDR in the focal plane can be chosen relatively freely, leaving the rest of the detector in its conventional readout mode.

Because the electrons are confined in the electric field below the sensing gate of the DEPFET amplifier (floating gate amplifier) and are not mixed with other charges, the measurement of the amount of signal charges can be repeated as often as required.

The noise can be reduced by

$$ENC(n) = ENC_o \sqrt{n}$$

where n is the number of readings of the signal charges and ENC_o the noise of a single reading.

We expect a single read noise of the DEPFET structure of $4e^-$ at –50°C with

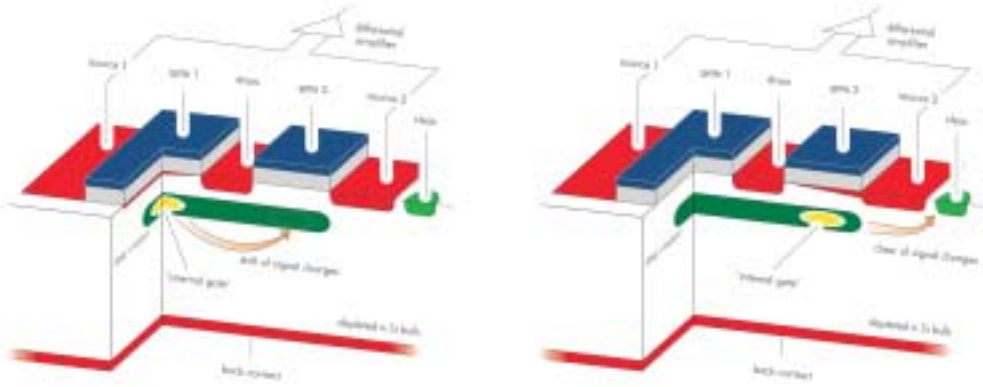

Figure 3.16. Two adjacent DEPFET devices are able to transfer the signal charges from one floating gate amplifier to the neighbouring one, reading the same signal charges several times. The read noise is reduced by $n^{1/2}$, where n is the number of readings.

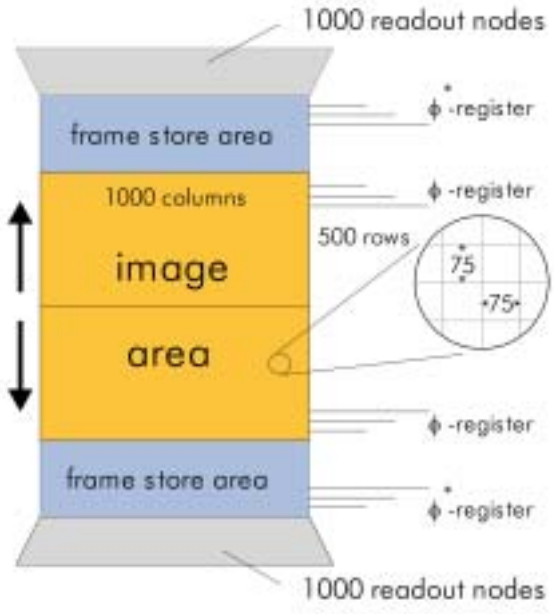

Figure 3.17. Example of a pn-CCD operated in a frame-store mode. The imaging area has a pixel size of 75 x 75 µm.

a shaping time of 1 µs. Repeating that procedure 16 times, spending 16 µs for the reading of two pixels, a single electron noise floor could be achieved, corresponding to an energy resolution of less than 10 eV (FWHM). This would allow expansion of the usable X-ray bandwidth down to 50 eV. As the areas that make use of the non-destructive readout can be selected during operation, we can imagine running the detector slowly in areas where sources have been detected and fast (without RNDR) where it is not required.

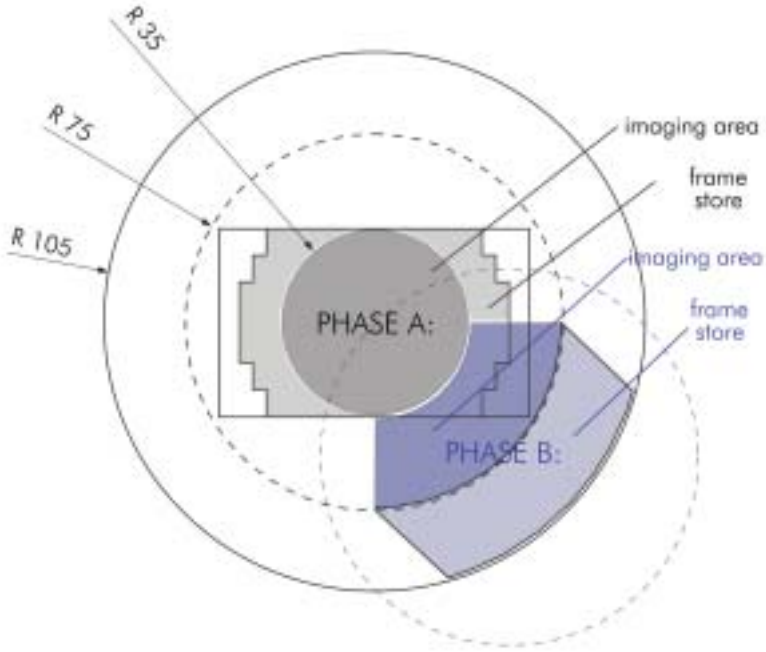

Figure 3.18. Composition of the whole focal plane with frame-store pn-CCDs. The outer CCDs are slightly cylindrical. The Phase-A configuration has a diameter of 70 mm, covering a FOV of 5 arcmin, while the Phase-B configuration covers the 10 arcmin FOV.

3.6 Resources

The WFI power and mass requirements are 200 W and 150 kg, respectively. The mass is only slightly higher than that of the XMM pn-CCD camera, but the 50 times pixel throughput means the power consumption goes up significantly. A detailed engineering study is needed to derive the resources with a precision of better than 10%.

3.7 pn-CCD frame store CCDs for XEUS

As in conventional CCDs, a frame-store format can be employed for pn-CCDs. The area to be processed in a quasi-defect-free manner increases by the size of the store area. A 7 x 7 cm image area can be realised monolithically on a 15-cm wafer (Fig. 3.17). If pn-CCDs are used for the 14 x 14 cm focal plane, a possible extension of the focal plane camera is shown in Fig. 3.18. The whole field of view could be covered by that technique with a minimum of insensitive gaps between the butted devices. The central part, the inner diameter of 7 cm, would be homogeneously sensitive.

The major change in concept, besides the smaller pixel size, is the dramatic increase in frame rate because of the modified readout philosophy. By doubling the processed area and dividing it into image and store sections, the required readout speed is obtained for the large collecting area of the XEUS

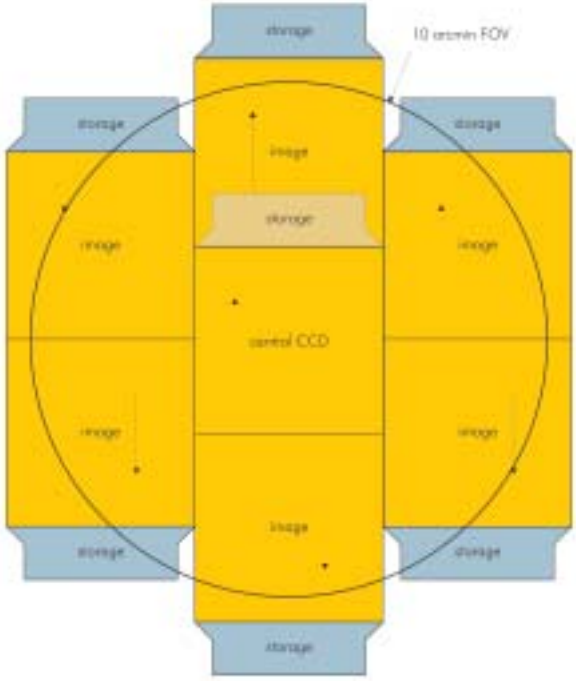

Figure 3.19. Example of the 10-arcmin FOV for a MOS CCD. The central CCD is vertically displaced with respect to the others. A FOV of 5 arcmin would be realised by one monolithic CCD.

mirrors. As will be shown later, we expect to achieve a frame rate of the whole camera of 200 s^{-1}. That will lead to a count rate of more than 200 s^{-1} and HEW.

As the pixel size shrinks, the number of read nodes and transfers increases. At the same time, the system requires more readout time and is more sensitive to radiation damage because of the higher number of transfers. If charge-sharing of signal charges among more than one pixel is needed for improving position resolution, the effective read noise per event will be higher by a factor $\sqrt{n}$ (n is the number of pixels involved). To maintain the high readout speed of the pn-CCD EPIC-XMM system, the signal processing must be speeded up by a factor of two. The solution to the above 'constraints' seems to be realistic, but must be proved experimentally.

To date, the signals of one row (64 pixels) are processed in parallel in 22 μs. The extension to 128 channels on the CAMEX amplifiers, to match the new pixel pitch, was previously realised for applications in high-energy physics, but it would involve a redesign of the CAMEX64B for low-noise operation. In addition, the signal process time must be shortened by a factor of two. The increased readout speed will certainly have an impact on the power consumption, which is below 1 W for the 36 cm^2 array.

If 128 channels are read out at 12.8 MHz, 10 µs would be required for the parallel readout of one pixel line. For the parallel transfer from the image to the storage area, 100 ns is needed for one transfer. A device of 1000 x 1000 pixels would be divided (as in the XMM-EPIC case) into identical halves of the image area, i.e. 500 x 1000 pixels each. For the parallel 500 shifts, 50 µs would be needed for the transfer from the image to the insensitive storage area. The readout time for the storage area while integrating X-rays in the image part would then be 500 x 10 µs = 5 ms. That means the whole focal plane would be read out within 5 ms. The out-of-time probability for the X-ray events will then be 1:100. In this operation mode, 200 image frames can be taken in 1 s with a full-frame time resolution of 5 ms.

3.8 A frame store MOS CCD system

MOS CCDs have been developed in collaboration with industry with great success. Large-format devices were integrated in the XMM-Newton focal plane. Significant improvements were made with respect to detection efficiency at the low- and high-energy ends, from 200 eV up to 10 keV. The energy resolution was Fano-limited and readout algorithms allowed pattern recognition of useful events. The pixel sizes can also be tailored according to the requirements given by the X-ray telescope.

They could be further improved to depletion thicknesses of up to 300 µm, keeping all other relevant parameters unaffected. As in the case of the pn-CCDs, they have the potential to match the XEUS requirement, with all restrictions inherent to CCDs in general. By increasing the number of read nodes and improving the readout speed of the front-end electronics, up to several hundred full frames per second seem to be feasible.

The 5 arcmin FOV could also be covered by one monolithic MOS CCD with dimensions of 7.5 x 7.5 cm plus the store areas (Fig. 3.19). The limiting fact is the parallel transfer time, which could be speeded up by using a double metal process to overcome the high-resistance polysilicon gates. Most probably this would require a backside-illuminated device.

With a read speed of 1 Mpix s^{-1} at a read noise of 5 el., about 200 read nodes would be required to match the XEUS frame requirement of at least 200 s^{-1}. This must be coupled to a high-speed event-recognition system that keeps track of the anticipated pixel rates.

3.9 WFI thermal control

General considerations

The WFI consists of a detector chip and a readout chip, connected over a short distance. The operating temperature is ~ 200K for the detector chip and < 250K for the readout chip. They are stuck together with silicon, which results in heat conduction of ~ 0.6 W K^{-1} (kSi = 160 W m^{-1} K^{-1}). With a heat dissipation of 20 W for the readout chip, the temperature difference between the chips is ~ 35K. This means, to reduce the heat input at the detector chip,

the readout chip must be cooled to < 230K. It is therefore proposed to operate both chips at 200K.

During measurements, temperature stability of 0.5K is required. Larger temperature variations require recalibration of the sensor.

Cooling

The DSC is a cube, with one side directed towards the Sun for optimum solar cells illumination. For observational reasons, the angle between the telescope axis (+X) and the Sun will be limited to 90-120° and the minimum angle between +X and the Earth horizon will be 4°.

Calculations over one orbit, with +Z always pointed towards the Sun, have been made for the average heat input from Earth, Earth-albedo and Sun for each side of the cube with SSM foil (IR-emissivity = 0.8, Sun absorptance = 0.2). SSM-foil is used to reduce the heat input from the Sun and/or the Earth-albedo. The minimum average temperature is calculated for a radiator with an area of 1 m^2 and an additional heat load of 20 W, looking to deep space (no restrictions of the view factor through the spacecraft). The variation of the heat input during one orbit for all sides of the cube could be as much as 100 W.

Side	*Radiation Input Power from Earth and Sun (Wm^{-2})*	*Min. Average Temperature (K)*
+X	64	196
–X	64	196
+Y	60	194
–Y	60	194
+Z (Sun)	239	260
–Z	84	207

The radiator

Only the –Z and +X faces will not be exposed to the Sun, so a trade-off analysis was performed for only these two positions. Transient calculations, using ESATAN, show large temperature variations during one orbit (170-230K for the +X face; 160-270K for the –Z face).

A radiator coupled to phase-change capacitors

To reduce these large temperature variations, phase-change materials (PCMs) could be used. On the –Z side, this results in a temperature of ~ 220K with a heat reservoir of 200 kJ. At +X, the temperature should be ~ 210K with a heat reservoir of 120 kJ.

Material	*Melting Temp. (K)*	*Latent Heat of Fusion ($kJ\ kg^{-1}$)*	*Specific Volume ($l\ kg^{-1}$)*
n-Heptane C_7H_{16}	182.4	141	1.46 (293K)
Methyl Propyl Ketone $C_7H_{10}O$	195.2	104	1.24 (293K)

from ESA PSS-03-108

Most of the PCM will be used to compensate for the high heat load from the Earth and Earth-albedo, and not from the sensor. For this reason, a heat switch between the radiator and PCM could improve the performance. The heat switch reduces the PCM mass. For both positions of the radiator, only an 84 kJ heat reservoir is necessary. In addition, the achievable temperatures decrease, especially for the –Z side (200K). A similar effect could be achieved by using louvres to close the radiator. The advantage of the heat switch is that, by using a gas gap, no moving parts are required. Similar gas-gap heat switches have already been developed for space applications, but not for such large thermal loads or this temperature range.

A radiator combined with a Peltier element

Another possibility for stabilising the temperature is to use a Peltier-cooler (thermo-electric). A heat lift of 20 W at a temperature difference of 30K is required. The electrical input to provide this cooling at room temperature is ~ 60 W. The efficiency of Peltier-elements decrease with decreasing temperatures, so the input power may be ~ 100 W. With this electrical input, it is also possible to use a Stirling cooler. Sunpower Inc. has already built a Stirling cooler that provides 35 W at 223 K with 60 W input power. This cooler has already flown on a Space Shuttle mission, but the lifetime may be a problem for a mission such as XEUS.

WFI thermal design summary

A radiator with a phase-change capacitor (PCC) together with a heat switch seems the best solution to cool the WFI detector. PCCs are a proven technology. One problem will be to find the PCM with the required melting temperature. Gas-gap heat switches exist, but must be redesigned for this high heat load and temperature range. The best position for the WFI thermal control system is on the –Z side, since at this location there is no need for sunshields. If XEUS takes measurements only over the night side of Earth (which is baselined), the PCC mass could be reduced. The radiator on the –Z side provides the maximum cooling power on the night part of the orbit. In addition, the power-consuming parts of the detector can be switched off during periods of non-measurement. This means that the PCM must compensate only for the heat load from the support structure. If, however, no heat switch is used, the +X side is the preferred radiator location, because the temperature is lower and a smaller PCC is required. However, this side also contains a baffle and the pointing system to the MSC, which will affect the overall configuration.

Thermo-electrical cooling with Peltier-elements is not applicable, because they need a high power input. For the same electrical power, a Stirling cooler can operate with a higher heat load at room temperature.

3.10 Conclusions

The first choice for WFI is an active pixel sensor because:

— the count rate capabilities are high enough to cover the whole bandwidth provided by the mirror system in a single-photon counting mode;

— it offers the operational flexibility to adapt locally the required readout speed;
— as no transfer of charges is needed, it is resistant to all kinds of radiation levels found in space;
— the power consumption is lower than in a CCD owing to the absence of large area shift registers.

All other physical quantities can be fulfilled with pn-CCDs or MOS CCDs, such as:

— 300-500 μm depletion depth;
— monolithic fabrication of 7 x 7 cm large sensors;
— Fano-limited energy resolution down to 100 eV.

4 NFI1: the Narrow-Field Soft X-ray Imaging Spectrometer

Narrow-Field Imager 1 is optimised for the 0.07-3 keV energy band (> 70% efficiency). This soft X-ray range is especially suited to studying objects at high redshift, because the XEUS mirror effective area is very large indeed below 2 keV.

Of the two high-resolution imaging spectrometers, the STJ-based NFI1 has been available with the required energy-resolving power longer than competing technologies. While this type of device is now available in small-array formats, considerable development is still required to meet the demanding requirements of XEUS. NFI1 will cover only a small part of the XEUS field of view (~ 0.5 arcmin, i.e. ~ 7 mm). The spatial resolution, as defined by the pixel size, over-samples the telescope PSF (2 arcsec goal) by a factor of ~ 3. With a plate scale of 240 μm/arcsec and a pixel size of ~ 150 μm, the spectrometer could comprise a single STJ array of 48 x 48 pixels. Such a large-format array of relatively large devices with a goal resolution of < 2 eV at 500 eV is a major technological challenge. This array could comprise individual discrete detectors or possibly be formatted as a matrix array (Section 4.13) to reduce the number of signal wires and electronic chains. Another option would be an array of 1-D distributed read-out strip detectors (DROIDs; Section 4.13), which are most promising with respect to energy resolution and detection efficiency, but with lower count-rate capability because they are inherently slower. Significant development work is therefore required to establish the optimum format for the XEUS NFI1 based on STJs.

4.1 The NFI1 instrument

Principal of operation

The absorption of a photon of energy E (eV) in a superconductor is followed by a series of rapid processes that involve the breaking of Cooper pairs by energetic phonons created by the hot electrons produced as the atom relaxes after the initial photoabsorption. This cascade converts the photon's energy into a population of free-charge carriers known as quasiparticles in excess of any thermal population. For typical transition metals, this conversion process ranges from nanoseconds (niobium) to microseconds (hafnium). At sufficiently low temperatures (typically an order of magnitude lower than the superconductor's critical temperature, T_c), the number density of thermal carriers is very small while the average number of excess carriers, N_0, created as a result of the photoabsorption process can be written as

$$N_0(E) \sim 6 \times 10^2 \, E/\Delta(T/T_c)$$

Here, the photon energy is expressed in eV and the temperature-dependent energy gap $\Delta(T/T_c)$ is in meV. Thus, in a superconductor such as tantalum, the initial mean number of free-charge carriers created, $N_0(E)$, is ~ 10^3 eV^{-1}.

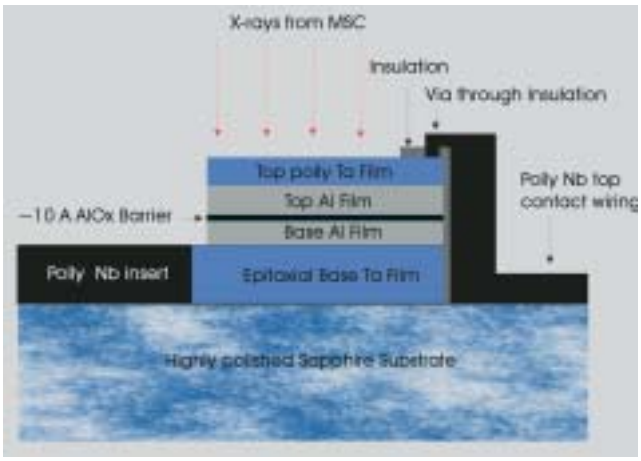

Figure 4.1. A cross-section through a typical tunnel junction, showing the key features and the mode of X-ray illumination.

The variance on $N_0(E)$ depends on the variance in the partition of the absorbed X-ray energy between productive phonons, phonons with energies $\Omega > 2\Delta$ that can break Cooper pairs, and phonons that are essentially lost from the system ($\Omega < 2\Delta$). The population of $\Omega < 2\Delta$ phonons evolves with time as the average energy of the increasing quasiparticle population relaxes, through quasiparticle phonon emission, towards the bandgap. The variance $<N_0>$ depends on the superconductor's bandgap Δ and its Fano factor F such that:

$$<N_0> \sim 6 \times 10^2 \, FE/\Delta(T/T_c)$$

Expressing this variance in terms of the energy resolution:

$$\delta E_F \, (\text{eV}) \sim 0.1 \, [FE \, \Delta(T/T_c)]^{1/2}$$

It has been shown that F is ~ 0.2 for elemental superconductors such as niobium and tin. This therefore represents the fundamental Fano-limited resolution of any superconductor. Thus superconductors such as tantalum or hafnium with $T << T_c$ when irradiated with soft X-ray photons of energy ~ 1 keV have a Fano-limited resolution of ~ 1.2 eV and ~ 0.2 eV, respectively.

The quasiparticles produced through photoabsorption can be detected by applying a DC potential across two such films separated by a thin insulating barrier, forming a superconducting tunnel junction (STJ). This potential bias favours the transfer of quasiparticles from one film to the other through quantum mechanical tunnelling across the barrier. The detector signal is therefore represented by the current developed by this tunnel process. After initial tunnelling, a quasiparticle can tunnel back, therefore contributing many times to the overall signal. On average, each quasiparticle will

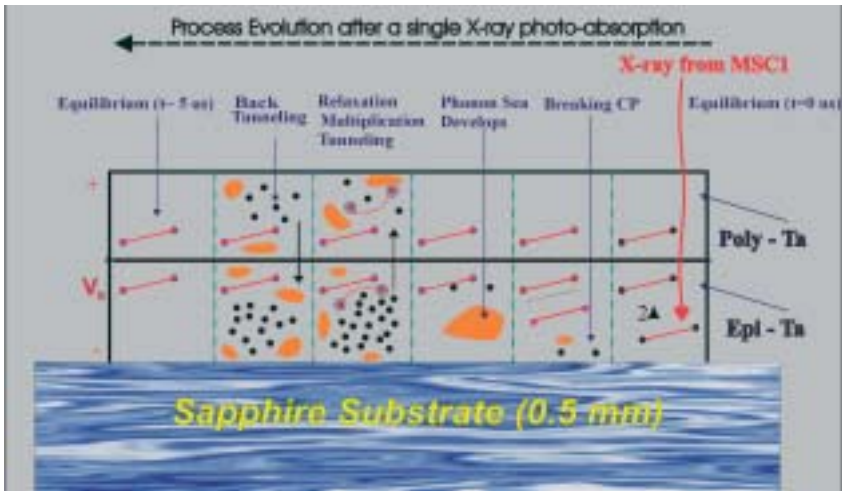

Figure 4.2. The various processes operating in the junction after the photoabsorption of a soft X-ray photon. From right to left, the process starts when the base film is in equilibrium at t = 0 μs and finishes with all free charge lost and the system back in equilibrium at t = 5 μs.

contribute <*n*> times to the signal before it is lost from the system through traps etc. Hence the mean number of effective charge carriers $N = \langle n \rangle N_0$. Typically <*n*> is of order 10-100 and depends on the size and nature of the STJ. Fig. 4.1 illustrates the cross-section through a typical junction; Fig 4.2 illustrates the various physical processes described above.

The multiple tunnel process leading to <*n*>, the average number of tunnels per quasiparticle, is, of course, also subject to statistical fluctuation. The fluctuations owing to the Fano process and those arising from the tunnel process can be added in quadrature such that the overall limiting resolution for a perfectly symmetrical STJ can be written as:

$$\delta E_T \text{ (eV)} \sim 0.1\ [E\ \Delta(T/T_c)(\text{F}+1+1/n)]^{1/2}$$

The tunnel-limited resolution for an STJ-based on unproximised tantalum or hafnium irradiated by 1 keV photons is therefore ~ 2.8 eV and 0.5 eV, respectively. Fig. 4.3 illustrates the tunnel junction-limited resolution for a number of elemental superconductors based on the following parameters:

Material	T_c *(K)*	Δ *(meV)*	τ_{qp} *(ns)**	τ_Ω *(ns)**	δE *(0.1 keV)**	δE *(1 keV)**
Niobium	9.20	1.550	0.149 (0.386)	0.004 (0.009)	1.4	4.5
Vanadium	5.30	0.800	5.3 (4.8)	0.013 (0.012)	1.0	3.2
Tantalum	4.48	0.664	1.8 (2.4)	0.023 (0.016)	0.9	2.8
Aluminium	1.14	0.172	100 (453)	0.242 (0.246)	0.5	1.5
Molybdenum	0.92	0.139	2077 (2963)	0.405 (0.579)	0.4	1.3
Hafnium	0.13	0.021	~ (8000)	(20)	0.2	0.5

τ_{qp} : quasiparticle characteristic time; τ_Ω : phonon characteristic time. Data in ( ) are based on recent data on the phonon-related characteristics of these materials. *resolution in eV at the indicated energy.

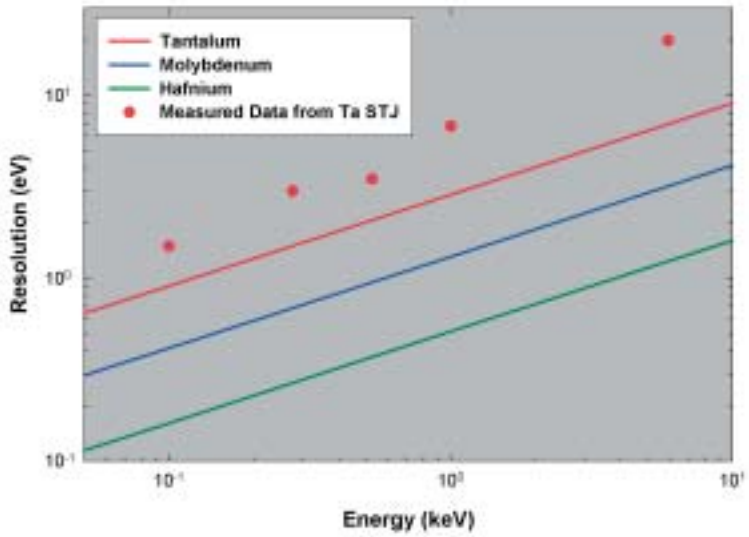

Figure 4.3. The tunnel-limited resolution of an STJ fabricated from a number of elemental superconductors. In addition, the measured resolutions of Ta-based junctions are shown; they are within a factor of ~ 2 of the theoretical tantalum tunnel resolution.

Practical considerations

The above description provides an overview of the basic operating principles of the STJ detector, but there are a number of practical issues that must be taken into account in developing a real working device. Of primary importance is the suppression of background current through the junction. There are three sources of background current: (a) the 'Josephson current' associated with the tunnelling of Cooper pairs across the barrier at zero bias voltage; (b) a current of thermal quasiparticles, and (c) a leakage current associated with perimeter insulation and micro-shorts in the barrier.

The Josephson current can be suppressed by placing the device in a homogeneous magnetic field oriented parallel to the plane of the junction. The dependence of the Josephson current on the magnetic field is a typical classical diffraction pattern. In the simplest STJ geometry (a square device in which the leads are orthogonal to the junction's sides), the Josephson current variation with applied magnetic flux is:

$$I/I_0 = \sin(\pi\phi/\phi_0)/(\pi\phi/\phi_0)$$

With this pattern, the peak currents decay slowly to zero, thereby requiring rather high fields in order to suppress the Josephson current and bias the junction in a stable fashion such that it can operate effectively as a photon detector. At such high fields, the band gap, Δ, is reduced and smeared since the magnetic flux penetrates into the superconducting films over dimensions non-negligible compared to the size of the junction. However, for other choices of the STJ geometry, the drop-off in the Josephson current with

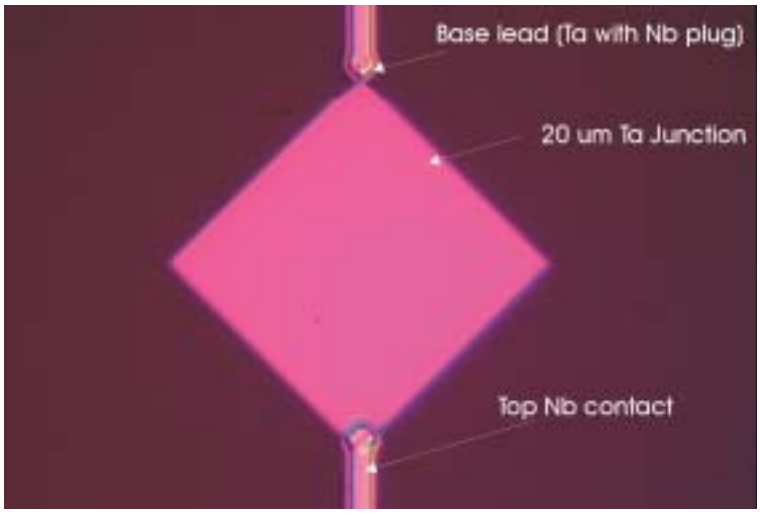

Figure 4.4. A Nomarski photo of a typical small Ta-based STJ optimised for operation at low magnetic field strengths. The top lead is Nb and the base Ta lead is plugged with Nb. The Nb prevents diffusion of the charge out of the junction.

applied field can be much faster than that of the square junction. A particularly attractive choice from the standpoint of close packing the STJs into an array is the 'diamond shape' illustrated in Fig. 4.4, where the sides are equal and orthogonal, but the leads exit along the diagonal from two opposite corners. The suppression function for this case is given by:

$$I/I_0 = 2\ [\cos\ (\pi\phi/\phi_0)/(\pi\phi/\phi_0)^2]$$

A plot of this relation as a function of applied magnetic field for a typical diamond-shaped tantalum device is presented in Fig. 4.5. This shape has been used successfully in small 6 x 6 arrays of close-packed junctions where the Josephson currents of each junction can be suppressed with the same applied field. The development of larger arrays coupled to larger devices specifically for the XEUS programme will require even further care in the design and layout of devices in order to suppress this Josephson current.

The thermal quasiparticle contribution to the background current is a direct and strong function of the operating temperature of the device. The thermal quasiparticle density scales as $T^{1/2}\ e^{-\Delta/kT}$. If we require that the thermal population be at least one order of magnitude smaller than the population produced by absorption of a photon with a typical energy of > 0.1 keV, then the temperature must be less than ~ 0.1 T_c. For a Ta- or Hf-based device, this requires operating at temperatures < 450mK and ~ 40mK, respectively. However, multiple tunnelling and charge trapping modifies this conclusion somewhat, and, in practice, somewhat lower temperatures are desirable.

The suppression of the leakage current requires fabrication of high quality,

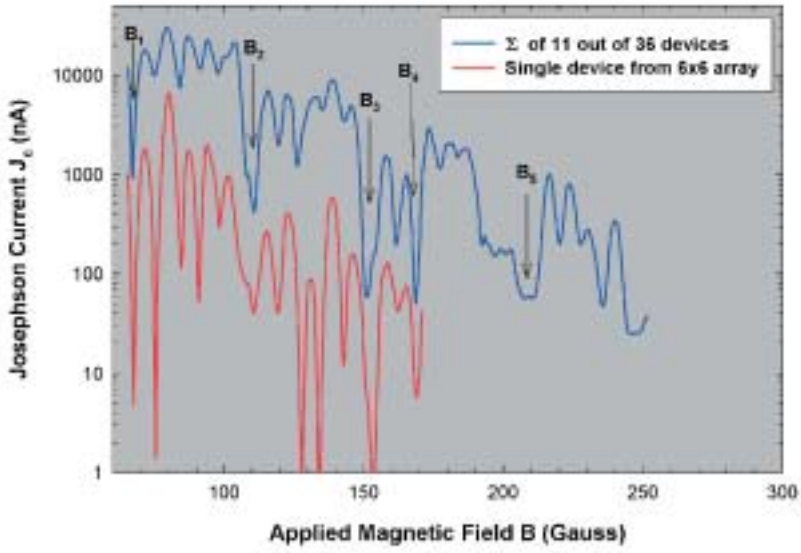

Figure 4.5. Typical Josephson current diffraction pattern obtained for a small diamond-shaped junction forming part of a 6 x 6 pixel array as a function of the applied magnetic field, B. The summed Jc (B) pattern for 11 pixels of the same array is also shown, together with the possible optimum magnetic field bias points (B_n). The array was of Ta-Al and each pixel was 25 x 25 μm.

uniform insulating barriers and superconducting layers. These are achieved via deposition of epitaxial metal layers on a smooth substrate, with controlled oxidation to produce the insulator. Leakage currents < 50 fA μm^{-2} can be obtained by these fabrication methods, providing a very sensitive low-energy response and a resolution close to tunnel-limited.

Unlike optical STJs, an X-ray STJ must be illuminated from the front rather than through the substrate (Figs. 4.1 and 4.2). For soft X-ray applications, the top layer film should therefore be very thin in order to ensure that the bulk of the X-rays are absorbed in the bottom superconducting layer, which is of high-quality epitaxial material and provides a somewhat higher energy resolution. However, to ensure an efficient soft X-ray response, thick dielectric insulators and high-density top wiring cannot be used in fabricating arrays of such devices because they would absorb the very soft X-rays. This is therefore a fundamental technical problem associated with large-format close-packed STJ arrays that are to be individually readout.

A second important concern for STJs is the suppression of quasiparticle losses, which introduce statistical broadening in the distribution of the measured charge signal per unit photon energy, and therefore degrade the resolution. Loss mechanisms include recombination with background thermal quasiparticles, and diffusion away from the junction, prior to tunnelling. One way to reduce the influence of losses is by enhancing the tunnelling probability. This can possibly be achieved using a technique known as ‘quasiparticle trapping’. A second superconducting ‘trapping layer’,

with lower critical temperature, is inserted between the primary photo-absorbing layer and the insulator, on both sides of the junction. Quasiparticles produced in the photo-absorbing layer diffuse into the trapping layer, where they scatter off phonons and lose energy, owing to the lower gap energy in the lower critical temperature material. Once their energy falls below the gap energy of the outer layers, they can no longer diffuse back out, and thus remain trapped close to the insulator, which enhances tunnelling. Typically, aluminium is used as the trapping layer in Ta- and Nb-based devices, and the insulator is aluminium oxide, produced by oxidising the aluminium after deposition. The lower band gap material (Al), of course, will influence the band gap of the higher band gap superconductor (e.g. Ta) through the proximity effect.

Fabrication of imaging arrays

This section considers possible approaches for the development of a relatively large field imaging system based on tunnel junctions.

STJ arrays

The design of an array is governed by a number of considerations:

— in order to ensure maximum packing density, the shape of the individual junction should be square, but with the connecting leads deposited at the opposite corners (diamond shape) to minimise the magnetic field required to suppress the Josephson current;
— the junction area must be kept reasonably small in order to limit the capacitive contribution to the electronic noise.
— photolithographic processes required to print the paterns have a maximum resolution of ~ 1-2 μm. This constrains the lead widths, as well as the maximum number of devices in any one row on a chip. The packing density of these leads also limits the minimum device size;
— the total number of leads must be minimised in order to reduce thermal loads. This requires the base film to be electronically common to all devices, so that a single lead can accommodate all of the base leads. Approaches for single top lead placement also need to be considered;
— all current array chips are fabricated on 5-10 cm wafers from a single, optimised trilayer. After dicing, a number of array chips can be produced from a single wafer. Other areas on the wafer are reserved for electrical or material diagnostic structures. This ‘on-wafer’ diagnostic approach ensures a high degree of reproducibility in performance among devices on a chip, and from chip to chip, and also ensures high yield;
— all leads are made from niobium, a higher band gap material, in order to act as potential charge reflectors and thereby suppress quasiparticle diffusion away from the junction;
— to ensure electrical conductivity in the base film, while maintaining the physical separation between base films of different junction devices, the base must be trenched to the substrate with a width of 2-5 μm. This approach constrains the packing density. Electrical connectivity is maintained through the use of bridges across the trenches linking adjacent devices. To prevent quasiparticle leakage from one device to

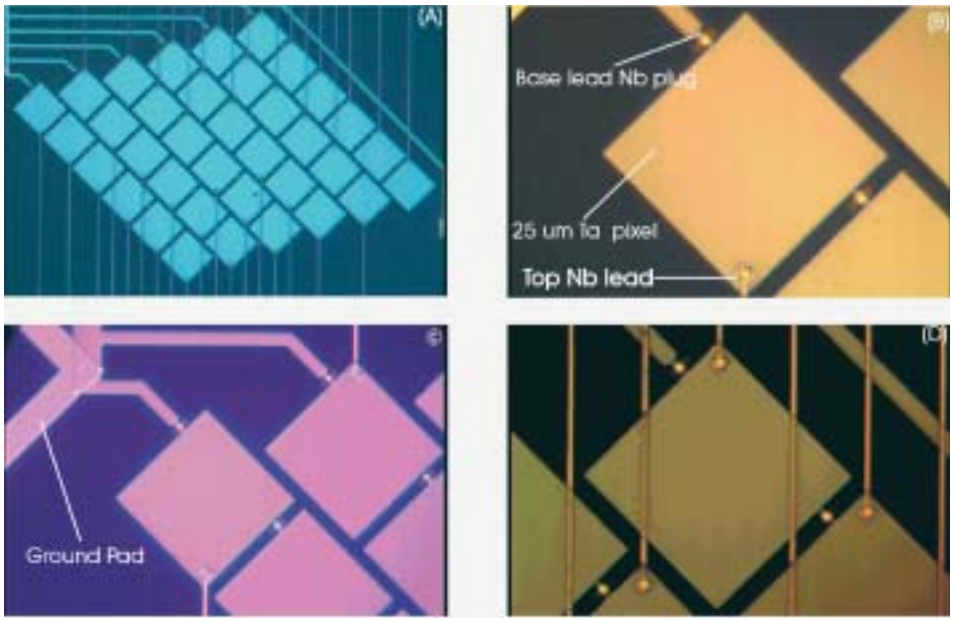

Figure 4.6. A set of Nomarski photos of a 6 x 6-pixel Ta array of STJs. Such an array was used to obtain the spectra shown in Fig. 4.15. A: the full array; B: a higher resolution image of a single pixel and its connection via a Nb plugged Ta bridge to adjacent pixels; C: the region where the common base film connects to the ground pad; D: the effect of the top wiring which, if too dense, reduces the efficiency at soft X-ray energies.

another, the bridges are also plugged with niobium, which, as in the case of the leads, acts as a charge reflector.

Figure 4.6 is a Nomarski photograph of a developmental Ta 6 x 6 STJ array highlighting the quality of the lithography. The devices are 25 μm square with 1.5 μm-wide leads and 4 μm-wide trenches. The bridges crossing the trenches are etched to < 1 μm to reduce charge diffusion. The 6 x 6 arrays have been successfully demonstrated in S-Cam2, a superconducting camera for ground-based astronomy in the visible (350-650 nm). Each device in this array has its own Nb top contact wiring that connects through a via in a Silox film through to the top Ta film. Each device therefore operates as a discrete detector with its own signal detection and signal processing chain. All these devices exhibited the required Josephson current suppression at the same magnetic field, and require a bias potential of ~ 0.2 mV. The variation in mean charge output of these devices is shown in Fig. 4.7 and is less than 5%. The production of larger-format arrays by the same processing steps is a natural extension of this work.

Figure 4.8 shows an array of 10 x 12-pixel devices before its removal from the wafer. 10 x 12-pixel arrays with 100% yield of low-leakage pixels have been fabricated and are currently integrated for further testing in the S-Cam3 instrument.

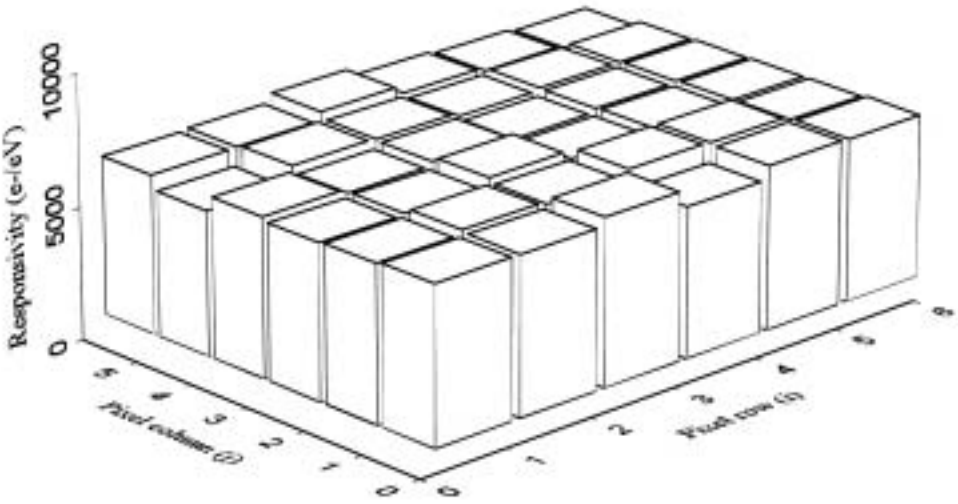

Figure 4.7. Variation of the mean charge output across a 6 x 6-pixel Ta STJ array illuminated by UV radiation.

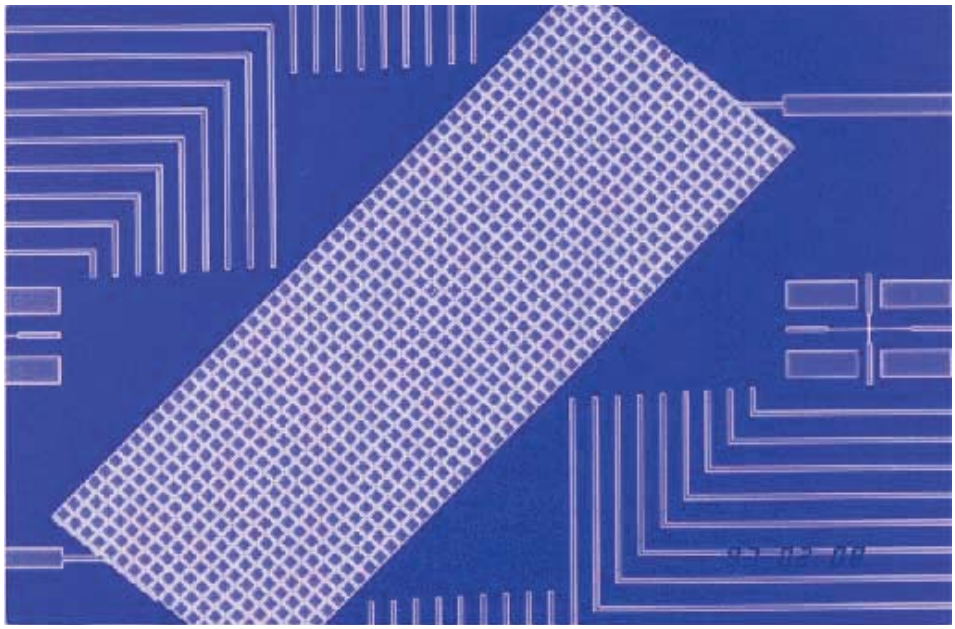

Figure 4.8. A microscope image of a large-format array (10 x 12 pixels) on wafer before completing the top contact wiring.

It must be stressed that expanding the format of the array to 48 x 48 with a pixel size of 150 μm while further improving the energy resolution is a major technological challenge. Such an array still would have the drawback of the large number of signal lines as well as the packing density of the top contacts.

Figure 4.9 shows an alternative approach to the direct readout array: the

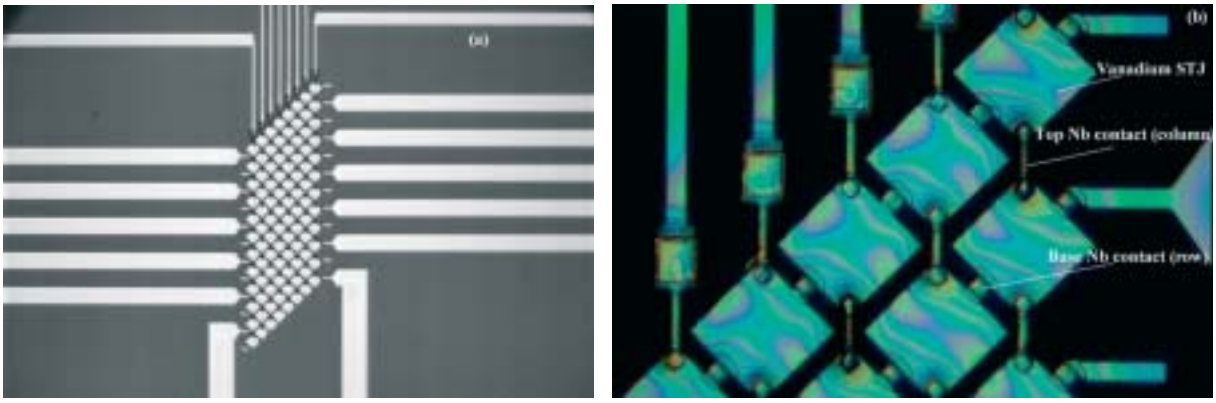

Figure 4.9. A reduced readout (matrix) chip of 12 x 8 pixels again deposited on a sapphire substrate. The devices are based on vanadium, while all wiring and plugs are in niobium. Such a chip expanded to 24 x 24 pixels could form a sub-array of the XEUS NFI1.

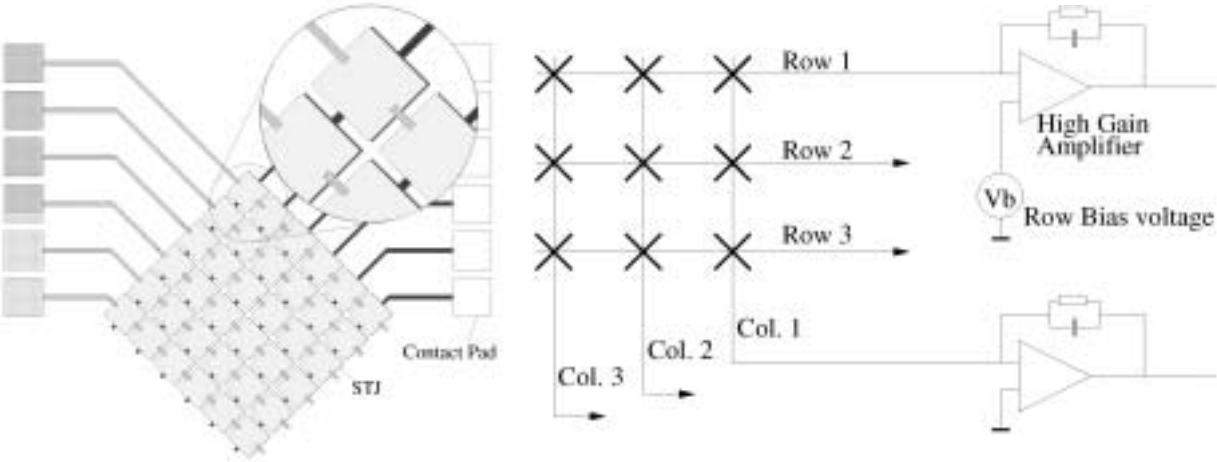

Figure 4.10. The simplified connection (left) and readout scheme (right) for the matrix array.

'matrix readout' array. Here, an array of 12 x 8 devices has been fabricated in such a manner that the number of readout lines has been reduced to only 20. This matrix readout approach connects the base film of all devices in an array from the same row and top films from the same column. Events are then read out using a coincidence technique between signals from the base and top films. This not only reduces the amount of front-end electronics and the thermal problems associated with the large number of wires entering the cryostat, but also removes the problems associated with dielectric and contacts obscuring the top film. An implementation of this technique using JFET charge-sensitive amplifiers has shown that energy resolution can degrade according to the associated input capacitance increase. The signal-to-noise ratio can be restored somewhat by the combination of signals from the row and column outputs. A theoretical study shows that, when series

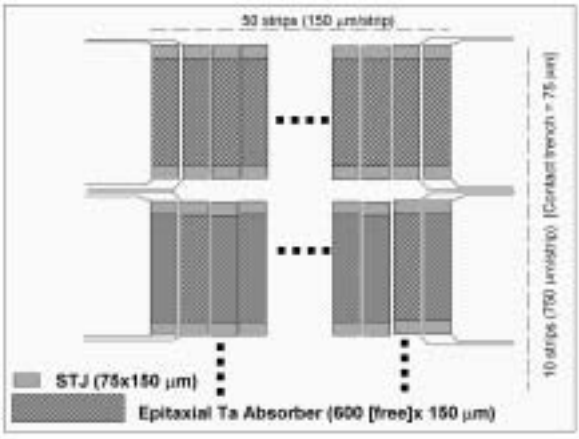

Figure 4.11a. A 1-D DROID system covering the NFI field of view of 0.5 arcmin.

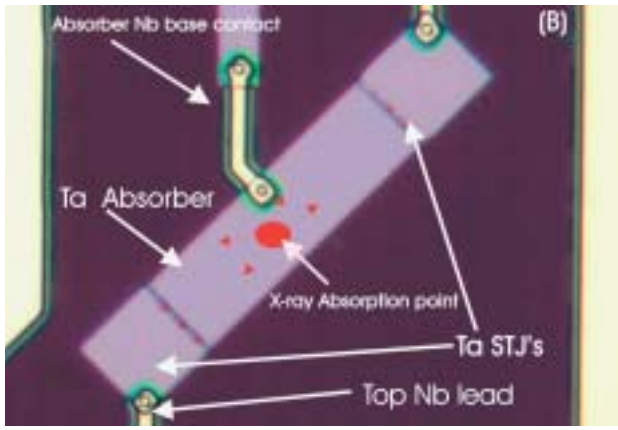

Figure. 4.11b. A Nomarski photo of a Ta-based 1-D DROID.

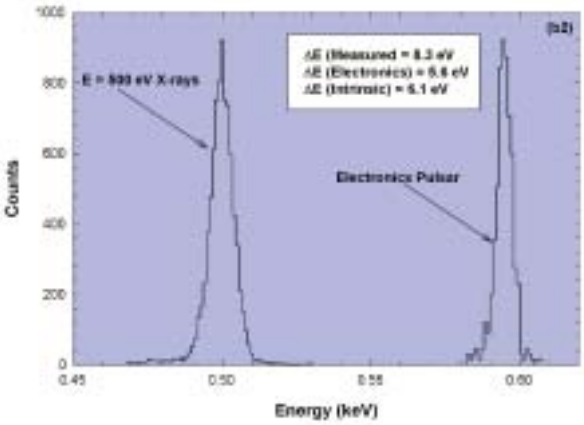

Figure 4.11c. Measured energy resolution of 1-D DROID at 500 eV. Major contribution to resolution degradation is the bias instability.

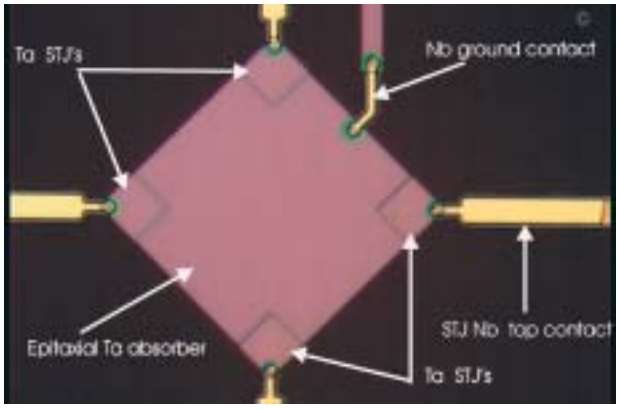

Figure 4.11d. A Nomarski photo of a 2-D DROID.

noise dominates, a 10 x 10 array of 25 μm detectors would have equivalent noise charge increased by ~ 4. However, as this noise is uncorrelated in row and columns, the overall degradation is only ~ 2.8.

Figure 4.10 shows the simplified schematic of such a matrix readout applied to a 6 x 6 array. Such arrays are under development.

Distributed readout arrays

The requirement of individually biasing and reading out large-format arrays of up to 2000 devices is demanding. A possible solution is offered by DROIDs, in which photons are absorbed in an epitaxial superconducting film such as Ta of large dimension (the absorber) and the resultant charge detected by STJs located at the corners of either a 2-D absorber or at the ends of a 1-D

strip of absorber. By time-coincident event measurement, it is possible to reconstruct both the absorption position and the energy of the incoming photons. Disadvantages of this approach are the relatively low sustainable count rate (dependent on the chosen geometry) and the sensitivity of the absorber to flux trapping. Compared to an array, the 2-D DROID offers a large sensitive area with a considerable reduction in the number of readout connections. Whether such a 2-D DROID could retain the stringent energy resolution requirements remains to be demonstrated, although spatial resolutions of < 10 μm have already been achieved. The 1-D DROID, while not providing such a large reduction in readout connections, might be able to maintain the required energy resolution simultaneously with the spatial resolution and while handling reasonably high count rates.

Good spectroscopic performance has been demonstrated with a small 1-D prototype DROID (10 x 200 μm, including two 20 x 20 μm readout STJs at the end; see Fig. 4.11b, left), for which resolution ~ 2.4 eV FWHM at 500 eV was achieved. DROIDs with improved geometry and larger dimensions have been designed. Fig. 4.11 shows a possible arrangement from a 1-D DROID-based array where the number of readout lines has been reduced to < 1000 compared to the 2300 required for an array of 48 x 48 direct STJs.

4.2 Instrument spectrometer design

The requirements for NFI1 are:

— high efficiency at 0.05-3 keV;
— good spectral resolution below 2 keV (< 2 eV, with a goal < 1eV);
— high count rate ability (> 5 kHz/pixel allows spectroscopy of ~ 10s mCrab sources in the initial configuration).

In addition to these scientific characteristics, the additional technical requirement is to maximise the operating temperature in order to relax the requirements on the heat lift of any cooling system. For this reason, a number of possible materials are considered which might form part of the lay-up of an STJ: Ta operating at ~ 300mK, Mo at ~ 90mK or proximised Hf at > 30mK. The choice between these materials will depend at a later stage on the system-level design constraints. To ensure a firm baseline, however, and a cooling technology different from that of NFI2 (Section 5), we shall assume an STJ array based on Ta.

The scientific aim of NFI1 is to obtain high-resolution spectra of high-redshift objects in a field 30 x 30 arcsec over the energy range 50-2000 eV with a resolution < 2 eV at 500 eV. Some response above 2000 eV is also anticipated. NFI1/2 will generally provide follow-up observations of specific objects detected in deep looks by WFI, which covers the full XEUS field. Such NFI observations are assumed to take place a number of weeks after the WFI observations. The broadband spectra of these WFI deep fields will form the criteria for selection between NFI1 and 2 as follow-up spectrometers.

The key capabilities and principle characteristics of NFI1 are:

Characteristic	*Requirement (Goal)*
Field of view	30 x 30 arcsec (0.5 x 0.5 arcmin)
Pixel size	0.6 arcsec (150 μm)
Number of pixels and format	48 x 48 (direct or matrix) (48 x 9 DROID)
Operating temperature (mK)	350 (Hf/Mo > 30mK)
Low-temperature stage	^{3}He sorption pump (Hf/Mo ADR)
High-low temperature stage (2K)	Mechanical cooler
Energy range (10% efficiency)	50-7000 eV
(80% efficiency)	100-2300 eV
Energy resolution	< 2 eV @ 500 eV (goal 1 eV)
Time resolution	5 μs

Here, a 48 x 48-pixel array of individual Ta-based STJs is assumed, while assuming that alternative schemes to simplify the chip and system design can be developed. This array is taken as a double-banked, staggered array in that two sides of the chip are used for lead placement and will have separate grounds. Thus, the fabrication of the array, in practice, reduces to the fabrication of smaller sub-arrays with respect to photolithography, lead placement and bond pads (Fig. 4.8). The array chip connects to an electrical harness via a substrate. This involves a considerable number of interconnections using gold/indium bump bond technology.

4.3 System description

The NFI1 instrument and its thermal interfaces are summarised at system level in Fig. 4.12. Essentially, it consists of two key units: a focal plane camera unit (NCH1), and a control and signal processing electronics unit (NCE1). The thermal control of the mechanical cooler is an integral part of NCE1.

The NFI1 camera head

The focal plane camera head (NCH1) houses the STJ array, filter wheel assembly, calibration sources and the full cooler unit (the mechanical cooler and adsorption cooler). An entrance door with an optical entrance door mechanism is a crucial part. This door opens and closes on command, so as to keep out contamination not only on the ground but at times such as the docking of MSC1 to DSC1, and in the vicinity of the ISS.

The NFI1 filter wheel assembly

A filter wheel assembly is located directly in front of the STJ array to suppress not only optical and UV fluxes but also near-IR flux by selecting appropriate filters. These filters, although optimised, will limit the instrument response at lower energies by increased X-ray absorption in the filters below a cut-off energy. The STJ array is kept in vacuum during launch by means of a door mechanism; a venting mechanism and a calibration source mechanism is included inside the door. The filter wheel has six

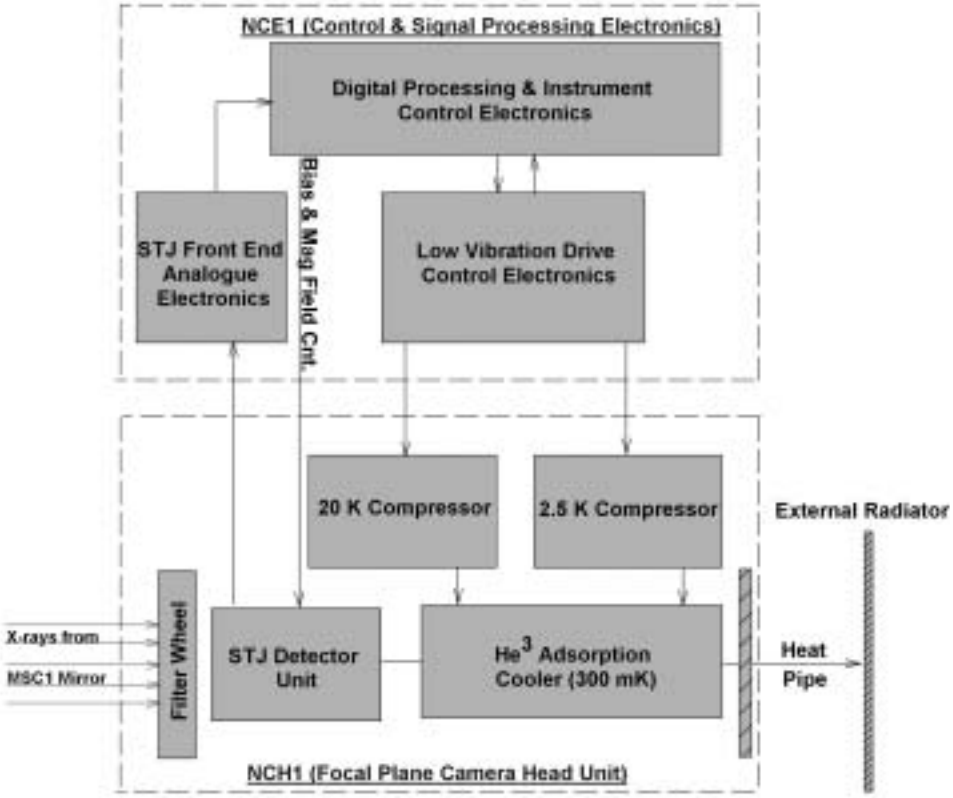

Figure 4.12. The proposed NFI1, highlighting the overall system-level aspects.

positions: four filters, a closed position and an open position. It will be driven by a stepper motor with redundant windings and redundant drive electronics. For positional control, redundant Hall sensors are used.

In addition to the conventional plastic/metal filters on the filter wheel, the unit will also contain an inductive grid fixed directly in front of the detector array in order to provide further rejection of the near-IR background.

Overview of the NFI1 cooling

This is a critical unit. The NFI1 instrument cooling system consists of a closed-cycle cooler with the following three main stages:

— a two-stage Stirling cycle pre-cooler with a base temperature of 20K;
— a Joule-Thompson (J-T) cycle cooler using ^{3}He as the working fluid pre-cooled by the 20K stage and acting as a 2.5K pre-cooler to the adsorption stage;
— an adsorption cycle cooler using ^{3}He to enable a base temperature of 350mK to be reached. This assumes that a Ta-based array is sufficient for NFI1. If an STJ array fabricated from a lower critical temperature superconductor such as proximised Hf or Mo is required or developed

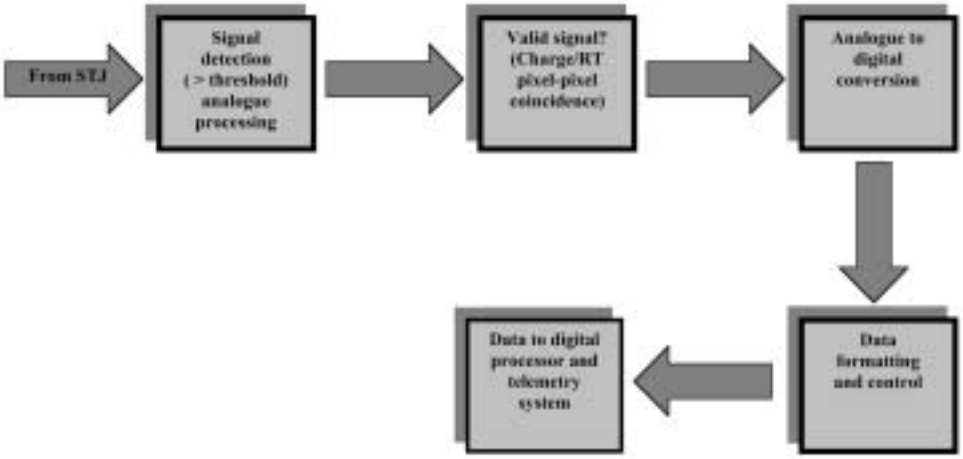

Figure 4.13. The STJ signal detection and processing chain.

then the base temperature would need to be > 30mK or ~ 90mK, respectively. Such a base temperature would be achieved by replacing the ^{3}He adsorption cooler by an ADR.

In addition, an external radiator may also be required. A full description of the cooling systems required for XEUS can be found in Section 6.

The NFI1 control and signal processing electronics

The NFI1 control electronics consists of analogue electronics situated as close to the camera head as possible (< 30 cm) and main control electronics, which provides the dual functions of signal processing and instrument control. A schematic of a typical signal detection and processing chain is shown in Fig. 4.13 for an individual junction (up to the ADCs).

The NFI1 control and digital signal processing electronics provide the interface between the detector and the front-end analogue electronics and the central processing computer. This interface follows a relatively conventional pulse height analysis topology. The analogue processing unit collects the charge produced by a photon interaction in the STJ array, amplifies the signal and applies applicable bandwidth limiting for an optimised signal-to-noise ratio. A decision process is applied to the processed analogue signal to verify its validity. Each valid signal is then converted to a digital number representing the energy of the photon detected, risetime (RT) of the signal, address of the pixel where the photon interacted and the time of the interaction.

The final digital information generated in this process is transferred to the spacecraft central computer for packaging and storage prior to transmission to the ground station. The main differences between this complete process and conventional analysis system is in the large number of signal processing

channels. The design will, in fact, be driven more by the quantity of electronics rather than by circuit technology.

In addition to the digital signal processing of the analogue electronics signals, the electronics performs the following instrument control functions:

— instrument magnetic field control and setting (for Josephson current suppression);
— instrument bias control;
— instrument cooling system control.

The NFI1 calibration sources

A calibration source is mounted above the filter wheel to shine through suitable apertures. The source has a low- and high-energy position with an off position between the two and is tuned by a small large-angle stepper motor, directly commanded by a bit pattern. The low-energy position allows the use of a pulsed light-emitting diode, while the high-energy position contains a cocktail of materials excited by an alpha-particle source. This produces fluorescent emission lines at 285, 500, 800 eV.

4.4 Resources

The overall instrument allocated mass is 175 kg. The masses of the individual units, together with their power and thermal requirements, are:

Unit	*Mass (kg)*	*Power (W)*	*Operating Temp.*
Camera Head	67	156	350±5mK (20±5°C)*
Control Electronics	108	146	20±10
Total	175	302	–

*refers to the actual operating temperature of NFI1; ( ) refers to the camera enclosure. During non-operational periods, NFI1 can be powered off and be held at 20°C. Includes the cooling system unit. Power refers to the requirement during an observation supplied at 28 V. The operating temperature of an Hf-based detector would be much lower (~ 30mK).

The power to the camera unit and control/signal processing electronics unit is provided by a converter in the control electronics unit. The cooling power is 20mW at 354mK. This is based on an ^{3}He sorption cooler coupled to a Joule-Thompson 2.5K stage with a cooling power of 3mW.

4.5 Performance

Detector efficiency

The efficiency of any detector is an important parameter when considering practical applications. Fig. 4.14 illustrates the efficiency of a Ta-based STJ as a function of photon energy for the case when the base film is ~ 300 nm thick and used as the primary detection element. In this case, the top film is

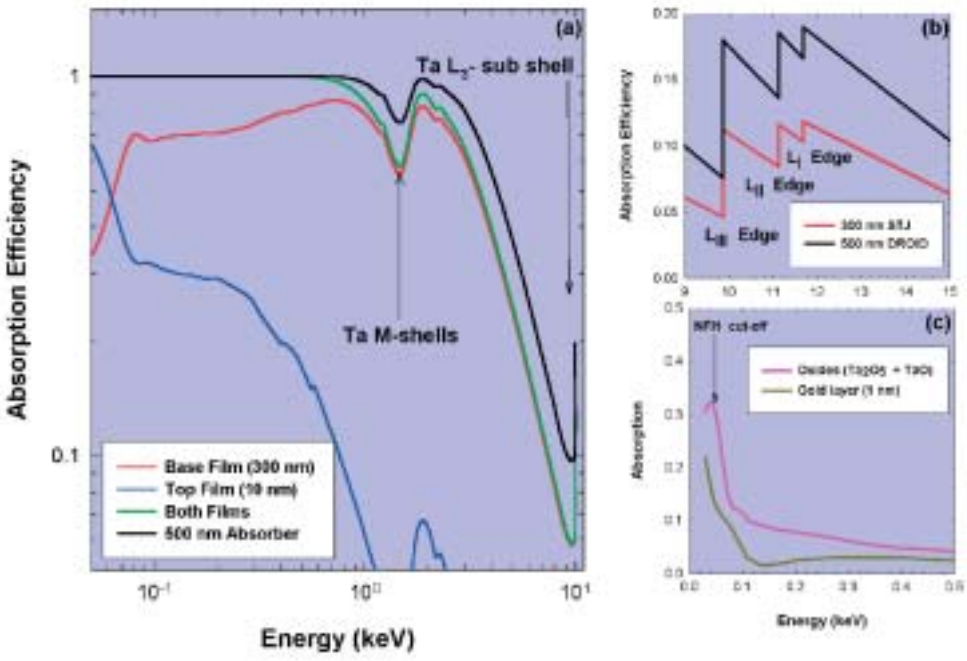

Figure 4.14. a: the overall detector efficiency for a Ta-based STJ array and a Ta 1-D DROID. The efficiency just above the Ta-L edge is also shown (b). The absorption at very soft X-ray energies in the oxide layers or in a thin protective gold coating is shown in (c).

only ~ 10 nm thick and its response is also indicated. For comparison, the efficiency of a thicker Ta film (500 nm), as may be applicable for a DROID-based detector, is also shown. At a photon energy of 1 keV, the efficiency for both films combined is ~ 85%, falling to ~ 10% at 7 keV. While the thickness of these films for an STJ can undoubtedly be grown to 500 nm, beyond this various loss mechanisms may become important such that the spectral resolution could be expected to degrade. This may, however, not be the case for the DROID configuration. In practice, the efficiency at the lower energies could be somewhat lower than that indicated in Fig. 4.14 owing to the fact that, unlike in the optical/UV, where back-illumination is the mode of operation, at X-ray wavelength the photon enters the detector through the front (front-illumination). This means that some fraction of the X-rays at lower energies would be absorbed in the top film oxide layer and also the top film, if the bottom film is used as the primary detection film, as well as the top contact. This latter point is important when considering arrays in which a significant amount of top contact wiring together with a SiO_x insulation layer is required. It may, however, be possible at least to stop the growth of the thin (4 nm) tantalum oxide through the introduction of a thin oxide-resistant surface coating such as gold (~ 1 nm) deposited during manufacture. The natural growth of oxides on the surface of the top film results typically in a 3 nm-thick Ta_2O_5 continuous layer on top of a 2 nm TaO layer which covers the Ta ~ 56% in clusters. The absorption in this complex oxide bi-layer is shown in Fig. 4.14(c).

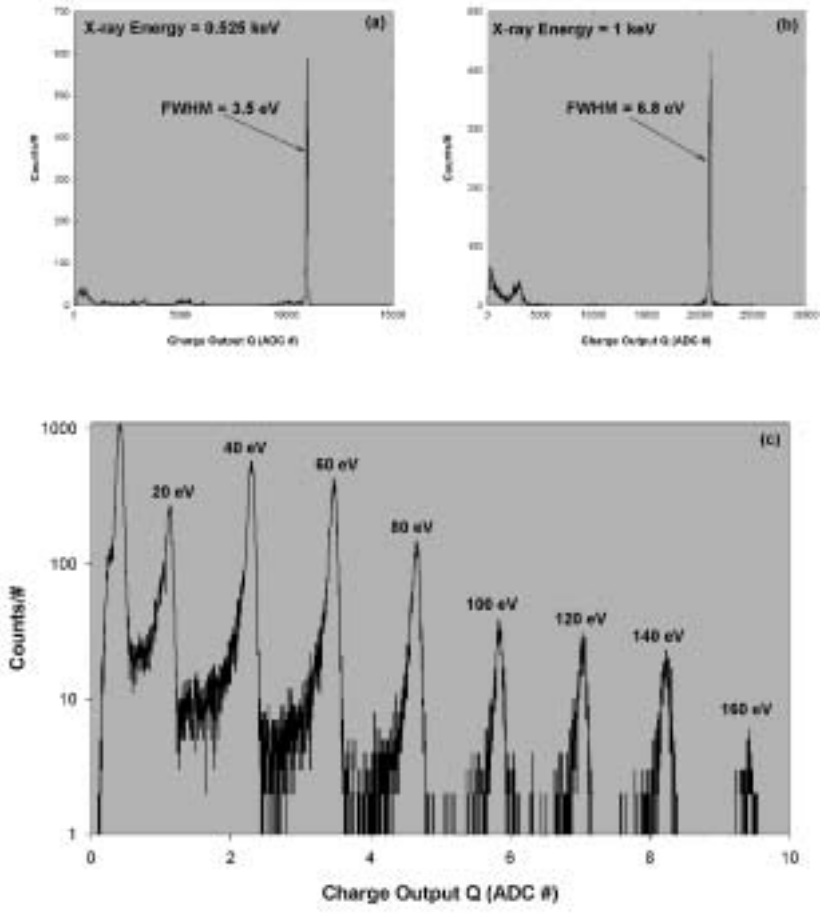

Figure 4.15. Pulse height spectra obtained from a single 25 µm pixel of a 6 x 6-pixel array of Ta-based STJs when illuminated by soft X-rays at energies of 0.525 keV (a) and 1 keV (b). Fig. 4.15(c) shows the single-pixel spectrum obtained when the array was illuminated at a synchrotron facility by radiation at an energy of 20 eV. In this case, the radiation was selected using a monochromator. The higher orders 2-8 up to 160 eV are easily detectable and resolved with such a detector.

The detector energy resolution

While the resolution has not yet reached the tunnel limits of a single STJ, indicated by Fig. 4.3, the situation is within about a factor of 2. The DROID concept, in contrast, has approached the tunnel limit with room for improvement by better placement of the base contacts. Fig. 4.15 illustrates the measured spectra from a Ta STJ forming part of a 6 x 6-element array illuminated by monochromatic radiation of various energies. Each device was 25 x 25 µm and consisted of two films each 100 nm thick. Only those photons absorbed in the base film that are separated from top film and substrate events by their distinct signal risetime are shown here. Typical resolutions $\delta E \sim 3.5$ eV at $E \sim 500$ eV were measured. While these data have not yet achieved the tunnel-limited resolution ($\delta E_T \sim 2$ eV at $E \sim 500$ eV), the

cause is determined to be a spatial variation in the detector gain which provides an additional variance dependent on the square of the photon's energy and which contributes to the overall variance.

The detector sensitivity to radiation

The radiation environment in space poses two potential issues of concern for the STJ arrays. First, charged particles interacting directly with the detector can cause permanent damage, either by degrading the barrier or the insulation of the contacts and the perimeter. Prototype STJ chips have been exposed to protons of energies 50-100 MeV up to a total dose of 11 krad, with the chip held at room temperature. No damage was observed when the chip was subsequently cooled to its operating temperature and exposed successfully to photons.

The second issue concerns the possibility of spurious signals from the STJ owing to particle irradiation. The proposed array is rather effective in the rejection of background events such as cosmic rays or soft electrons precipitating from the magnetosphere. The double sandwich structure implicit in the design of the STJ is a natural coincidence system. Laboratory measurements, involving a cobalt gamma-ray cell of controllable intensity to create Compton electrons, has shown that significantly different risetimes and amplitudes are produced by an STJ from such events compared to X-ray photons. Particle interactions deposit most of their energy in the substrate, but this can still produce quasiparticles owing to the transport of phonons into the junction volume with sufficient energy to break Cooper pairs. However, these events may be discriminated by their risetimes and amplitudes. In addition, substrate phonons produced by charge-particle interactions propagate to more than a single pixel. Thus, further particle-event rejection can be accomplished using an anti-coincidence veto between adjacent pixels.

The detector count rate limits

Some sources observed with XEUS will be rather intense, given the large collecting area of the telescope below 2 keV. NFI1 should therefore have the capability to observe rather high count rates. Each pixel in the array is limited in its temporal response by the tunnel time of the detector and the relaxation time required to convert the photon energy into charge carriers. In addition to these detector time resolution limits, the electronics processing chain (through the pulse shaping time) will introduce a certain deadtime. Fig. 4.16 shows the spectral response of a Ta-based STJ to two different soft X-ray count rates and a shaping time of 2.6 μs. At an input rate of 10 kHz the resolution has degraded to 6.2 eV from a value of ~ 3.9 eV at 1 kHz. Note in Fig. 4.16, apart from the increase in distortion of the spectral line at 10 kHz (the skewed distribution towards lower energies), the small number of events that are introduced at higher energies (to the right of the main spectral peak) in the case where the junction is irradiated at a 10 kHz rate. These are pile-up events. Below 5 kHz, no serious degradation in energy resolution or major pile-up (double events) is observed.

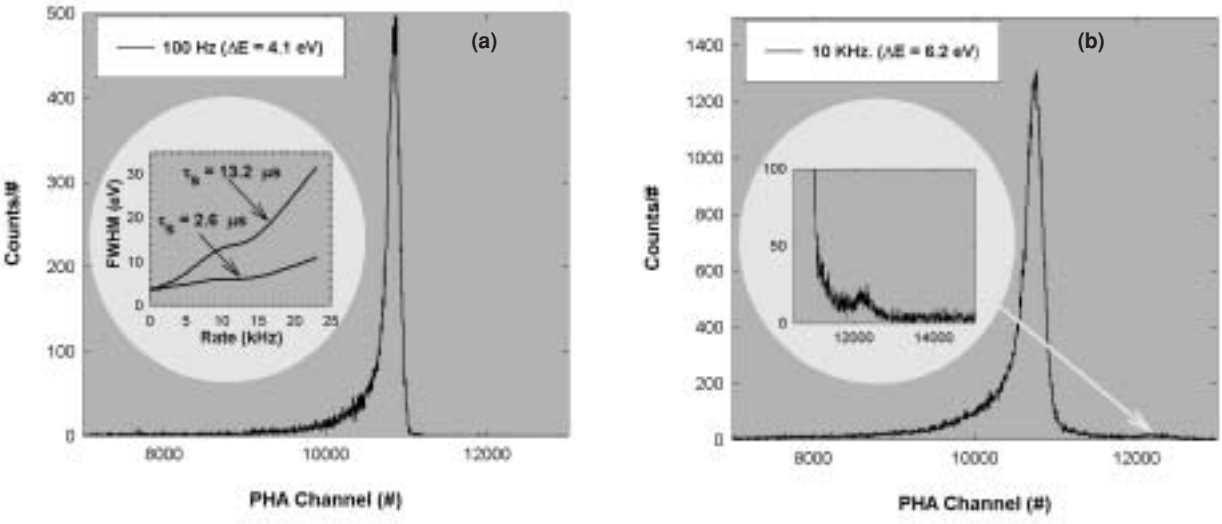

Figure 4.16. The spectral response of a small Ta-based STJ to soft X-rays (277 eV) for two different X-ray intensities: (a) 100 Hz and (b) 10 kHz. The inset of (a) shows the degradation of energy resolution as a function of input rate for two different shaping times, while the inset of (b) shows a zoom of the double event/pile-up region.

For DROIDs, the situation is significantly worse. Ideally, the above count rate limitations per single device would translate to the area covered by the whole DROID. However, the pulse decay time in a DROID is longer than for a single junction, and the time coincidence technique of event reconstruction competes with pile-up. For example, in a 2 mm-long bar, an event risetime is not only 10x longer than for a single-pixel device, but changes with position along the bar. Engineering the diffusion constant to higher values by thickening the bar allows an increase in efficiency, but at the expense of lowering tunnel probability and thus increasing tunnel noise. Typically, then, we expect the count rate capability of a 1-D DROID with a relatively large number of spatial elements (100 μm-resolution elements in a 2 mm bar) to scale inversely with a pile-up limit of the X-ray point source spot size.

5 NFI2: the Narrow-Field Medium-High-Energy X-ray Imaging Spectrometer

The second narrow-field imager, NFI2, is optimised for the 0.5-7 keV energy band, but it will operate up to at least 15 keV with slightly degraded efficiency and energy resolution. Up to intermediate redshifts ($z < 3$), this energy range contains the majority of diagnostic X-ray lines, which can be observed largely unabsorbed by the interstellar medium of our own Galaxy. At larger redshifts, most of the lines move to energies below 1 keV, which makes NFI1 more suited to the deepest observations.

5.1 The microcalorimeter instrument

Microcalorimeters have proven performance from the optical to the X-ray band. As a baseline, the NFI2 instrument will be optimised for the 0.5-7 keV energy band to complement the low-energy, 0.05-3 keV, NFI1 instrument optimised for the energy range below 2 keV. The NFI2 microcalorimeter could, however, be designed for the full 0.05-7 keV energy band, though at slightly degraded performance.

Within the above energy range, microcalorimeters equipped with a normal to superconducting phase-transition thermometer, usually known as transition edge sensors (TESs), have recently shown excellent performance. The National Institute of Standards and Technology (NIST; Boulder, USA) has obtained an energy resolution of 2 eV FWHM for the 0.25-3 keV energy range and 4.5 eV FWHM at 5.89 keV combined with a count rate capability of 50-500 s^{-1} and good detection efficiency. In Europe, the Space Research Organization Netherlands (SRON; Utrecht, NL) has measured an energy resolution of 3.9 eV FWHM for 5.89 keV X-rays with a count rate capability of ~ 500 s^{-1} (100 μs fall time). Typical operation temperatures are 70-100mK.

The large thermal coefficient of resistance, α, of the steep phase-transition thermometer, in combination with voltage biasing, allows for operation of the TES in extreme negative electro-thermal feedback, thereby enabling:

— stable operation, almost as a self-biasing null detector;
— count rate performance up to 500 s^{-1}, since feedback shortens the pulse decay time;
— excellent energy resolution for rather large heat capacity, thereby enabling the use of metallic absorbers.

Only results on single-pixel devices are currently available. Although some initial designs for imaging arrays have been published, considerable developments for the sensor and readout electronics are required to create the 32 x 32-pixel imager required for XEUS.

Operating principle

A microcalorimeter (Fig. 5.1) consists of an absorber for photons or particles,

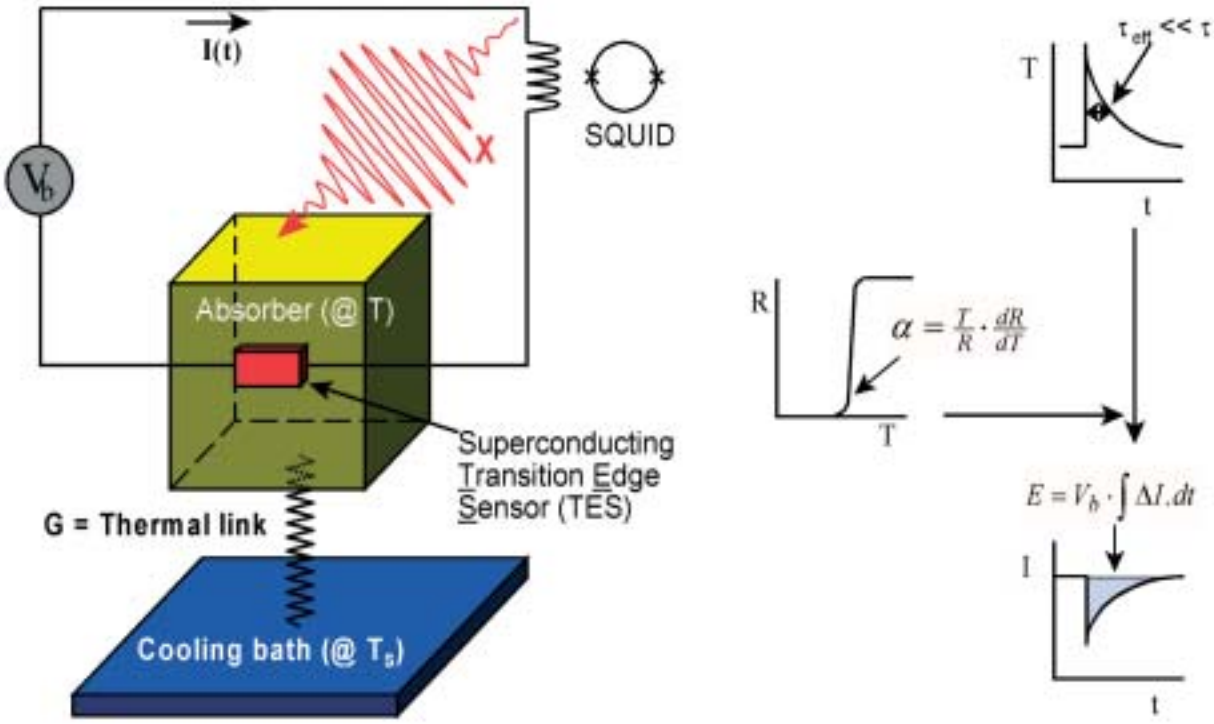

Figure 5.1. Microcalorimeter schematic.

characterised by its heat capacity C [J K^{-1}] at temperature T [K], a resistive thermometer R (T) [Ω], characterised by its thermal coefficient of resistance α:

$$\alpha = \frac{d\ln R}{d\ln T} = \frac{T}{R}\frac{dR}{dT} \tag{5.1}$$

and a link to the heat bath, characterised by a dynamic heat conductance $G = \mathrm{d}P/\mathrm{d}T$ [W K^{-1}]. P is the bias power flowing from the sensor at temperature T to the bath at temperature T_s. The thermal time constant τ [s] of the device is given by $\tau = C/G$, where C is heat capacity. For thermometers with a positive α, which is the case for a TES, a constant voltage bias creates negative electro-thermal feedback. In that case, the thermometer is read out by measuring the current I [A]. Given the low impedance of the thermometer, a superconducting quantum interference device (SQUID) is used as current amplifier.

The bias voltage V_b drives the detector temperature T well above the bath temperature T_s through dissipation of electrical bias power

$$P = \frac{V_b^2}{R(T)} = IV_b \tag{5.2}$$

in the thermometer resistance. The resulting negative electro-thermal feedback with DC loop gain

$$L_0 = \frac{\alpha P}{GT} = \frac{\alpha\,[1 - (T_s/T)^n]}{\mathrm{n}} \approx \frac{\alpha}{\mathrm{n}} \tag{5.3}$$

when $T >> T_s$, creates stable self-biasing. In equilibrium,

$$\frac{V_b^2}{R(T)} = \mathrm{K}(T^n - T_s^n) \tag{5.4}$$

with K and n ≈ 3.2 constants defining the heat transport over the heat link. The electro-thermal feedback also reduces the thermal time constant τ to an effective time constant

$$\tau_e = \frac{\tau}{1 + L_0} \tag{5.5}$$

which is extremely relevant for high-count rate operations.

An X-ray of energy E incident on the absorber will be absorbed and thermalised. The temperature of the detector element will rise within less than 1 μs by $\Delta T = E/C$. Subsequently, the excess heat is mainly compensated for by a temporal reduction of the electrical bias power P, so that the sensor returns exponentially to its set point with a time constant τ_e. Given the constant bias voltage, the reduction in bias power P is measured as a current change $\Delta I\,(t)$ by the SQUID amplifier. In the case of voltage bias with current readout, the closed-loop current responsivity S_I of the microcalorimeter equals:

$$S_I = -\frac{1}{V_b}\frac{L_0}{1 + L_0}\frac{1}{1 + i\omega\tau_e}\ [A\ W^{-1}] \tag{5.6}$$

In the case of high loop gain, the responsivity approaches $1/V_b$ and the energy of the measured X-ray is approximately given by

$$E = -V_b \int \Delta I(t)\ \mathrm{d}t, \tag{5.7}$$

the integral over the current change divided by the responsivity.

Design and performance parameters

The basic performance parameters for NFI2 are energy resolution, energy range, detection efficiency and speed. The available design parameters are heat capacity C, thermal coefficient of resistance α, heat conductivity G and transition temperature T. To a first approximation, the performance parameters are a function of C/α.

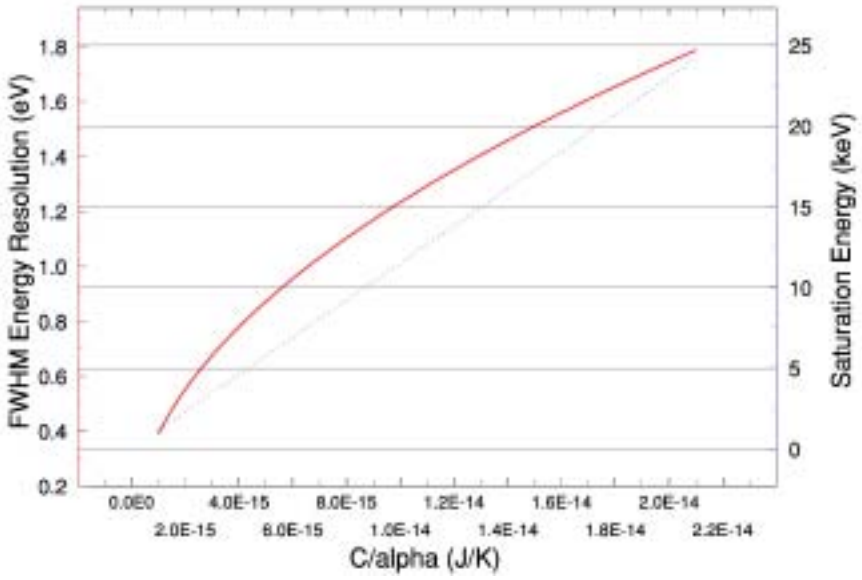

Figure 5.2. Energy resolution and saturation energy of a TES-based microcalorimeter as a function of *C*/α. The curves are calculated for an operational temperature of 100mK and a biaspoint defined by *r* = 0.1.

The energy resolution is limited by the presence of phonon noise between the sensor and the heatbath and Johnson noise of its thermometer resistance. The noise of the SQUID output amplifier is, in general, negligible. The energy resolution is given by:

$$\Delta E_{FWHM} = 4\sqrt{\ln 4}\,(\gamma n)^{\frac{1}{4}}\sqrt{kT^2\frac{C}{\alpha}} \tag{5.8}$$

with $\gamma \approx 0.5$ accounting for the reduction in noise due to the thermal gradient over the heat link, and n = 3.2 the power law exponent for the dependence of the thermal conductance of a Si_xN_y membrane on temperature. k is Boltzmann's constant.

If we approach the $R(T)$ relation of the thermometer by an exponential function, i.e.

$$R(T) = R_N \exp[(T - T_C)/\Delta T] \tag{5.9}$$

for $T \leq T_C$, actually quite close to measurements under voltage-biased conditions, then the saturation energy for the sensor becomes:

$$E_{sat} = -\ln(r)T\frac{C}{\alpha} \tag{5.10}$$

A photon with the saturation energy drives the thermometer normally. Higher energies will have a pulse shape with a flat top. The parameter $r = R_{bias}/R_N$ defines the biaspoint.

The energy resolution and saturation energy are given in Fig. 5.2 as a function of C/α for a temperature $T = 100$mK and $r = 0.1$. For $C/\alpha = 1.3 \times 10^{-14}$ J K^{-1}, the saturation energy equals 15 keV and the energy resolution will be about 1.4 eV FWHM. So, for XEUS, there is some design margin if the theoretical energy resolution (Eq. 5.8) for TES-type microcalorimeters can be obtained.

We have to make sure that the above value for C/α allows for sufficient absorption material to meet the requirements on absorption efficiency for the optimised 0.5-7 keV energy range and the extension to 15 keV. This is discussed later.

Having frozen the values for C/α, the only parameter available to adjust the speed of the sensor is the heat conductance G to the bath. Obviously, G is related to the power flowing to the bath. In the case of $T_s << T$ the power $P = GT/\mathrm{n}$. So the response time is given by:

$$\tau_e = \frac{C}{G}\frac{1}{L_0 + 1} \approx \frac{C\mathrm{n}}{G\alpha} \approx \frac{C}{\alpha}\frac{T}{P} \qquad (5.11)$$

So for $C/\alpha = 1.3 \times 10^{-14}$ J K^{-1} and $T = 100$mK, the bias power per pixel has to be 13 pW in order to get an effective signal decay time of 100 μs.

Development status

The following paragraphs summarise the state-of-the-art for TES X-ray microcalorimeters. The focus is on single-pixel devices, since the development of arrays is just starting and little information has been published so far.

The thermometer

Normal-to-superconducting phase-transition thermometers with a transition temperature T_c between 15mK and 1.0K are generally made of proximity bilayers of a superconducting and normal metal, so that the transition temperature can be tuned by the respective layer thicknesses. So far, bilayers of Al/Ag, Al/Cu, Ti/Au, Ir/Au, Mo/Au and Mo/Cu have been developed and tested. In addition, single layers of W (15mK and 80mK) and Ti (450mK) have been used successfully. The transition width ranges typically from 0.5mK to a few mK, which results in a thermal coefficient of resistance α between 20 and 200. So far, the Al/Ag and Al/Cu bilayers have shown long-term instabilities, while other materials are more stable. The Ti/Au thermometers produced at SRON are perfectly stable over periods in excess of one year. The Mo-based thermometers used by NIST and NASA Goddard Space Flight Center (GSFC) are expected to be even more stable than Ti/Au. The transition temperature is reproducibly set by the

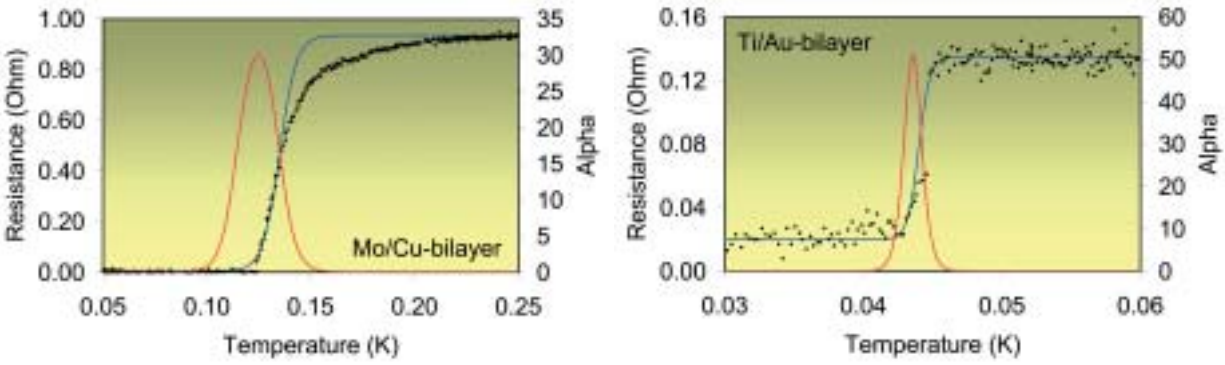

Figure 5.3. Measured *R*(*T*) characteristic of Mo/Cu and Ti/Au bilayer thermometers. The blue solid line is an analytical fit used to derive the thermal coefficient of resistance (alpha) shown in red.

thicknesses of the two layers and can reasonably be predicted with theories on the proximity effect.

Some measured $R(T)$ characteristics for Ti/Au and Mo/Cu bilayers fabricated at SRON are shown in Fig. 5.3. When voltage-biased, the rather high current density through the thermometer widens the transition width ΔT and thereby reduces α. This results in a larger dynamic energy range, $E_{SAT} \approx C\Delta T$, and a smaller loop gain than expected on the basis of the $R(T)$ curves, measured with a small current, of the thermometers as shown in Fig. 5.3.

Under voltage-bias conditions, the $R(T)$ curves can be approximately described by an exponential relation for which $\alpha = T/\Delta T$. Typically $\alpha \approx$ 20-40 for most of the experimental devices. Very little effort has gone so far into the design and production of thermometers with an engineered α.

Absorber and sensor layout

TES microcalorimeters consist of a radiation absorber coupled to a phase-transition thermometer. Absorbers for TES devices have been routinely made of normal metals such as Au, Ag and Cu. Absorbers have also been successfully made from the semi-metal Bi because of its about 20× lower heat capacity than normal metals and high X-ray stopping power. Future research on very low heat capacity superconducting absorbers (Sn has been used very successfully in NTD-Ge-type microcalorimeters) should be seriously considered.

The sensor is positioned on top of a Si_xN_y membrane, which serves as the weak heat link to the bath. Electrical connections to the thermometer and the absorber are made by superconducting leads, which have a negligible contribution to the thermal transport to the bath. Given the high packing density required for an imaging array of microcalorimeters, a stacked configuration with the absorber on top of the thermometer is the most promising geometry.

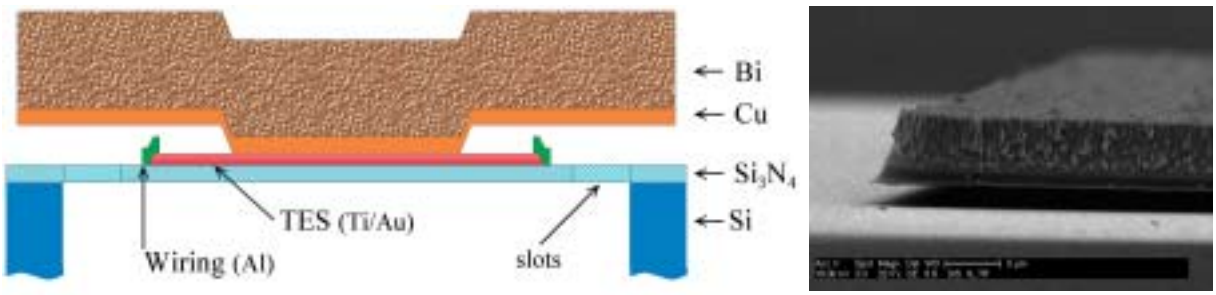

Figure 5.4. Cross-section of a stacked sensor. The thermometer is deposited on a Si_xN_y membrane and electrically connected by superconducting wiring. The absorber consists of a Cu base-layer with Bi on top. The pixel size for XEUS will be 240 × 240 µm. In the micrograph at the right, the free overhang of a produced Cu-Bi mushroom absorber is shown.

A design under development at SRON is shown in Fig. 5.4. The mushroom-shaped Bi absorber is connected to a Cu backing layer, which contacts only the central part of the thermometer. Since the T_c of the thermometer is suppressed under the Cu contact, only the sides of the bilayer around the absorber pedestral act as the thermometer. The groups at NIST and GSFC have deposited Bi directly onto the Mo/Cu thermometers without affecting the transition temperature.

Energy resolution and event time

The best energy resolutions measured in the optical, 0.1-3 keV X-rays and 5.9 keV X-rays are 0.16 (Stanford Univ., USA), 2.0-2.4 (NIST, GSFC) and 3.9-6.1 eV (NIST, GSFC, SRON).

Figure 5.5 shows a pulse height spectrum measured at SRON for 5.9 keV and 6.4 keV X-rays with a microcalorimeter consisting of a 310 x 310 µm Ti/Au thermometer with T_c = 95 mK and a 4.5 µm-thick Cu absorber of 0.1 x 0.1 mm. Using well-established high-resolution measurements of the Mn-K$\alpha_{1,2}$ doublet, the data can be fitted with a detector energy resolution of 3.9 eV FWHM. Addition of the Bi absorber will only slightly enhance the heat capacity and is expected to have a marginal influence on the energy resolution. So far, the best energy resolution measured with a Cu-Bi mushroom absorber equals 4.9 eV FWHM.

The event time of these microcalorimeters ranges from a few µs for the optical devices up to 2 ms for the X-ray devices. The SRON device combines 3.9 eV energy resolution at 5.9 keV with an event time of 100 µs, thereby enabling count rates up to 500 s^{-1}.

Based on information in available literature, the measured energy resolution by the various groups worldwide can be normalised to $2.35\sqrt{k}T^2C$, which gives normalised resolutions between 0.5 and 1.2 . The loop gain L_0 for these data ranges from about 1 to 20. In general, the measured energy resolution

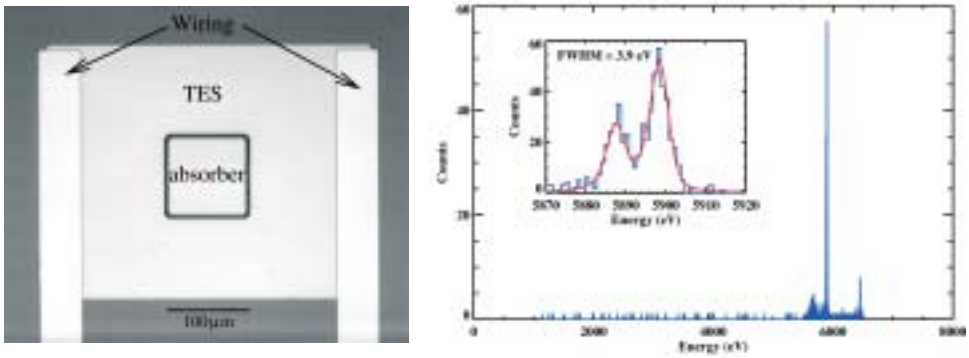

Figure 5.5. Pulse height spectrum for Mn-Kα and Kβ X-rays. The insert shows a fit with 3.9 eV FWHM energy resolution through the Mn-K$\alpha_{1,2}$ doublet at 5.89 keV. The micrograph shows the TiAu thermometer, its Nb leads and the central square Cu absorber.

falls short of the expected energy resolution by typically a factor 2-3 for 5.9 keV X-rays. This is partly related to the measured presence of excess noise in most of the current devices employed at the various research groups. In addition, it might relate to the calculation of expected resolution by applying the small signal limit that is not fully applicable for the 5.9 keV X-rays.

The measured pulse shortening turns out to be in agreement with the α-value derived from the *I-V* curves for a specific device and the resulting loop gain L_0 in excess of 10.

Imaging spectrometer

Development work on imaging TES spectrometers is just starting. Some preliminary designs and predicted performance data have been published. The imaging aspects, with regard to the sensor and the multichannel readout electronics, will form the major part of the development work for a XEUS imaging spectrometer. The following sections address these issues.

Status summary

Very good energy resolutions (2.0 eV FWHM at 1 keV and 3.9 eV FWHM at 5.9 keV) have been realised for pixels close to what will be required for XEUS. These energy resolutions fall short by a factor 2-3 of the theoretical expected resolution given by Eq. 5.3 and shown in Fig. 5.2. The discrepancy is due to a combination of effects, including excess noise, imperfect data filtering and comparison of large signal data with small signal models. For a 2.5-factor energy resolution discrepancy, one should design for 2/2.5 = 0.8 eV FWHM resolution, which results in a saturation energy of 5 keV (see Fig. 5.2).

With respect to the event time, 100 μs is regularly obtained. Much faster performance will be seriously limited by degradation of the thermometer steepness α, owing to enhanced bias currents, and increased demands on the SQUID amplifier dynamic range and SQUID multiplexer bandwidth.

5.2 Imaging spectrometer design

There are two different approaches for designing an imaging spectrometer. One employs an array of single pixels, by which advantage is taken of the optimum performance (high energy resolution and good count rate capability) attainable in a single pixel at the expense of sensor, wiring and readout electronics complexity. The other approach is the use of intrinsic 1-D or 2-D imaging spectrometers, which might enable reduction of the complexity of the instrument at the expense of slightly degraded energy resolution and a significant degradation of the count rate performance. So the core of the NFI2 instrument will be realised as a pixel array. However, the field of view might be extended by adding a surrounding sensor making use of intrinsic 1-D or 2-D imaging. The complexity of single-pixel array designs can, to some extent, be reduced by signal multiplexing.

The requirements

The requirements for NFI2 on XEUS are:

Spatial resolution element – pixel size	1 arcsec – 240 μm
Field of view – array size	0.5 arcmin – 32 x 32 resolution elements
Energy range – detection efficiency	0.5-15 keV – > 90% for 1-7 keV
FWHM energy resolution	2 eV @ 1 keV and 5 eV @ 7 keV
Count rate – effective time constant	> 250 $c\,s^{-1}$ pix^{-1} – 100 μs
Background rejection	> 95% (minimum ionising) particles

The TES design is fairly tolerant to the pixel size. Changes towards smaller pixel size will enable reduction of the heat capacity, which can be used to improve on energy resolution and/or high-energy detection efficiency. Increasing the pixel size will degrade the energy resolution by the increase of heat capacity from the absorber. This might, however, be circumvented by the development of superconducting absorbers, like Sn or Ta, with very low heat capacity.

A field of view larger than 32 x 32 pixels is presently considered too complex to propose. Given, however, the timelining for XEUS (around the middle of the next decade), it is quite likely that appreciably larger arrays can be realised by that time. Even a larger field of view might be possible with the use of 1-D or 2-D designs for the outer parts of the sensor.

As indicated above, the TES has shown excellent energy resolution from the optical through the X-ray range. The NFI2 performance will be optimised for the 0.5-7 keV energy range by selection of an absorber with 90% absorption efficiency up to 7 keV and low enough heat capacity to meet the resolution requirements at 1 keV and 7 keV. The low-energy range of XEUS will, with a fair overlap, be addressed by the NFI1 instrument, and NFI2 will have very adequate response up to 15 keV.

To meet the energy resolution requirements, the pixel heat capacity and operating temperature are the key design parameters. Conservative design criteria are taken for the purpose of this document. Based on current status,

an energy resolution degradation of a factor 2.5 from optimum (see Section 5.3 and Fig. 5.2) is assumed.

With an effective time constant of 100 μs, a count rate of at least 500 c s^{-1} pix^{-1} is considered feasible without serious degradation of the energy resolution. Given the spatial oversampling of the focal image, the camera can handle sources up to a strength of about 1 mCrab, that is ~ 1000 c s^{-1} for the zero-growth XEUS.

So far, only the background rejection of minimum ionising particles through the use of energy discrimination has been considered.

Pixel array design

The strongest design drivers for a pixel-array spectrometer are the required electrical connections to each pixel, the thermal connection of each pixel to the bath and the minimisation of both electrical and thermal cross-talk between neighbouring pixels.

Design alternatives

The design of an array of microcalorimeters is, in principle, a 'copy and paste' process of an optimised single-pixel design. The design of such an array pixel is, however, bounded by a number of additional constraints:

— each pixel should have the same thermal link to the heat bath, independent of the amount of pixels in the array;
— given the tight efficiency requirements, the pixels should be closely packed, limiting the space available for electrical wiring and thermal connections to the heat bath;
— the electrical and thermal cross-talk between the pixels must be small enough not to degrade the energy resolution;
— fabrication feasibility and ruggedness against thermal cycling play a larger role than for single pixels.

These conditions, together with the requirements on energy resolution, efficiency and count rate lead to several different design options. These options are predominantly characterised by differences in the mechanical layout.

Placing all the pixels on one large membrane has been considered. Such a structure is, however, highly vulnerable – a crack can ruin the whole array. Furthermore, for uniform cooling, normal metal cooling lines to each pixel would be necessary. Experiments with single pixels have shown that such cooling lines, attached to the thermometer, have an adverse effect on the energy resolution. Another possibility is to place all the pixels on a metal substrate and use the Kapitza resistance between the device and the substrate as the thermal link. This requires very low operating temperatures (< 50 mK) and even lower bath temperatures (< 25 mK). Furthermore, there are very considerable stress issues related to this route.

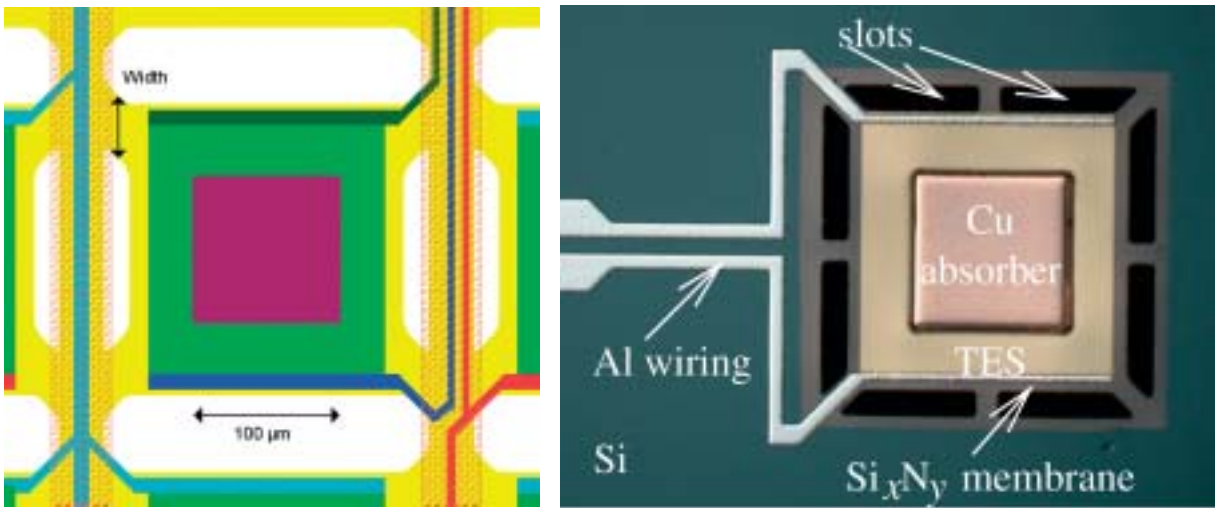

Figure 5.6. Basic layout of a sensor pixel. On the left, the hatched areas represent the Poly-Si or Si-support beams. The thermometer (green) on top of the Si_xN_x-membrane (yellow) is electrically connected by leads running over the support beams. The membrane is attached to the support by four legs, dimensioned to the designed heat conductance. The absorber foot is indicated by a purple square in the middle of the thermometer. On the right is a picture of a realised single pixel with a slightly different design.

So the most likely routes make use of individual SixNy membranes per pixel supported by Si support bars, providing the mechanical stability and the thermal link to the bath.

The SRON/MESA+ Research Inst. (Univ. of Twente, NL) collaboration is working on two basically different designs for the Si support structure, while the pixel layout is almost the same. The pixel design uses a slotted membrane in order to control the conductance to the heat path. A top view of the basic layout is shown in Fig. 5.6, while Fig. 5.4 shows a side view.

The two basically different design options for the Si-support structure are summarised in Fig. 5.7. In the upper part, the membranes are suspended between a set of long narrow bars of Si, formed by wet etching of [110]-oriented wafers. The vertical sides of these ribs are [111]-oriented and scanning microscopy shows that the surface roughness is smaller than 0.1 µm. This will allow for radiative phonon heat transport with a mean free path of 1-10 µm.

In the lower two structures, the Si_xN_y layer is not directly grown on the Si wafer. Instead, a layer formed of a sacrificial material is placed between. At a later stage, the sacrificial layer is removed to leave shallow boxes below a Si_xN_y membrane. The boxes can be above or below the Si-wafer level. The obvious advantage of this shallow box route is its strength and better heat conductivity. In addition, it allows for positioning of the wiring under the

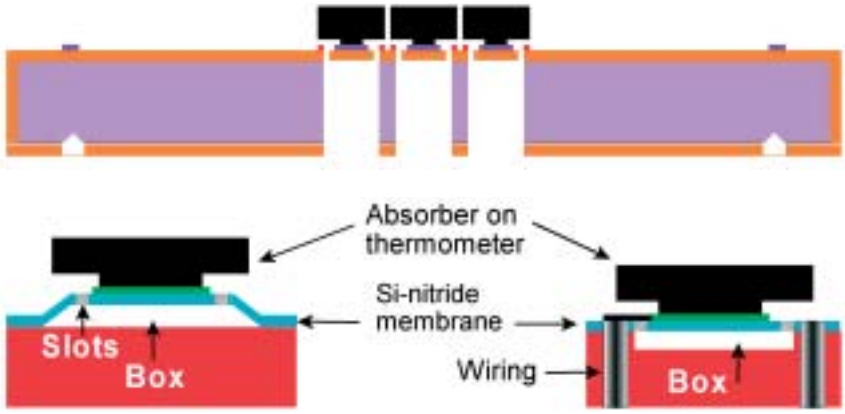

Figure 5.7. Two options for the fabrication of an Si-support structure. The upper one shows long narrow Si-bars wet-etched in [110]-oriented Si. The bottom one shows shallow box structures created by the removal of a sacrificial layer.

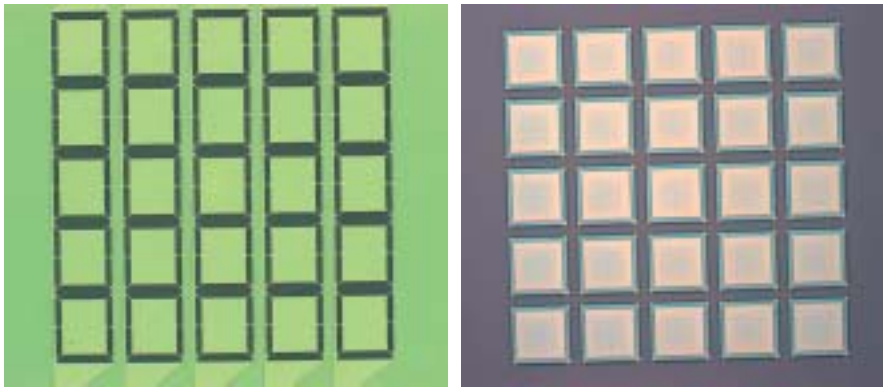

Figure 5.8. 5 x 5 structured membrane pixel arrays with 250 µm pitch. The left wafer is produced by wet etching in [110] Si, while the right one is made by the use of a Poly-Si sacrificial layer.

pixels, i.e. at the bottom level of the shallow boxes. Another wire routing option, in principle valid for all options shown, uses wafer feedthroughs, allowing for bump-bonding at the bottom. This is illustrated at the bottom right option of Fig. 5.7.

Examples of production trials of 5 x 5 pixels along both routes are shown in Fig. 5.8. It entails here only the production of the structured membranes.

Performance estimates

Making use of Eq. 5.8, we can estimate the performance once the heat capacity is known. The heat capacity estimates for a sensor with a 160 x 160 µm TiAu thermometer and 240 x 240 µm Cu-Bi absorber are 2.8×10^{-14} and 2.7×10^{-13} J K^{-1}, respectively. In that case, the absorber

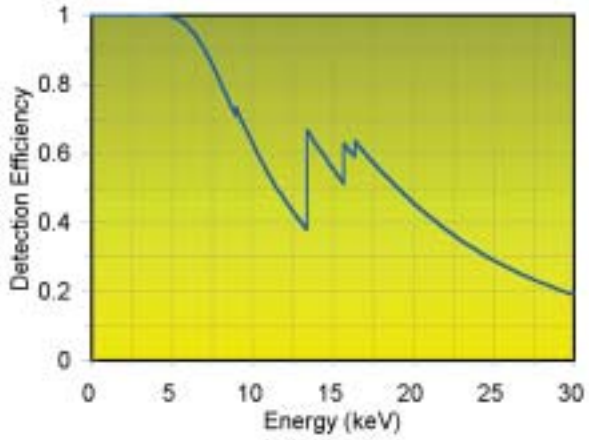

Figure 5.9. Absorption efficiency of a detector pixel with an absorber consisting of 0.21 µm Cu and 7 µm Bi.

consists of 0.21 µm Cu and 7 µm Bi, thereby meeting the 90% absorbtion efficiency requirement up to 7 keV. The detector absorption efficiency as a function of X-ray energy is given in Fig. 5.9.

The theoretical energy resolution for such a pixel, assuming $\alpha = 30$, is 1.2 eV FWHM and the saturation energy is 12 keV for $T = 100$mK (Fig. 5.2). In practice, the resolution would be ~ 3.0 eV for the current development status. Transformation of the whole sensor to operation at 80mK would reduce the experimental resolution to 2.1 eV, quite close to the XEUS requirent. The saturation energy thereby reduces to 9.6 keV. In order to create an event speed of 100 µs, the bias power per pixel has to be set to (Eq. 5.11) 8 pW per pixel, well in the range possible using Si_xN_y membranes. A summary of design and performance parameters is:

Pixel heat capacity	2.4×10^{-13} J K^{-1} at 80mK
Absorber layout	0.21 µm Cu + 7.0 µm Bi
Absorbtion efficiency	90% up to 7 keV
Thermometer	160 x 160 µm TiAu with $\alpha = 30$, $T_c = 80$mK
Energy resolution (FWHM) for small signals	2.1 eV with theoretical limit of 0.84 eV
Energy resolution (FWHM)	2.3 eV at 1 keV and 3.3 at 7 keV
Saturation energy	9.6 keV
Fall time for small signals	100 µs
Fall time	120 µs at 1 keV and 245 µs at 7 keV
Bias power per pixel	8 pW

Most of the response values given above, and all of those given in Section 5.1, hold for the case of a small-signal model. For larger signals, the pulse fall times slowly increase and also, subsequently, the energy resolution. This is illustrated in Fig. 5.10. The pulse shapes are given in units of normalised

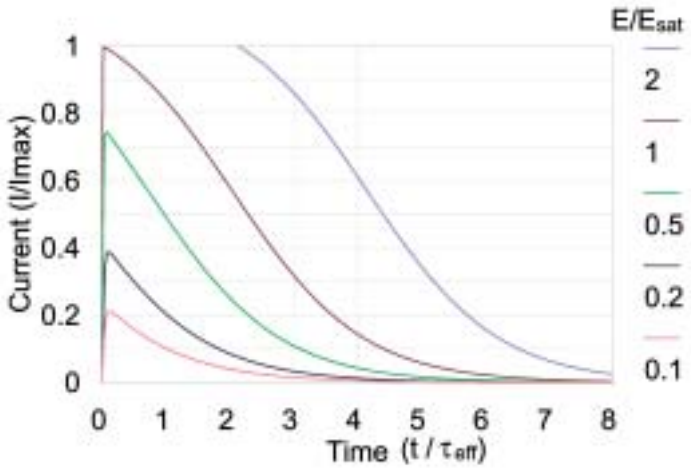

Figure 5.10. Normalised pulse shape as a function of normalised time for several normalised X-ray energies.

current change against normalised time for various normalised X-ray energies. It is clear that the 1/e fall time increases with X-ray energy and that above the saturation energy the pulse shapes have a flat top. Fitting the various fall times as a function of energy produces

$$\frac{\tau(E)}{\tau_{eff}} = \frac{2E}{E_{sat}} + 1 \tag{5.12}$$

This results in a 120 μs fall time at 1 keV and 245 μs at 7 keV. This also results in a degradation of energy resolution:

$$\frac{\Delta E(E)}{\Delta E} = \sqrt{\frac{\tau(E)}{\tau_{eff}}} \tag{5.13}$$

The values at 1 keV and 7 keV were given above in the summary of design and performance parameters.

1-D and 2-D imaging designs

The readout of single-pixel array designs could be simplified by using either 1-D or 2-D imaging spectrometers. In such a detector, the heat created by the absorption of an X-ray photon is read out by either two (1-D) or four (2-D) voltage-biased thermometers. The energy is derived by adding the output signals, while the position is determined by the differences in signal risetime or amplitude.

Using 1-D or 2-D imaging spectrometers will affect two important performance parameters. The most directly impaired is the count rate

performance. At present, single-pixel devices have effective fall times of, at best, 100 μs and can handle up to about 500 count s^{-1} without serious degradation of the energy resolution. Since imaging spectrometers are expected to have similar time constants, a 2-D n x n imaging spectrometer can handle only ~ $500/n^2$ c $s^{-1}pix^{-1}$. Since for XEUS the count rate performance is very important, strong preference is given to single-pixel arrays. Almost certainly, the energy resolution of a 1-D or 2-D imager will be impaired by the increase of the absorber heat capacity and the fact that the energy has to be derived from the addition of two or four outputs.

The baseline design for the XEUS NFI2 instrument is therefore a single-pixel array spectrometer.

5.3 Readout electronics

The XEUS scientific requirements can be translated into requirements for the readout electronics. The most relevant for one TES pixel are:

Input current noise	18 β^{-1} pA/√Hz
Dynamic range	1.2 x 10^6 β √Hz
Bandwidth (small/large signal)	10/100 kHz
Slewrate	20 A s^{-1}

The SQUID noise level is chosen to be a factor β ~ 3 lower than that of the TES.

Given the extremely low output impedance of the detector, SQUIDs are the only devices capable of meeting these requirements. They have very low noise and high bandwidth in combination with reasonable dynamic range and slewrate, which have to be improved by feedback.

Although individual pixels are being readout by SQUIDS quite successfully, the readout of arrays by various multiplexing schemes is just beginning. Before the multiplexing schemes are addressed, the SQUID as a current amplifier will be discussed in more detail.

SQUID as current amplifier

A SQUID is a magnetic field sensor of unparalleled sensitivity. The output voltage of a SQUID is sine-shaped as a function of applied magnetic flux. Consequently, its behaviour is nonlinear and periodic. One period corresponds with the magnetic flux quantum Φ_0, where $\Phi_0 = 2.07 \times 10^{-15}$ Wb. With an input coil as current-to-flux tranducer, a very sensitive cryogenic current amplifier is obtained, especially suitable for low-impedance sources.

The proper use of SQUIDs as current amplifiers is complicated by two characteristics. The SQUID output noise voltage is small in comparison to the input noise levels of conventional room-temperature electronics, so care has to be taken for proper matching. Furthermore, owing to its periodic behaviour, linearity and dynamic range require special attention. A number

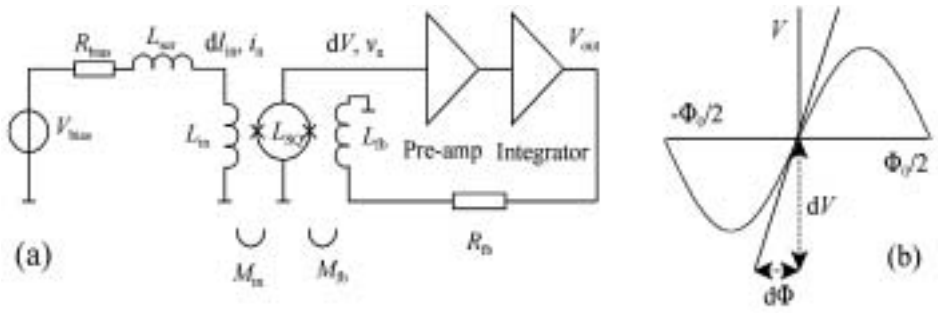

Figure 5.11. Electrical circuit equivalent of the SQUID system including the voltage-biased bolometer and an additional series inductance in the input loop (a). The parameters of the *V-F* curve are shown in (b).

of strategies are discussed in the following sections to optimise these characteristics.

The Flux Locked Loop

A common solution for improving linearisation and dynamic range is the Flux Locked Loop (FLL). The electronics circuit equivalent of a microcalorimeter read out by a SQUID with an FLL is shown in Fig. 5.11a.

Microcalorimeter R_{bias} is voltage-biased by voltage source V_{bias}. The current change is magnetically coupled into the SQUID loop with inductance L_{SQ} through the use of an input coil with impedance L_{in} , so that $d\Phi_{in} = M_{in}\, dI_{in}$ with $M_{in} = k(L_{in}\, L_{SQ})^{1/2}$ and $k \sim 1$, the coupling constant between the input coil and the SQUID loop. Subsequently, the magnetic flux change $d\Phi$ is transferred to a voltage change dV by $dV/d\Phi$, which is the slope of the flux-to-voltage (*V-F*) curve in the bias point of the current-biased SQUID (see Fig. 5.11b.

Subsequently, the output dV is pre-amplified to a measurable output voltage signal. In order to guarantee large dynamic range, linearity and stability, a feedback circuitry has to be added. This consists of a feedback coil L_{fb}, coupled to the SQUID loop with mutual inductance $M_{fb} = k(L_{fb}\, L_{SQ})^{1/2}$ and fed by the output signal through a feedback resistor R_{fb}. An integrator is added in the loop in order to create very large dynamic range and stability at low frequencies.

The bandwidth of the FLL system is set by the transmission delays in cabling and electronics. For practical systems, the bandwidth is limited to ~ 5-10 MHz by the cabling length between electronics and detector. This could be appreciably optimised by cold amplifiers or cryostats designed for very short cable length.

Matching of the SQUID output to the preamplifier

A standard DC-SQUID operated at < 4K has an input noise level in the

range of 0.1-1.0 $\mu\Phi_0/\sqrt{Hz}$. This is transferred to the required current noise by an input coil with the proper mutual inductance. The typical responsivity of a DC SQUID is 100 $\mu V/\Phi_0$, so the output voltage noise is typically 0.01-0.1 $nV/\sqrt{Hz}$, quite a bit lower than the typical 0.5 $nV/\sqrt{Hz}$ input voltage noise of room-temperature electronics. This will result in a loss of dynamic range, when the noise level is matched by the use of a bigger input coil to the SQUID. To compensate for the loss of dynamic range, the loop gain of the FLL has to be increased, which will decrease the system bandwidth. There are several routes to improve on this situation by matching the SQUID output to the amplifier input. A few methods are briefly discussed below.

A way to match the SQUID output noise level to that of semiconductor electronics is by putting n SQUIDs in series. When all SQUIDs operate in phase, the output voltage increases by a factor of n, while the SQUID noise increases with $\sqrt{n}$. In this way, better matching between the room-temperature electronics and the SQUIDs is obtained. SQUID current amplifiers based on this principle, generally called array SQUIDs, are being pioneered by NIST and are commercially available in the USA. In combination with an FLL, they meet the requirements for single-pixel readout.

Another means of noise-matching has been obtained by Additional Positive Feedback (APF). Local (positive) feedback at the SQUID (APF) has been applied to increase the transfer function ($\partial V/\partial F$) of the SQUID so that better noise-level matching with the room-temperature electronics is obtained. The disadvantage of this technique for XEUS is that the dynamic range of the system is decreased.

A different route for noise-matching is taken by VTT (Espoo, FIN) with Adaptive Noise Cancellation (ANC). In this case, voltage bias is used for the SQUID, which allows for feedback of and thereby cancellation of the pre-amplifier voltage noise. This approach has no impact on the system dynamic range, but a slight penalty on the system bandwidth and the requirement for fine-tuning of the feedback circuitry with a cold FET of very well-specified resistance. This system essentially meets the XEUS single-pixel requirements.

With AC-biasing of the TES microcalorimeter, impedance matching between the SQUID and the room temperature electronics can be taken care of by transformer coils. In that case, the dynamic range is limited by the noise temperature of the room-temperature amplifier.

Array readout schemes

Direct readout of an n x m-pixel microcalorimeter array requires one SQUID per pixel. Limited cooling power, cabling complexity and its potential unreliability are the main drivers for reduction of the number of SQUIDs and wires. In that context, several multiplexing concepts are being studied worldwide. Distinct alternatives are discussed in this section.

Direct readout

The readout of each pixel is based on a SQUID current amplifier operated as a null detector by means of FLL electronics as described above. Array SQUIDs or SQUIDs operated with ANC meet the XEUS requirements. The most conservative approach is to equip each pixel with a separate biasing and readout circuit, consisting of a shunt resistor, a SQUID and an FLL. Since the cooling capacity of the 35mK stage is limited, the n x m SQUIDs have to be mounted at the intermediate temperature level (0.8-1.0K) of the ADR. The limited available cooling power makes the design of the 3 x n x m wire looms between the SQUIDs and the microcalorimeter array challenging. The number of wires between the intermediate temperature level and the room-temperature electronics is at least 5 x n x m. The room-temperature electronics will also be complex because of the large number of required FLLs.

The number of wires and SQUIDs could be reduced by the cross-connection of a few pixels in a type of matrix readout. This will, however, degrade the energy resolution by $\sqrt{m}$ and the count rate ability by m, with m the number of interconnected pixels read out by one SQUID.

Multiplexing

The Nyquist criterium states that a signal with a bandwidth F_s and duration T_s can be exactly represented by a K-dimensional space, where $K = 2F_sT_s$. Therefore an amplifier with bandwidth MF_s spans an M x K-dimensional linear space during the time interval T_s. Consequently, if a proper orthogonal basis is chosen for each TES signal, an amplifier with negligible noise and bandwith MF_s is capable of transmitting M signals simultaneously without loss of SNR.

Multiplexing involves projecting the M, K-dimensional signal subspaces in the M x K-dimensional amplifier space in such a way that the signal subspaces are independent. Projection is accomplished by multiplying each signal subspace with an element of an M-dimensional orthogonal basis.

For Time Division Multiplexing (TDM), the orthogonal basis can be formed by boxcar functions, which are square-wave on/off functions with a duty cycle of $1/M$, shifted $1/2F_sM$ in time space with respect to each other. The multiplication can be implemented in several ways. At present, NIST uses SQUIDs at each detector pixel, which act as superconducting switches and are fed by the boxcar generator.

In the case of Frequency Division Multiplexing (FDM), the orthogonal basis may be formed by M sine functions at carrier frequencies $m\omega_c$, $m = 1, 2,\ldots M$ with $\omega_c > 2\pi F_s$. The multiplication with this carrier frequency is known as amplitude modulation (AM). Since the TES is a resistive element, amplitude modulation can be achieved by biasing the microcalorimeter itself with an AC bias voltage.

Time Division Multiplexing

NIST has initiated the development of TDM. It will be used for the SCUBA II sub-mm array on the James Clerk Maxwell Telescope and is also

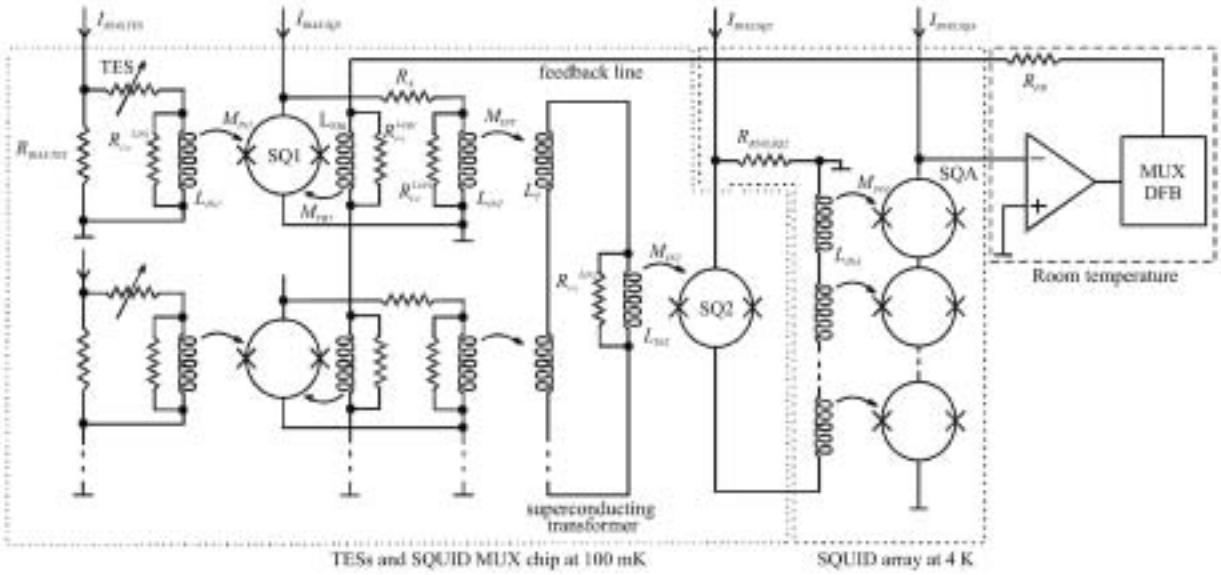

Figure 5.12. TDM circuit as developed at NIST. The pixels in one column are connected to a common summing loop readout by a second-stage SQUID, which is buffered by an array-SQUID. In the TES detector array, one row at a time is switched on by activation of the first-stage SQUIDs in that particular row. The dynamic range and linearity of the system is improved by a digital feedback system.

under development for the X-ray microcalorimeter experiment on Constellation-X. The layout of the second-generation TDM at NIST is shown in Fig. 5.12. In this system, each pixel is equipped with a SQUID, acting as a superconducting switch. All the SQUIDs of one column are subsequently coupled to a summing loop readout by a second-stage SQUID, which is subsequently coupled to an array SQUID to match the cold electronics to the room-temperature electronics. There is a digital FLL system for each multiplexer chain. During operation the readout is activated row by row. The inactive rows are essentially switched off and do not contribute significantly to the system noise.

The number of wires between the pixel-array and the SQUIDs is the same as for direct readout, i.e. 3 x n(row) x m(column). The number of connections between the SQUIDs and the warm electronics is reduced to $10m + 2n$ and the number of FLL circuits is reduced by a factor of 32.

The SQUID produces wideband white noise. In case of TDM, the SQUID produces noise over an MF_s bandwidth, while the TES signal rolls off at F_s. Consequently, the sampled TES signal contains aliased high-frequency noise of the SQUID amplifier. To make this negligible, the SQUID noise has to be decreased by $\sqrt{M}$, thereby reducing the useful dynamic range. In the literature, this effect is known as the multiplex disadvantage. The requirements for the XEUS array are given at the beginning of Section 5.3.

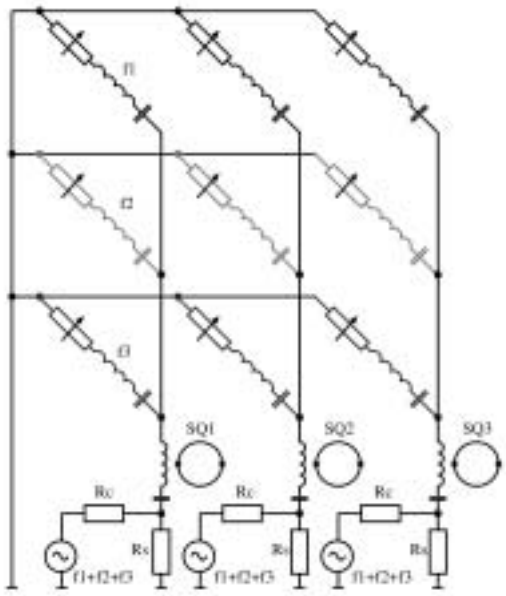

Figure 5.13. Frequency multiplexing schematic. Each row is biased with a different frequency (indicated by different colours) and each column is read out with a single SQUID. Each pixel (the microcalorimeters are indicated as variable resistors) is equipped with an LC-filter to prevent addition of TES Johnson noise.

For TDM, the requirement for the noise has to be enhanced to $< 18/\beta\sqrt{M}$ pA/√Hz, for the dynamic range to 1.2 x 10^6 $\beta\sqrt{M}$ √Hz and for the bandwidth to M x 100 kHz with $\beta \sim 3$ and $M = 32$. For realistic values of the achievable multiplexer input noise, i.e. 0.2 $\mu\Phi_0/\sqrt{\text{Hz}}$, and an FLL gain-bandwidth product limited by a 25 cm cable between cold and warm electronics, i.e. 50 MHz, the TDM multiplexer is able to read only $M \sim 5$ rows.

So, for XEUS, about 6-7 multiplexers are required to read out one detector column. This limit is set in particular by the combination of the slewrate and dynamic range requirements. Relaxation of the event time requirements by about a factor 6-7 (Constellation-X aims for τ = 500 μs), allows the readout of one detector column with one multiplexer.

Frequency Division Multiplexing

FDM is under development at Univ. California at Berkeley (USA) and Lawrence Livermore National Laboratory (LLNL, USA), and at VTT (FIN) and SRON (NL). A sketch of a possible layout for 3 x 3 pixels is given in Fig. 5.13. Each row of bolometers is biased with an alternating current at a different frequency. A single SQUID is connected to each column to detect the combined signal of all rows in that column. The essential point is that the signals are separated in frequency space, so that there is no influence on count rate capability and energy resolution. Each pixel requires an LC-filter

to prevent addition of the white Johnson noise from the TESs, thereby degrading the energy resolution.

The use of an FDM multiplexer reduces the number of SQUIDs to m and the number of wires to room temperature to $5m$. Also, the number of wires between the pixel-array and the SQUIDs has become quite small, i.e. $2m$. More complicated, though, is the fact that each pixel is equipped with a filter. These filters set the AC-bias frequency. For example, operation at 10 MHz requires capacitors with a size of approximately 1 mm^2. So the filters are most probably produced at a wafer separate from the TES sensor array, which requires $\propto m^2$ connections either by wire- or bump-bonding.

First of all, it has to be proved that the TES can be successfully operated at AC-bias instead of DC-bias. Recent work at LLNL and SRON has shown that a TES device preserves its I-V characteristics and energy resolution under AC-bias. At SRON, a resolution of 6.3 eV FWHM for 5.9 keV X-rays has been obtained under AC-bias at 46 kHz, while the DC resolution measured for the same device was 5.5 eV. At this stage of development, the discrepancy can be accounted for by unsufficient optimisation of the AC versus the DC readout electronics.

AC modulation enables impedance matching between the SQUID and room-temperature electronics. By careful design of a very low-noise SQUID and room-temperature amplifier, it may be possible to operate a SQUID without FLL so that operation at frequencies above the FLL cut-off bandwidth limitation is possible. The dynamic range requirement remains, however, challenging and the SQUID response has to be linearised in order to prevent mixing of different AC carriers.

Unlike TDM, frequency multiplexing does not suffer from the multiplex disadvantage. However, there is another cause for an increased requirement on dynamic range compared to that required for single-pixel readout. This is due to the fact that the output signals of all TESs in one column add. The first step to reduce this is effectively to get rid of the AC carrier signals by means of bias-current compensation. Now only the coincident X-ray signals in one column add. To FDM's advantage, an X-ray image of the sky will be quite empty apart from a few sources. Furthermore, we do not accept more that about 500 c s^{-1} (5% overlap) in one pixel anyway in order to retain good energy resolution. So signal pile-up within one column will in general be quite small. With the same SQUID and FLL performance as for TDM, frequency multiplexing can read out $M = 64$ pixels.

So FDM promises better performance than TDM for XEUS. This is because an X-ray image is largely empty and TDM uses a large fraction of its bandwidth to read out empty pixels. However, TDM is much further developed and highly promising results are being obtained from the sub-mm detector arrays for SCUBA II.

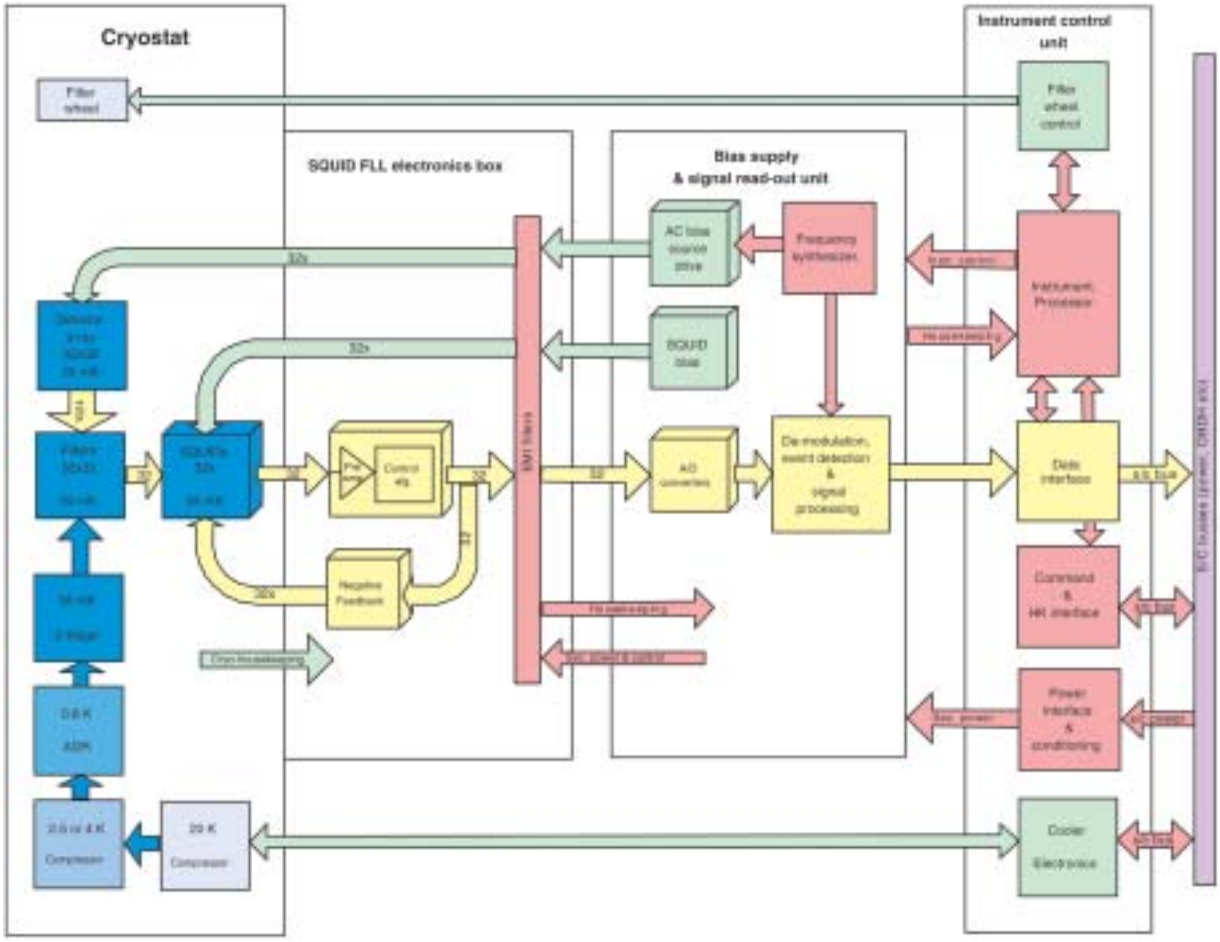

Figure 5.14. The NFI2 system design. The camera head consists of a cryostat with its coolers, housing the microcalorimeter array and SQUID electronics. The radiation entrance contains a filter wheel, which also seals off the cryostat. The electronics units outside the cryostat control all parts of the instrument and contain analogue and digital chains for data acquisition.

5.4 System description

Given the early stage of the programme, most of the instrument system aspects are under preliminary definition. A functional block diagram of a preliminary system design, based on FDM, is shown in Fig. 5.14. The instrument consists of a cryogenic part, the focal plane camera head and room-temperature electronics. The room-temperature electronics consist of three units: the SQUID FFL electronics box, the bias supply & signal read-out unit, and the Instrument Control Unit.

The NFI2 focal plane camera head

The focal plane camera head consists of a cryostat with the various cooling stages required to cool it down to 35mK. The cryostat houses the micro-calorimeter array and the SQUID-based superconducting electronics and is

equipped with a filter wheel at the radiation entrance from the X-ray telescope. The filter wheel has one position to seal off the cryostat hermetically in order to circumvent contamination of the microcalorimeter array during ground testing, launch and ISS docking.

The NFI2 filter wheel assembly

The NFI2 filter wheel assembly has the same functionality as that for the NFI1 instrument. As for NFI1, the filter wheel assembly also serves as a sealable entrance door.

Operation of the detector requires a very significant suppression of the sky and spacecraft background, both in the infrared as well as in the optical. Obviously, the filters have to be maximised in terms of X-ray transmission and IR and optical absorption. Given the optimisation for another energy range, the required filters for NFI2 partly differ from those for NFI1. Section 7 provides more details on the filters.

Microcalorimeter array and SQUIDs

The microcalorimeter array has an operational temperature of 80mK and will be mounted on the lowest temperature stage of the double-stage ADR, which has a base temperature of 35mK. The temperature of that stage has to be stable to < 10mK h^{-1} and the stray magnetic field of the cooler at the location of the sensor array has to be smaller than 10^{-6} T.

In the frequency multiplexing concept, the TESs are AC-biased and via serial L-C bandpass filters coupled to 32 column SQUID amplifiers (see Section 5.3). With a cooling power of the second ADR cooling stage of 5.5 μWh @ 35mK, it becomes feasible to place the 32 SQUIDs at the lowest temperature, thereby reducing their noise level and increasing the system dynamic range. To ensure stable SQUID operation, the stray magnetic field should be < 10^{-5} T.

NFI2 cooling

Operation of the NFI2 spectrometer requires a bath temperature of 35mK. Such a temperature can be obtained by a double Adiabatic Demagnetisation Refrigerator (dADR), which runs from a base temperature of 2.5K created by a Joule-Thomson cooler on top of a two-stage Stirling cooler. See Section 6 for details of the cooling system.

The multipixel array and the SQUID amplifiers will be situated at the 35mK stage. The wiring requires adequate thermal anchoring at all temperature stages in order to reduce the thermal load. The estimated thermal loads on the system are based on the rather optimised FDM approach and are summarised in the table on p.91, together with the other requirements on the cooler.

Room-temperature electronics

The room-temperature electronics consists of three units:

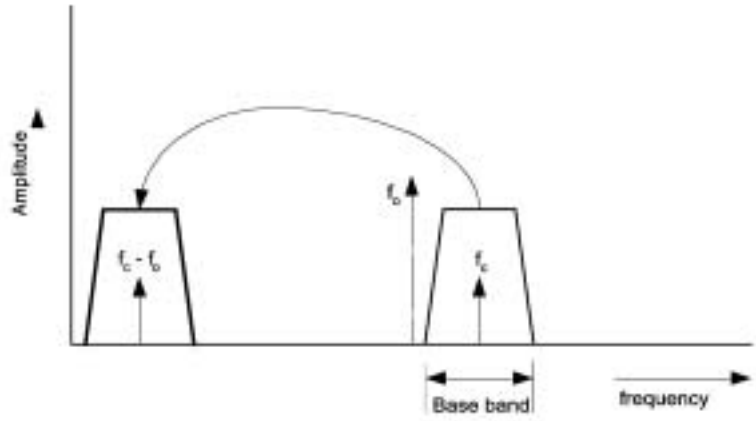

Figure 5.15. Baseband conversion. The baseband of 32 amplitude-modulated frequencies is converted to lower frequencies.

— the SQUID FLL electronics and I/F filter box (SQUID FLL Electronics Box; SEB);
— the bias supply and signal readout unit (Bias Supply & Signal Readout; BSSR);
— the Instrument Control Unit (ICU).

The first box (SEB) contains very sensitive analogue electronics, to amplify the SQUID output signals and to ensure, by negative feedback (FLL), that the SQUIDs remain in their linear V-Φ working point. It contains also all interface circuits (EMI filters) for the signals to and from the micro-calorimeter array and SQUIDs.

The second unit (BSSR) contains sensitive and stable AC bias supplies for the microcalorimeters, the bias supplies for the SQUIDs and the readout chain, inclusive analogue-digital conversion and the first stage of signal processing of the detector signals.

The ICU takes care of instrument control and all the interfaces to the spacecraft. The control functions comprise those for the filter wheel and cryocooler, the setting, adjustment and (re-)calibration of the detector and readout SQUIDs, and data acquisition and final data processing of science and housekeeping signals. Some of these building blocks are discussed in more detail below.

SQUID electronics

The baseline is to operate the SQUIDs in Flux Locked Loop. The maximum frequency response of the control loop will be determined by the transmission delay of the signals in the cables and the electronics (maximum 5-10 MHz). The minimum AC bias frequency will be dictated by the practical

implementation of the bandpass filters between the microcalorimeters and the SQUIDs (maximum practical capacitor values). A trade-off between those two constraints is still to be made. To solve the problem of loop stability at higher frequencies, three possible solutions are envisaged:

— direct feedback with warm SQUID FLL electronics (maximum AC bias frequency ~ 5 MHz);
— direct feedback with cold SQUID FLL electronics inside the cryostat;
— baseband conversion with warm electronics.

Baseband conversion implies that the overall SQUID FLL response can be limited to a lower frequency (< 5 MHz). The frequency baseband of 32 amplitude-modulated detector signals ($f_c \pm \Delta f$) is mixed with an oscillator signal (f_0) to transfer the band to lower frequencies ($f_c \pm \Delta f - f_0$); see Fig. 5.15. This signal is subsequently fed back and at the level of the SQUID the signal is again restored to the original frequency band.

Bias supply and signal readout

The bias supplies for the microcalorimeter array should generate 32 very low-noise and stable AC signals. The frequency of one bias signal must be accurately tuned to the best-fit of 32 narrow-bandpass filters for one row of the detector array. To produce these accurate tuneable signals, a frequency synthesiser is envisaged.

The signals of the 32 SQUID FLL outputs must be demodulated before further signal processing is possible. Demodulation might be performed by analogue or digital electronics. With analogue circuits, 32 x 32 identical demodulation chains are required. This solution is only practical, with respect to volume, mass, power consumption and reliability, with a high degree of electronic integration in an analogue or mixed-signal ASIC. The digital solution is therefore more attractive, but requires the signal to be digitised with a high sample rate at 10-20 times the carrier frequency (AC bias frequency).

After demodulation, event detection and further signal processing should be performed digitally. For this task, a trade-off between two solutions must be made: ‘general purpose’ Digital Signal Processors (DSPs) or a dedicated design integrated in an ASIC or FPGA.

Data acquisition

Data acquisition takes place in the ICU. The degree of further data processing will depend on the mode of operation. Obviously it should be possible to send all information on the digitised pulse shapes to the ground as well as digitised data on the instrument noise level. An event will consist typically of a hundred 12-bit samples, so this mode is feasible only at very low count rates.

The baseline mode will apply the appropriate digital filtering to the digitised signal data onboard and thereby derive a pulse height for every signal. This,

together with the location in the microcalorimeter and a timestamp, will be sent to the ground. More complex modes, where correction for pile-up and cross-talk will be carried out onboard, have not been assessed in this phase of the programme.

Resources

The load on the cooling system is based on a system with 32 SQUIDs and the necessary wiring. At the camera level, it is based on thermal isolation by superconducting Al wiring on top of a 1 cm-long, 6 mm-wide and 2 μm-thick Si_xN_y membrane, although Kapton foils might be used here as well. For the rest of the connections, 50 μm manganine wiring is taken with 10 wires/channel, thereby allowing for adequate shielding. The calculated heat loads at the various stages and the power dissipated by the microcalorimeter and the SQUIDs are indicated below:

Item	*Temperature Stage*	*Thermal load, T-stability, B-field*
Temperature stability	35mK	< 10mK h^{-1}
Stray magnetic field	35mK	< 10^{-6} T
Load wiring 35-800mK	35mK	5 nW
Power in pixels	35mK	20 nW
Power in shunt resistors	35mK	200 nW
SQUID power	35mK	32 nW
Wiring 0.8-2.5K	0.8K	0.5 μW
Wiring 2.5-20K	2.5K	16 μW
Wiring 20-150K	20K	1.3 mW
Wiring 150-300K	80K	4 mW

With a cooling power of 5.5 μWh @ 35mK for the double-ADR, this allows for uninterrupted measurement times of 20 h. AC bias in principle allows for removal of the shunt resistors, since the voltage bias can be created by the use of transformers. This would increase the measurement time to about 100 h. In case cold FLL electronics are required, the load on the 150K stage (Si-components) or 20K stage (GaAs-components) will be enhanced very significantly. Quantitative values are not available at this stage.

The mass and power budget estimates relevant for the spacecraft are:

Item	*Mass (kg)*	*Power (W)*
Cooler	80	220
Detector/filter wheel	15	
Flux Lock Loop electronics	6	20
Bias Supply & Signal Readout	8	40
Instrument Control Unit	7	30
Total	116	310

The resources required for the cooler are based on information on existing instrumentation, described in more detail in Section 6. The mass estimation for the detector housing and filter wheel is derived from a crude design of

detector housing and cryostat. The electronics estimate is based on 32 SQUIDs with FLL electronics and 32 fast, 50 MSa s^{-1}, ADC and 64 ASICs to digitise and process a total data rate of 10^4 event s^{-1}.

5.5 Performance

The performance parameters for NFI2 instrument are:

Spatial resolution element size	240 x 240 μm / 1 x 1 arcsec
Array size	32 x 32 / 0.5 x 0.5 arcmin
Energy range	0.5-15 keV
FWHM energy resolution	2.3 eV @ 1 keV and 3.3 eV @ 7 keV
Detection efficiency	> 90% up to 7 keV (Fig. 5.9)
Fall time	120 μs @ 1 keV and 245 μs @ 7 keV
Maximum count rate	500 c s^{-1} pix^{-1}

The energy resolution slowly degrades towards higher energies because, during the event, the detector is driven away from its optimum bias point. This influences the event time and thereby the energy resolution. To a first order approximation, the energy resolution in the NFI2 energy range is given by:

$$\Delta E_{FWHM}(E) = 2.1\sqrt{\frac{E(\mathrm{keV})}{4.8} + 1} \quad \mathrm{eV} \tag{5.14}$$

The calculated efficiency is given for the absorber with 0.21 μm Au and 7 μm Bi in Fig. 5.9.

The characteristic decay time of the events is given by:

$$\tau_{eff}(E) = 100\left[\frac{E\,(\mathrm{keV})}{4.8}\right] \quad \mu\mathrm{s} \tag{5.15}$$

No real data are available on the rejection efficiency of background events. Risetime rejection will not be very efficient. Minimum ionising particles crossing the absorber will deposit about 16 keV, so the majority of those events will fall outside the main NFI2 energy range. Furthermore, some events might be rejected by the use of anti-coincidence between pixels. In case this level is considered too high, an anti-coincidence shield has to be considered.

6 The Focal Plane Assembly Cooling

The XEUS payload includes three X-ray imaging spectrometers, WFI, NFI1 and NFI2, with respective operating temperatures of 180-210K, 300mK and 20-35mK. The higher operating temperature falls within the range of passive radiators or Peltier coolers and was discussed specifically for WFI in Section 3.9. The sub-Kelvin temperatures require a multi-stage system with the following architecture:

— 2.5K heat sink + ^{3}He Sorption Cooler (HSC);
— 2.5K or 4K heat sink + Adiabatic Demagnetisation Refrigerator (ADR).

Other available sub-Kelvin cooling techniques fail to meet the specifications and have been excluded. The 2.5K or 4K heat sink can be provided either by a pumped helium bath or by a Stirling or pulse tube mechanical cooler associated with a Joule-Thomson loop. Most of the technology associated with the proposed cooling solutions has been or is about to be demonstrated in the laboratory, if not in space. Many of the system aspects have been proved in studies for various instruments. There is therefore good confidence that these technologies can be developed in time for use on these instruments.

6.1 Closed cycle coolers versus cryogens

The sub-Kelvin temperature calls for a multistage system. The 300-4K (or 2.5K) range can be provided only by a (pumped) helium cryostat or a mechanical cooler. The former does not need any input power for its operation and is fully static, but has a limited lifetime. The latter requires only input power and can be operated indefinitely. In addition, the envelope and mass of a mechanical cooler are smaller than those of a cryostat offering a lifetime of a few years.

XEUS will operate continuously between visits to the ISS, which will occur on a timescale of about 5 years. Therefore, the cooling must be provided along the same timescale. As a result of this and the low Earth orbit, it appears highly unlikely that a helium cryostat could satisfy the mission lifetime between ISS visits. Furthermore, it would require specific and costly equipment (on-orbit transfer, liquid helium container, …) at the ISS. However, mechanical cooler technology is at a sufficiently advanced stage, so it has been chosen as the mission baseline. Problems associated with induced vibrations are recognised as a critical design aspect. They must be evaluated and, if necessary, solved using, for example, low-vibration drive electronics and improved support structure.

6.2 Mechanical cooler design

Description

The reliability requirement associated with the development of cryocoolers for space applications leads to the rule that a cooler shall be simple, have no

Figure 6.1. The 50-80K Stirling cooler. (Astrium UK)

friction or, even better, no moving parts. ESA has been actively supporting a development effort that began in the UK in the early 1980s (Oxford Univ.; Rutherford Appleton Laboratory, RAL;, British Aerospace, now Astrium UK) on a 50-80K split single-stage Stirling cooler. The key feature of this cooler is the use of gas clearance seals to eliminate all rubbing parts and of diaphragm springs to maintain these clearance seals. This 50-80K cooler is now available as an industrial off-the-shelf production item from Astrium UK (Fig. 6.1).

The capability of the Stirling cooler has been extended to lower temperature: a space-qualified double-stage Stirling cooler using the same proven technology, providing about 250 mW at 20K is available.

Furthermore, this dual-stage Stirling cooler has been used as a precooler for a 4K Joule-Thomson stage. This 4K cooler was originally the baseline configuration for the Herschel satellite; its qualification against the Herschel requirements is expected to be achieved in the near future. Finally, RAL, which originated most of the above development, has been operating the 4K system using ^{3}He instead of ^{4}He. In this case, this cryocooler provides 5 mW of cooling power at 2.5K (instead of 10 mW @ 4.2K). Fig. 6.2 shows a laboratory scale demonstration of this 4K cooler.

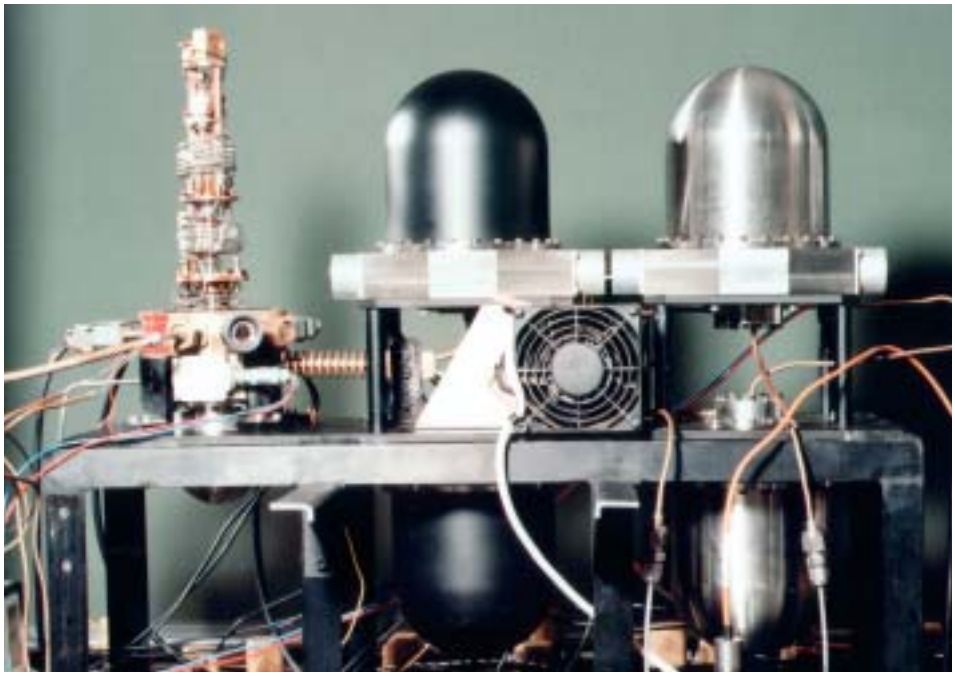

Figure 6.2. Laboratory scale demonstration of the 4K cooler.

This cooler is the baseline for the 2.5K or 4K cold heat sink required by the NFI instrument on XEUS. Development of pulse tube cryocoolers is underway in Europe; if successful, the two-stage Stirling cold finger could be replaced by a two-stage pulse tube, providing benefits such as ease of integration, robustness and lower level of induced vibrations.

XEUS design

A proposal to NASA for the Hubble Space Telescope (HST) 2002 refurbishment mission baselined a set of Stirling cycle coolers coupled to a ^{3}He sorption cooler to provide a closed-cycle cooling capability with a base temperature of 350mK. A feasibility study on this three-stage cooler was performed and a prototype is being tested. This study, funded by ESA, was carried out by a coordinated team led by MMS-Bristol and supported by RAL and the Service des Basses Températures of CEA-Grenoble (SBT). Although this system was specifically studied for HST, it provides a guideline for the XEUS mission because the bulk of the system engineering work has been done. The system consists of three main stages:

— a Stirling cycle pre-cooler to enable temperatures down to 20K to be reached. This cooler also provides intermediate cooling at about 150K (500 mW);
— a Joule-Thomson (J-T) closed-cycle cooler using ^{3}He as the working fluid to reach temperatures down to 2.5K;
— a ^{3}He sorption cooler to reach 0.3K.

The first two stages require the use of two compressor pairs: the first is used for the 20K Stirling cold finger, and the second provides the DC gas flow for the J-T loop. The specific architecture used to couple the sorption cooler thermally to the 2.5K stage, as well as a description of this sorption cooler, is detailed in the following section

The 2.5K cooler (Stirling + J-T) uses and thus dissipates nearly 220 W. This number includes the electrical consumption. The rough power budget (detector electronics are not included) is:

Function or Unit	*Power (W)*
20K Cooler compressor pair	82
Displacer/compensator	3
Drive electronics	38
2.5K Cooler compressor pair	60
Drive electronics + Getter heater	35
Total	218

The predicted mass budget (2.5K cooler + electronics) is expected to be ~ 65 kg. The various contributions (rough estimate) are:

Item	*Predicted flight mass (kg)*
20K compressor pair	14.5
20K displacer/compensator	5.5
20K various	3
2.5K compressor pair	14.5
2.5K various	10
Various shields	1.5
20K Drive electronics	7.5
2.5K Drive electronics	7.5
Total	64

The instrument support structure is not included in these figures and would increase the overall mass.

6.3 NFI1 low-temperature stage

The sensor technologies used for this instrument require an operating temperature of around 350mK, which will be provided by an HSC. Adsorption coolers rely on the capability of porous materials to adsorb or release a gas when cyclically cooled or heated. By varying the temperature, it is possible, for instance, to provide a pumping effect, which can be used to manage the gas pressure in a closed system, condense liquid at some appropriate location and then perform an evaporative pumping on the liquid bath to reduce its temperature.

CEA-SBT has developed or contributed to the design of several adsorption ^{3}He coolers with specific design for weightless operation. These coolers

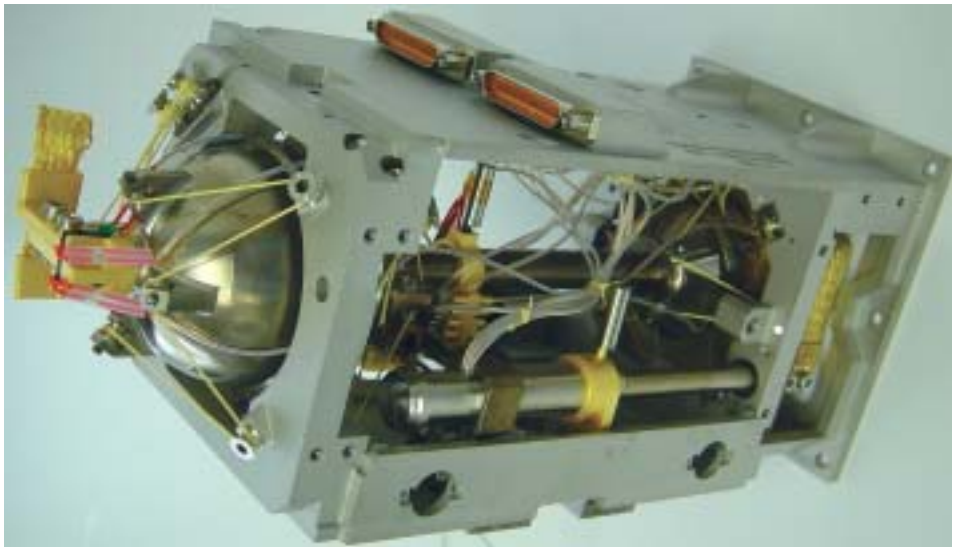

Figure 6.3. Herschel sorption cooler to be used on the SPIRE and PACS instruments.

require a pre-cooling stage at a temperature lower than the helium liquid-vapour transition (≤ 3K); they achieve sub-Kelvin temperature with autonomies ranging from 1 day to 2 weeks for typical net cooling power ranging from 10 μW to few hundred μW. Helium sorption refrigerators have no moving parts, are vibrationless and can be designed to be self-contained and compact with a high duty-cycle efficiency. These features and the expected reliability that follows make them very attractive for space applications. In addition, the thermal and mechanical interfaces are fairly simple. The links to ambient temperature are limited to the heater wires used to drive the sorption pump and, possibly, the heat switches.

Figure 6.3 shows a cryogenic qualification model of the cooler to be flown aboard the Herschel satellite. In this design, the evaporator is filled with a porous material to hold the liquid by capillary attraction in the absence of gravity effects. Operation of the refrigerator begins by cooling all components to below 3K (pre-cooling stage), at which temperature all of the ^{3}He is adsorbed by the activated charcoal in the sorption pump.

Once the heat switch on the evaporator has been turned on and the heat switch on the pump has been turned off, the refrigeration cycle is initiated by heating the sorption pump to ~ 40K with a resistive heater. The heat switches allow establishment of the necessary temperature gradient to make the evaporator the coldest point in the system. As the temperature of the sorption pump rises, ^{3}He gas is desorbed from the charcoal. When the ^{3}He gas pressure exceeds the saturated vapour pressure of ^{3}He at the pre-cooling stage temperature, liquid condenses in the evaporator because both the surface tension and the vapour pressure provide forces that drive and hold the liquid to the coldest point.

Finally, the heat switch on the pump is turned on, thermally grounding the sorption pump, and the heat switch on the evaporator is turned off, thermally isolating the evaporator. The heat switch on the pump, although not necessary, provides a significant improvement in terms of dissipated power and cool-down time. As the sorption pump cools down, the vapour pressure of ^{3}He is reduced and the temperature of the evaporator drops quickly to ~ 300mK, where it remains stable until the liquid ^{3}He is exhausted. The refrigerator can be recycled indefinitely.

The cooling of the NFI1 sensors will be effected by a smaller unit. As mentioned above, the 2.5K heat sink will be provided by a Stirling cooler associated with a ^{3}He Joule-Thomson loop. Owing to mechanical and thermal constraints for XEUS, the HSC is limited to a 2-litre STP, which corresponds to the characteristics of the prototype being evaluated in the framework of the HST study.

The architecture is as follows. The second pair of compressors required to provide the DC gas flow drives three Joule-Thomson loops (J-T1, J-T2, J-T3), and a bypass line. J-T1 and J-T2 alternatively provide cooling to the sorption pump or to the evaporator. J-T3 continuously operates to maintain the thermal shield at 2.5K, and can be additionally used to thermally stabilise the wires. The bypass line is used during the pre-cooling phases and could also be thermally coupled to the sorption pump to improve the performance during the cool-down phase. J-T1, J-T2, J-T3 and the bypass line are turned on and off by room-temperature valves controlled by the drive electronics.

With this architecture, no heat switches are required because this function is provided by the J-Ts.

Although no precise specifications have been set for NFI1, the cooler could provide the following performance:

Pre-cooling stage	2.5K J-T loop
Available cooling power at 2.5K	3 mW
Sorption cooler characteristics	
^{3}He charge	2 litres STP
Estimated mass	< 100 g (support structure excluded)
Rough overall dimensions	Ø 60 mm x h 130 mm
Typical performance	
Cooling power	20 μW at 354mK
Hold time (with 20 μW applied)	14.5 h
Recycling time*	13 h*
Ultimate temperature (with no applied load)	315mK

*this number depends on the thermal architecture used. In this case, it is assumed that at any given time the load on the 2.5K stage cannot exceed 3 mW.

The HSC mass and input power (few 0.1 mW) are negligible in comparison with the overall mass and power needed for the 2.5K system. The drive electronics, not included here, are expected to weigh around 1 kg.

6.4 NFI2 low-temperature stage

This instrument requires substantially lower temperatures, down to 20-35mK, which will be provided by an ADR coupled to a 2.5K mechanical cooler. The cooling may be regarded as an entropy-reducing process. For instance, for a paramagnetic material and its associated disordered collection of magnetic dipoles, the application of a magnetic field causes the alignment of the dipoles and consequently a reduction in entropy. This technique has been extensively used in laboratories throughout the world. It provides cooling in the whole cryogenic range down to a few mK. With the advent of superconducting magnets, ADRs have become simpler and cheaper. As with the HSC, the ADR has no moving parts, is vibrationless, self-contained and requires only current leads for its operation. These features and the expected reliability that follows make them very attractive for space applications. An ADR is schematically composed of three items:

— a paramagnetic material integrated within some enclosure and with an insert. This is suspended via low thermal conductivity materials to the precooling stage;
— a heat switch required to couple or decouple the paramagnetic material thermally to the pre-cooling stage;
— a magnet (usually superconducting).

The basic operating cycle of an ADR is divided into three steps. The first is isothermal magnetisation of the paramagnetic material for pre-cooling. As the magnetic field is applied, the ion magnetic moments that are free with randomly oriented spins are aligned, thus lowering the entropy of the material. This process generates heat, known as the magnetisation energy, which is extracted via the heat switch to the pre-cooling stage. The second step is adiabatic demagnetisation in which the magnetic field is reduced to the value corresponding to the desired final temperature. During this phase, the heat switch is off. Consequently, as a first approximation, the entropy of the system remains constant and so the temperature drops. The last step is usually isothermal demagnetisation. Once the required temperature is achieved, the magnetic field is then reduced at the appropriate rate to counteract the thermal input from the environment and maintain this temperature. Once the magnetic field reaches zero, the whole process can be indefinitely repeated, thus ensuring long hold-times (of order 24 h), interrupted by shorter recycling periods (of order 2 h).

Recognising the relevance of this technique to space applications, ESA recently placed a contract with Astrium (D) and the Mullard Space Science Laboratory (MSSL, UK) for the development and pre-qualification of an ADR, designed according to the XEUS mission requirements. Such work will lead to two engineering modules, and will allow experimental tests on

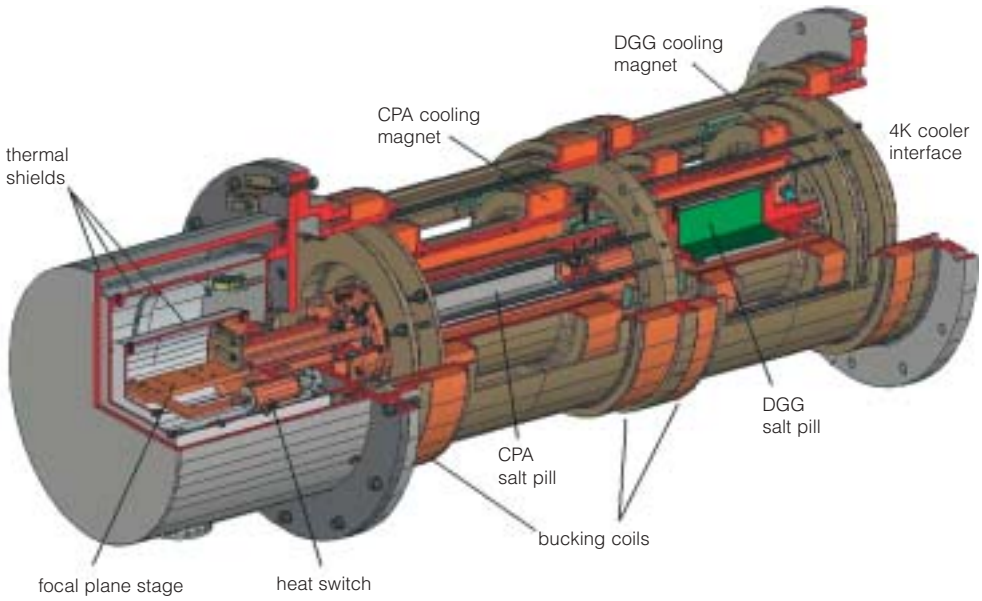

Figure 6.4. A double-stage ADR, employing salt pills of chromic potassium alum (CPA) and dysprosium gallium garnet (DGG).

representative focal plane detectors. This work builds on the experience at MSSL and is focusing on a double-ADR (dADR) system (Fig. 6.4). The key feature of the dADR is to permit cooling from 4K down to 100-10mK with limited magnetic field while offering a reasonable hold time. This is achieved via selected paramagnetic materials: dysprosium gallium garnet (DGG) for the 4K-1K stage and chromic potassium alum (CPA) for the lower stage (1K - < 0.1K). With this architecture, the required magnetic field remains of the order of 2-3 T, and possibly below. This limited field yields a number of advantages in comparison with conventional two-stage ADRs, including reduced stored energy, compatibility with passive shielding, and gains on the thermal loss owing to current leads. A laboratory-grade dADR is being assembled for testing during 2003. The two pre-qualification units, specifically designed for the XEUS mission, will become available by end-2003. The pre-qualification activities will simplify the future procurement of a fully flight-qualified version.

This dADR might provide cooling to NFI2's detectors. A 3-D model of this refrigerator is shown in Fig. 6.4.

The dADR comprises two ADRs, one housing the CPA material (material 2) and the other housing a DGG crystal (material 1). Solenoid-driven mechanical switches thermally couple or decouple one material to/from the other and/or the DGG crystal to the 4K interface. This system comprises two conduction-cooled NbTi magnets wound on the same copper former. Buckling

coils are associated with each main magnet to null the magnetic field at the heat switch positions and at the detector stage.

In principle, this system could also be coupled to a 2.5K mechanical cooler using a similar thermal architecture. The dADR characteristics are:

Precooling stage	2.5K J-T loop
Available cooling power at 2.5K	3 mW
dADR characteristics	
First-stage material	dysprosium gallium garnet
Second-stage material	chromic potassium alum
Typical magnetic field required	2-3 T
Estimated mass	29 kg (inc. magnetic stray field control)
Rough overall dimensions	Ø 282 mm x h 694 mm
Expected performance	
Cooling power at first-stage	~ 13 μW at ~ 1K
Cooling power at second-stage	1 μW at 20mK
Hold time	15 h for1 μW at 30mK
	19 h for1 μW at 50mK

The mass of the dADR is fairly high and a careful mechanical and thermal design of the support structure will be performed. The drive electronics (not included here) are expected to weigh ~ 7 kg.

6.5 System design and resources for NFI1

NFI1 and NFI2 both use a 2.5K mechanical cooler for the pre-cooling stage. The overall mass for these two instruments is expected to be ~ 150 kg, with overall power consumption of ~ 450 W.

Below is a summary of the foreseen instrument thermal budgets. Some data are missing because they require more advanced definition of the cooling system and architecture for their evaluation.

Type	*Maximum demand*	*Available resource*	*Margin*
Mass budget	65	TBD	TBD
Power budget	220	TBD	TBD
Heat flow budget: 350mK	20 μW	flexible	–
Heat flow budget: 2.5K	3 mW	5 mW	2 mW
Heat flow budget: 20K	TBD	250 mW	TBD
Heat flow budget: 150K	TBD	500 mW	TBD

6.6 System design and resources for NFI2

The same comments for NFI1 also apply here. The foreseen overall focal plane assembly thermal budget is:

Type	*Maximum demand*	*Available resource*	*Margin*
Mass budget	77	TBD	TBD
Power budget	220	TBD	TBD
Heat flow budget: 20-35mK	200 to 300 nW	flexible	–
Heat flow budget: 0.75-1K	~ 13 μW	flexible	–
Heat flow budget: 2.5K	TBD	5 mW	TBD
Heat flow budget: 20K	TBD	250 mW	TBD
Heat flow budget: 150K	TBD	500 mW	TBD

7 Filters for XEUS

7.1 Introduction

XEUS has a unique configuration – the mirror system is separated from the focal plane detector system without any closed structure or optical bench. Previous missions have all incorporated a closed tube as the structure linking the mirror with the detectors. Such a tube also removes stray light. Careful design is therefore required in the XEUS mission for the mirror spacecraft and detector spacecraft to ensure that stray light is not a problem. The stray light is, of course, significantly reduced by operating XEUS in its basic mode on the night side of the orbit – effectively using the Earth as a giant sunshield. One option to maximise observing efficiency is operation during the sunlit part of the orbit. The XEUS focal plane detectors may therefore require optical filters to:

— remove any residual stray light entering the focal plane during the sunlit part of the orbit;
— reduce the optical and UV radiation from stars in the XEUS mirror field of view (the cryogenic detectors described in Sections 4 & 5 are particularly sensitive to optical and UV radiation).

While the actual optical loads expected at the focal plane will need to be carefully evaluated through a full stray and imaged light analysis, during the spacecraft system study, some preliminary characteristics of possible filters can be presented. Clearly, any such filters constructed from free-standing thin films will reduce the soft X-ray response. From the XEUS core science objectives described in Section 1, it is clear that this reduction must be minimised.

In addition to optical and UV radiation, the cryogenic detectors are extremely sensitive to near-infrared radiation (NIR). This essentially blackbody radiation has the effect of degrading the energy resolution and decreasing the signal-to-noise ratio, thereby limiting the low-energy response and possibly introducing dead time into the detector system. Again, careful design of the cryostat will be necessary to remove this NIR load. Detector view angles to 293K surfaces, which radiate at ~ 10 μm, must be avoided. It is, however, considered necessary that some types of filters may be required to ensure NIR loads are reduced to acceptable levels.

7.2 Optical filters

Three filters are described here: Al/Si multilayers, Nb and Ca/Bo multilayers. These free-standing filters, typically 100-200 nm thick, are all based on an established polyimide grid technology. All provide a good soft X-ray response (typically > 10% transmission for X-ray photons of energy $E > 50$ eV) while attenuating NIR, visible and UV radiation to 10^{-4}-10^{-7}. Fig. 7.1 shows the soft X-ray response of these three potential filters, while Fig. 7.2 shows the transmission at optical wavelengths. From these figures, there is clearly considerable trade-off between the soft X-ray response and the required UV and optical attenuation (c.f. Nb filter).

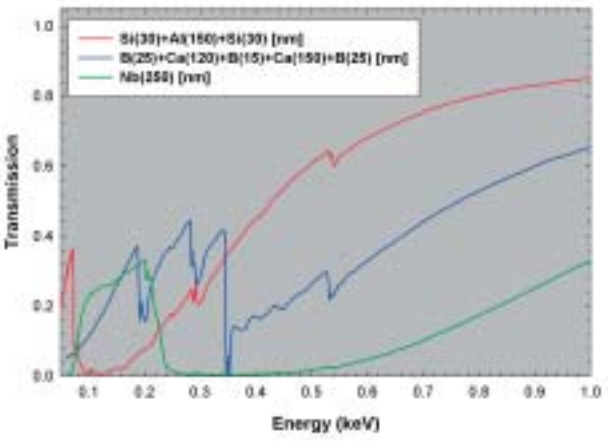

Figure 7.1 (above left). The measured soft X-ray transmission above 50 eV for the three filters described in Section 7.2.

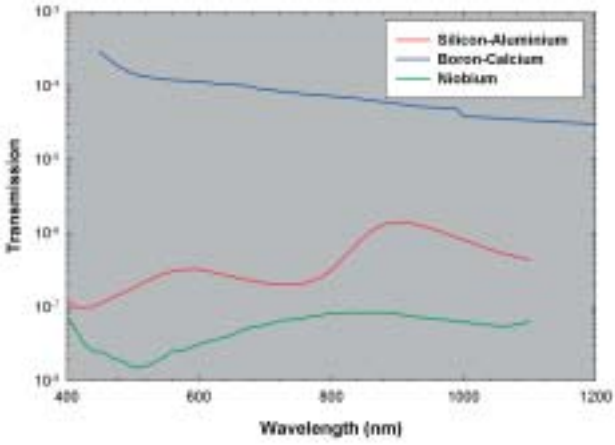

Figure 7.2 (above right). The measured optical transmission for the three filters described in Section 7.2.

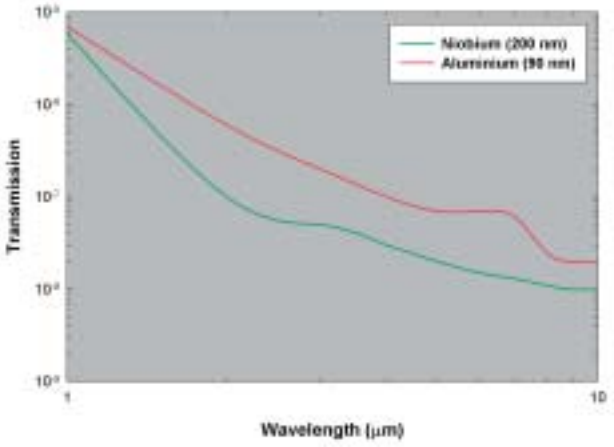

Figure 7.3 (right). The transmission through thin metal foils at NIR wavelengths.

7.3 NIR filters

Free-standing (mesh grid-supported) thin metal films are an effective means of significantly reducing the NIR flux – providing the filters are held close to the detector and kept at low temperature. Fig. 7.3 shows the transmission at 1-10 μm for two such films: a 200 nm-thick Nb film and a 90 nm-thick Al film. Of course, while the NIR attenuation is ~ 10^{-5}-10^{-8}, the soft X-ray response will be significantly reduced, as described in Section 7.2.

A different type of filter can be considered to avoid this loss in the soft X-ray. Metallic mesh structures have frequency-selective properties widely used in microwave and mm-wave technology that can be used for IR filtering. They can provide significant attenuation above a cut-off frequency governed by the geometry of the mesh while maintaining a high transparency at X-ray wavelengths.

Consider a free-standing square mesh as shown in Fig. 7.4a having thickness t ~ 300 nm, pitch a ~ 300 nm and hole width c ~ 260 nm. The filter response of such a mesh can be separated into different regions:

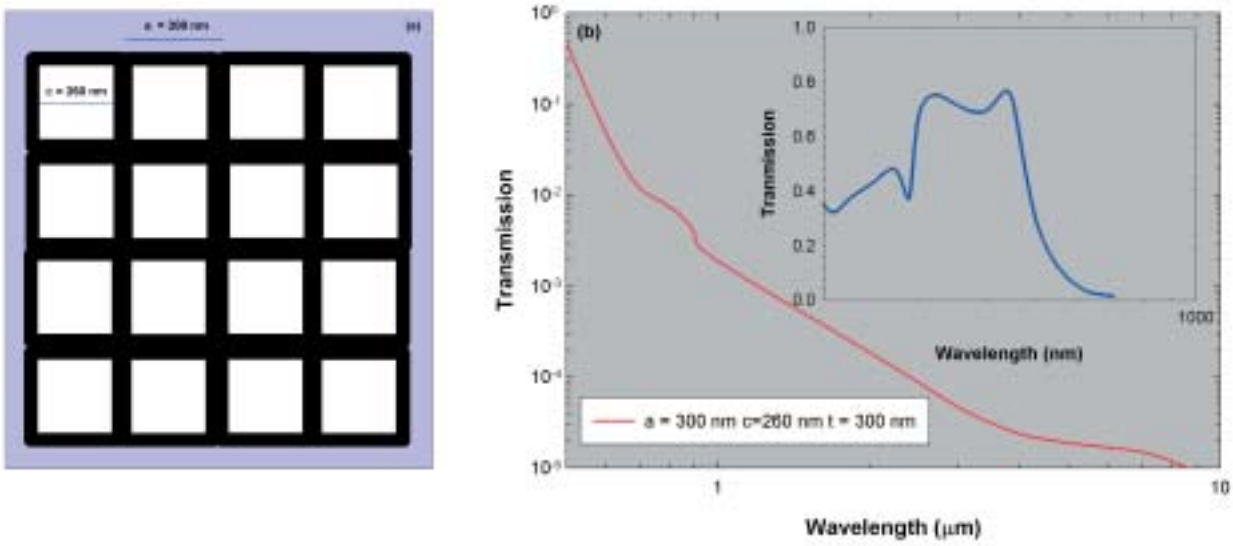

Figure 7.4. a: the schematic of an NIR filter grid. This is the simplest of many geometries that can be considered depending on the configuration of the detector and the required attenuation not only at NIR wavelengths but also into the optical. b: the attenuation of such a grid at NIR wavelengths for normal incidence.

— the cut-off region for wavelengths longer than 2*c* in which waves are attenuated. The thickness of the mesh defines the slope of the transmission curve above the cut-off wavelength. Increasing the thickness therefore can provide a greater attenuation above the cut-off wavelength;
— the transmission region for wavelengths longer than the mesh pitch. Here, high transmission can be expected;
— a grating lobe region (diffraction of the incident radiation). High transmission is possible but the photons are spread over different directions – possibly outside the detector field.

The relative importance and width of each region can be tailored by selection of the mesh parameters. Such a simple grid described above has a transmission at NIR wavelengths as low as 10^{-5} while maintaining X-ray transmission across the full XEUS energy band as high as 75%. Fig. 7.4b illustrates the expected NIR transmission through such a grid. The response of such mesh filters depends on the angle of incidence of the NIR emission. For oblique incidence, the behaviour of the mesh depends on the polarisation and is lower particularly for thicker structures. Fig. 7.4b refers to the case of normal incidence.

A number of different techniques can be considered for fabrication of such metal grids, including:

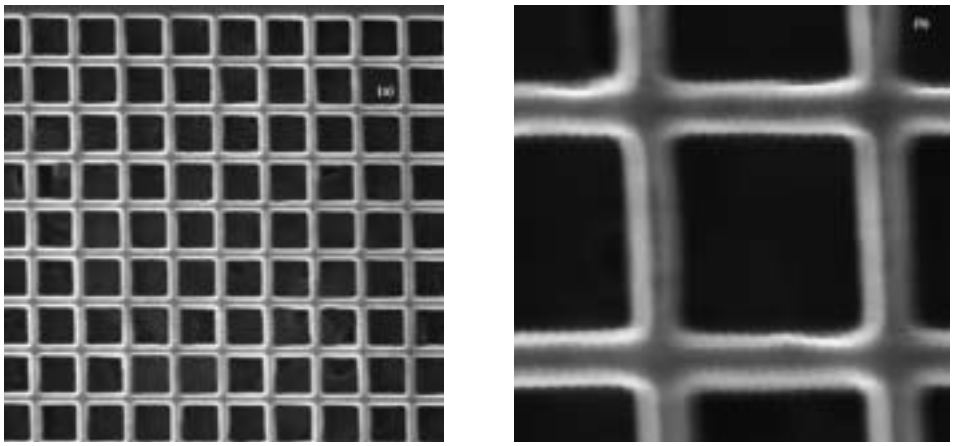

Figure 7.5. a: an Al mesh filter on a substrate produced by focused ion beam milling. b: close-up of part of this mesh.

— focused ion beam milling (FIB) of a metal film deposited on a suitable wafer substrate. The substrate is subsequently removed by reverse side FIB and chemical etching. Fig. 7.5 shows a grid prior to removal of the substrate. FIB has the advantage of being able to pattern a rather large area (~ 1 x 1 mm).
— electron beam lithography using a thin metal layer on a Si substrate followed by a thick layer of polyimide and thin resist. This is patterned by e-beam lithography and developed. A thin metal layer is then deposited which, after lift-off, acts as a mask for reactive ion etching in the polyimide. Electroplating can then be used to grow the high aspect ratio grid in the resist grooves on the thin metal layer between the substrate and the polyimide. The substrate is then dissolved to detach the filter.

8 The Technology Programme

8.1 Introduction

The XEUS focal plane is a challenging development in its own right and, as such, the various core technologies must be studied as early in the programme as feasible. This section indicates those core activities required to provide confidence that the performances assumed in the preceding sections can be achieved. A development plan should be formulated so that, as XEUS proceeds through its various phases, the technology development associated with the focal plane proceeds in parallel. An overall preliminary plan is shown in Fig. 8.1.

8.2 WFI

The wide-field focal plane instrument on XEUS requires major development because it is based on a rather new DEPFET detector. This is the most advanced semiconductor X-ray pixel detector. Considerable development is required for this novel detector in terms of the pixel size, readout speed and low-energy response. It is proposed to fabricate and test as early as possible specific prototypes of the WFI detectors. The main activities associated with this development programme are therefore:

— detailed evaluation of the design requirements;
— fabrication and test of DEPFET sensor element structures for comparison with the required specifications;
— development, fabrication and test of the three DEPFET control and signal processing chips;
— development of a test programme to assess the integrated test structures' performance against requirements;
— design, fabrication and test of larger-format integrated DEPFET demonstration devices.

Clearly, the main detector issues that need to be addressed are:

— optimum operating temperature;
— device noise;
— energy resolution;
— low- & high-energy response;
— device speed;
— device spatial resolution;

Status of development and proposed technology programme

The DEPFET detector is in an early stage of development. Prototypes have been fabricated and have proved all functional principles. While basic device physics research is still needed for the DEPFET arrays, the alternative pn-CCD frame store concept requires mainly technological research. The main technological issues are:

— qualification of a new 15-cm process;

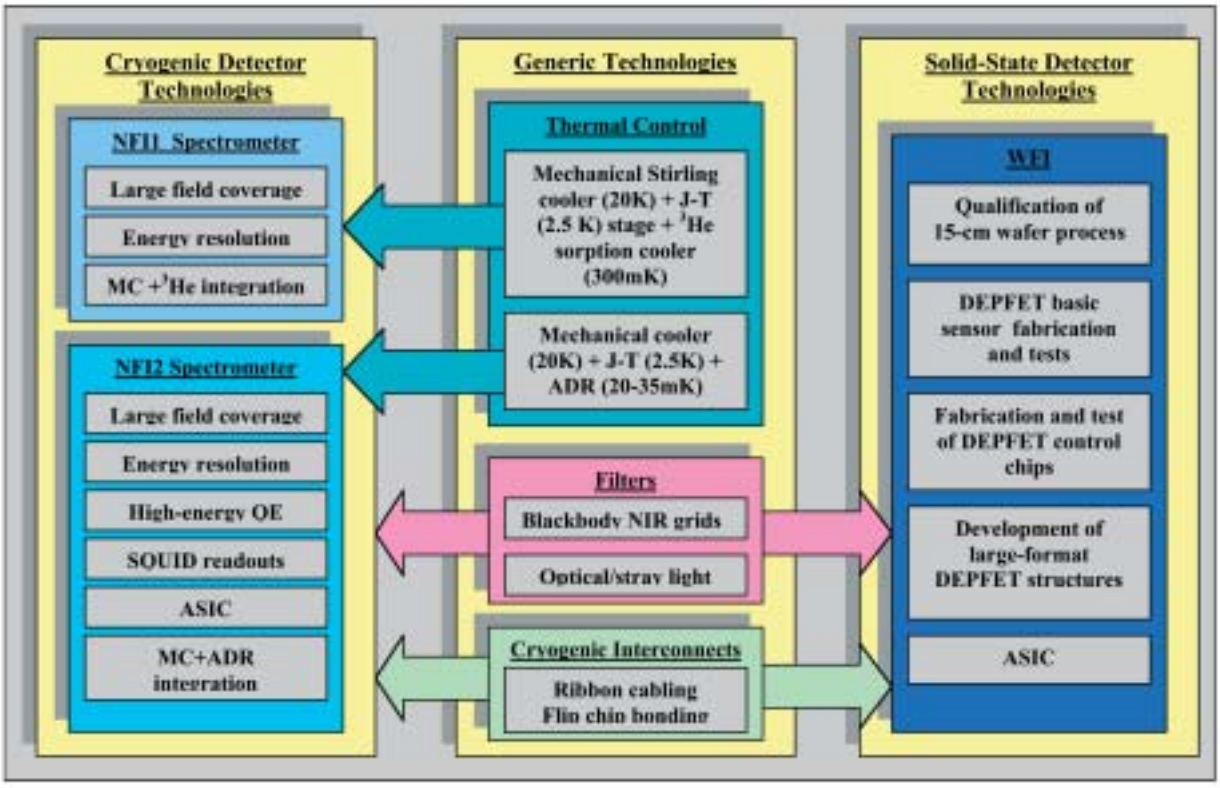

Figure 8.1. A preliminary technology plan highlighting the key technology steps required for the model payload comprising the XEUS focal plane.

— development of a double-layer metallisation process, without increasing surface and bulk leakage currents;
— large-area passivation, matched to the thermal requirements;
— development of adequate flip chip bonding techniques;
— improvements of the homogeneity of the planar process;
— mechanical mounting and cooling of the detectors

The main issues on the device physics level are:

— design optimisation;
— reduction of power dissipation;
— data reduction techniques after the ADC.

As a first step, matrices of 64 x 64 pixels with a pixel size of 50 μm will be studied. At the device level, all further areas of development can be outlined on the basis of these initial experimental results.

The problems of interconnections and cooling must also be solved in a sound way. As the spacing between the readout channels shrinks by a factor of two, wedge-bonding does not seem to be adequate.

8.3 NFI1

The NFI1 narrow-field focal plane instrument requires a further development effort because it is based on a large-format STJ detector. The main activities associated with the development are:

— demonstration of the performance of large-pixel devices appropriate to the XEUS PSF, particularly with respect to energy resolution and uniformity of response;
— demonstration that a low-energy response can be achieved in a large-format close-packed array, particularly down to the lower level threshold of ~ 50 eV;
— demonstration of the characteristics and performance of STJ arrays based on matrix readouts and their effect on the NFI1 design;
— demonstration of the characteristics and performance of 1-D and 2-D DROIDs and their effect on the NFI1 design;
— demonstration of the overall performance of a Ta-based large-format array coupled to a closed-cycle cooling system operated around 300mK with respect to thermal and electrical characteristics (including microphonics);
— development of larger-format Hf- or Mo-based arrays coupled to a closed-cycle cooling system operated around 30mK or 90mK, respectively;
— reduction/optimisation of the wiring and contact bonding for large-format arrays;
— NIR reduction optimisation.

8.4 NFI2

The NFI2 narrow-field focal plane instrument requires substantial development because it is based on the rather new but extremely promising TES sensor. The work involves primarily the development of a large-format array with a spatial resolution matched to the PSF of the XEUS optics, while maintaining good energy resolution and high efficiency up to 7 keV. It is proposed to fabricate and test specific prototypes of the NFI2 detectors as early as possible. The main activities associated with this development programme are therefore:

— establish a detailed design approach both at sensor and electronic readout level compatible with the overall requirements for the XEUS spectrometer;
— further develop single-pixel demonstration devices of the selected sensor technology;
— further develop and optimise SQUID-based electronic readout for single-pixel devices;
— demonstrate the required capability and performance of single devices when coupled to an optimised readout system;
— based on both initial design considerations and the performance of test devices, develop the design of a large-format array suitable for XEUS;
— develop prototype arrays;
— develop an array electronics readout system;
— demonstrate the required array performance.

8.5 Thermal control

Both narrow-field instruments require the development of a mechanical cooler with a base temperature of 2.5K. This is achieved in two stages: (i) a Stirling pre-cooler with a base temperature of 20K, (ii) a Joule-Thompson closed-cycle cooler to enable a temperature of 2.5K to be achieved. For NFI1, which is based on Ta STJs, requiring a base temperature of ~ 300mK, a ^{3}He sorption cooler is required. For NFI2, with a much lower temperature requirement, an ADR third stage needs to be coupled to the 2.5K stage to achieve a base temperature of 20-30mK.

The basic activities required are:

— further development of the existing 20K Stirling cooler coupled to the 2.5K Joule-Thompson stage to maximise the heat lift and minimise microphonics. The microphonics and induced vibrations are a major issue for the cryogenic detectors, and need to be addressed as soon as possible;
— coupling of the 2.5K cooler to a ^{3}He sorption cooler to achieve a cooling power of 20 mW at 350mK for ~ 15 h;
— system testing of a prototype NFI1 STJ Ta array coupled to a representative cooler;
— substantial development of an ADR coupled to the 2.5K cooler so as to achieve a base temperature of 20mK with a cooling power of 200 nW for a hold time of ~ 14 h;
— optimisation of the NFI2 cooler in terms of mechanical and thermal design.

9 Auxiliary Science Instrumentation

9.1 Hard X-ray Camera

Scientific case

Introduction

The introduction of imaging capabilities in the hard X-ray range (10-100 keV) with the use of focusing techniques (e.g. multi-layer optics) will provide access to a new observing window. Present instrumentation in this range is based either on collimated instruments or mask techniques. While imaging can be achieved with a mask-based instrument, the limiting sensitivity is always dominated by the background of the entire detector, giving a typical source detection limit of about 10^{-11} erg cm^{-2} s^{-1}.

With XEUS, an area of about 2000 cm^2 @ 30 keV is expected to be achieved with a point source concentrated in a spot of 5 arcsec (HEW). For a power-law spectrum with photon index of 1.7, the source detection limit in 100 ks (assuming a negligible background in the source region) would be roughly F (10-40 keV) = 10^{-15} erg cm^{-2} s^{-1}, i.e. 4 orders of magnitude lower than present instrumentation. A good continuum spectrum (i.e. about 100 counts in total) would be obtained in 100 ks for a source with F (10-40 keV) = 2 x 10^{-14} erg cm^{-2} s^{-1}. The full spectroscopic capability of the focal plane detector (energy resolution of 1 keV @ 60 keV) would be exploited for a source giving about 20 counts in each single resolution bin, corresponding to about F (10-40 keV) = 3 x 10^{-13} erg cm^{-2} s^{-1} for a 100 ks observation. These performances, already unique by themselves, when combined with the unprecedented capability of XEUS in the lower energy range, will open exciting prospects in several fields.

The obscured Universe and AGN

Deep X-ray surveys have resolved the X-ray background at around 1 keV into a population of discrete sources almost entirely composed of AGN. The energy density of the X-ray background peaks at ~ 30 keV, but only a fraction of this total energy density can be accounted for by the AGN population that dominates the soft X-ray background. On the other hand, we also know that many nearby AGN are heavily obscured and that the central engine is visible only at high energies. Models derived by adding the X-ray spectrum of a large number of absorbed AGN at different redshifts with various column densities succeed in reproducing the spectrum of the hard X-ray background. The total energy produced by AGN may be comparable to that generated by the stellar population, with the AGN output mostly hidden by obscuring regions. The hard X-ray capability of XEUS will be crucial in clarifying this scenario. The population of sources making up the X-ray background above 10 keV should be composed of heavily absorbed objects ($N_H > 10^{24}$ cm^{-2}). From the extension of the log N-log S from lower energies, most of the XRBs above 10 keV can be resolved by XEUS: in a typical 100 ks observation, hundreds of sources should be detected in the hard X-ray band in the 15 arcmin FOV available at 30 keV. Being obscured, their optical counterparts should be extremely faint, hence detection of the iron Kα line could provide the only method to determine their redshifts. The X-ray

redshift of this population of sources could be directly derived from the spectroscopy data gathered below 10 keV with one of the NFI instruments. For the brightest sources (F (10-40 keV) = 10^{-14} erg cm^{-2} s^{-1}), high-quality spectra catered by XEUS at 0.1-80 keV will enlighten the properties of the absorber and the central engine, up to z = 1 for a moderately bright source (L = = 10^{44} erg s^{-1}) and z = 3-5 for the more luminous AGN, leading ultimately to the cosmic history of the accretion power produced in the Universe.

Non-thermal emission from clusters of galaxies

In recent years, growing evidence for non-thermal emission in clusters of galaxies has accumulated. At hard X-rays, power-law tails dominating the thermal emission above ~ 10 keV have been detected by BeppoSAX in clusters such as Coma and A2256, with a luminosity of a few times 10^{43} erg s^{-1} in the 20-80 keV range. The most likely explanation is inverse Compton scattering of the cosmic microwave background by a non-thermal population of electrons, although alternative explanations have also been proposed. This population of electrons is also producing radio emission by synchrotron, in agreement with the observation of radio haloes in these sources. With the XEUS imaging capability in hard X-rays, it will be possible to clarify the origin of this component and understand the acceleration processes in the inter-cluster medium (ICM) by mapping the non-thermal emission in several clusters of galaxies, and measuring the spectrum of a hard X-ray component as faint as 10% of that observed in Coma up to z = 1. The study of the evolution of the 'non-thermal power' in clusters of galaxies with redshift will be very important in clarifying the formation processes of these structures, since the acceleration processes are likely connected with the formation of shocks generated during merging.

Non-thermal emission from SNRs and star-forming regions and the origin of cosmic rays

Hard X-ray observations over the past few years begun by ASCA and followed up by RXTE, BeppoSAX and, more recently, XMM, have demonstrated the presence of non-thermal X-ray emission arising from shells of young SNRs such as SN1006, Cas-A and Tycho. This emission, a power law with energy index 2 extending to several tens of keV, is attributed to synchrotron emission from electrons shock-accelerated to hundreds of TeV. The luminosity of this component in the 10-40 keV range is around 10^{35} erg s^{-1}. This finding is supported by the detection of TeV gamma-rays from two of these remnants. Another family of hard non-thermal X-ray sources was recently recognised in systems composed of a SNR interacting with a nearby molecular cloud. In one of these sources, the CANGAROO experiment has detected TeV photons that are thought to be produced by high-energy protons via the decay of π^0 (rather than by inverse Compton scattering of electrons as in the cases mentioned above). Since cosmic rays consist primarily of protons, this evidence would mean that the production of cosmic rays in our Galaxy could be conclusively linked to SN explosions, if this process is indeed present in most SNR. Hard X-ray observations could provide important information in this respect, because the population of protons should also produce hard X-rays through bremmsstrahlung with a

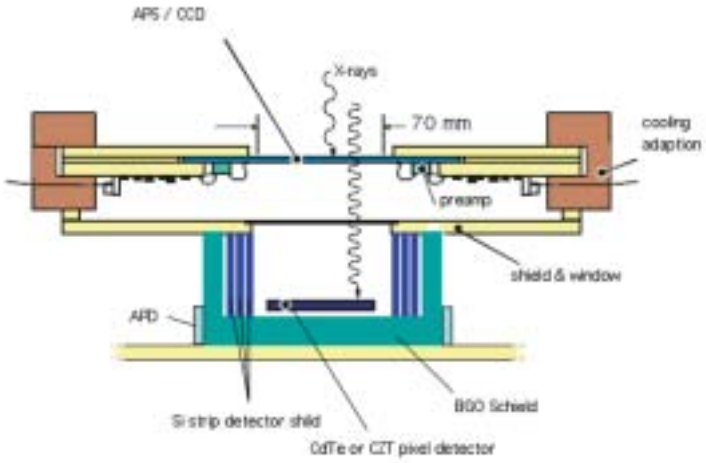

Figure 9.1.1. The HXC and WFI. The HXC will be placed below the WFI.

spectrum distinctly different from that attributed to synchrotron emission from electrons. Evidence of non-thermal power law emission has been found in two SNR-molecular clouds, with a flat shape ($\Gamma = 0$) consistent with that expected from proton bremmsstrahlung in a dense region. With the hard X-ray capability of XEUS, it will be possible to provide a census of the non-thermal properties of SNRs up to distances far beyond the boundary of our Galaxy, reaching out to M31.

Other topics

Probing the SN explosions

Hard X-ray images in the Ti^{44} lines at 68 & 78 keV in SNR, recently detected by BeppoSAX, will provide information about the explosion that formed them, since the amount of Ti^{44} synthesised depends sensitively on the explosion energy, asymmetries and mass cut. While it is expected that Integral will provide information about the total mass of the Ti^{44} (via observation of the line at 1157 keV), with the imaging and sensitivity capability of XEUS it will be possible to map the distribution of Ti^{44} in the SNR.

The hard X-ray properties of afterglows of GRBs

But for the first thousands of seconds after a GRB, no information on the hard (> 10 keV) emission of X-ray afterglows of GRBs is available. Particularly important in this respect is the long-term evolution of the X-ray spectrum at high energies. With the XEUS sensitivity, it will be possible to measure the hard X-ray spectral evolution for several weeks after the burst. Combined with the lower-energy capability, this will provide a spectral coverage spanning three orders of magnitude in energy, i.e. the same bandwidth from optical to X-rays. The temporal and spectral evolution of the continuum will provide important clues on the fireball evolution (jet *vs.* spherical expansion) and the environment in which it expands (interstellar

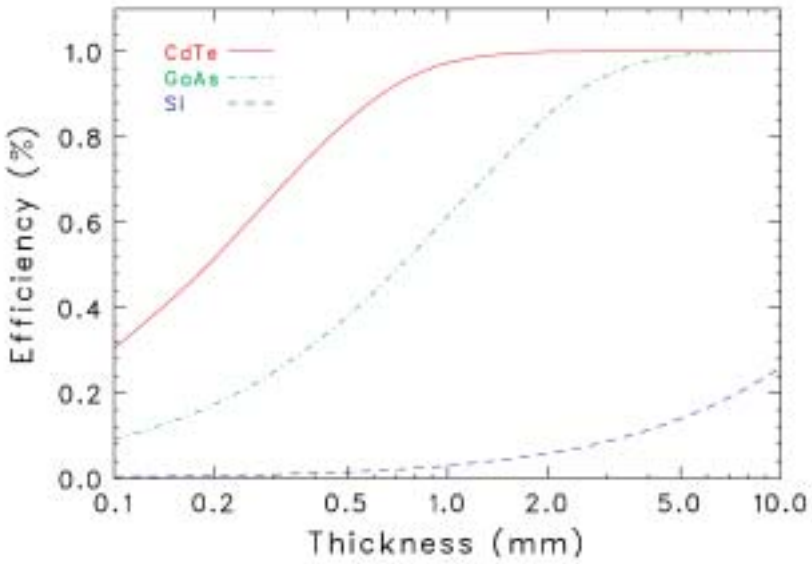

Figure 9.1.2. Detection efficiency for 60 keV gamma-rays with room-temperature semiconductor material. Mass-attenuation coefficients are used for the calculation.

medium *vs.* wind from massive progenitor), ultimately leading to the nature of the progenitor and the energy budget of these explosions.

Hardware implementation

A very high sensitivity in the 10-80 keV band will be achieved by employing a multi-layer, grazing incident hard X-ray telescope ('supermirror') in conjunction with a hard X-ray imaging detector. Since the supermirror is able to cover the energy range from ~ 0.2 keV up to 60-80 keV, the focal plane detector is required to cover a very wide energy band. One idea is to combine a fully depleted X-ray imaging device (soft X-ray detector) such as an active pixel detector and a pixelated CdTe detector as already proposed for the hybrid camera of the future Japanese NeXT mission. Soft X-rays will be absorbed in the soft X-ray detector, and hard X-rays will penetrate the CCD and be absorbed in the CdTe pixelated array. Pixel electrodes are formed on the CdTe surface and each electrode is bump-bonded to the readout electronics chip (ASIC).

A schematic design of the hard X-ray camera (HXC) is shown in Fig. 9.1.1, together with the soft X-ray detection part and the shield. In order to obtain an ultimate sensitivity for both soft X-ray and hard X-ray energy band, active shielding is important. For this, detectors should have fast timing resolution of 10-100 μs, such that the detectors can be vetoed when there is a hit in the active shield.

CdTe and CZT

The focal plane detector should have a sufficient efficiency at least up to 80 keV. Semiconductor detectors with high mass absorption coefficient seem

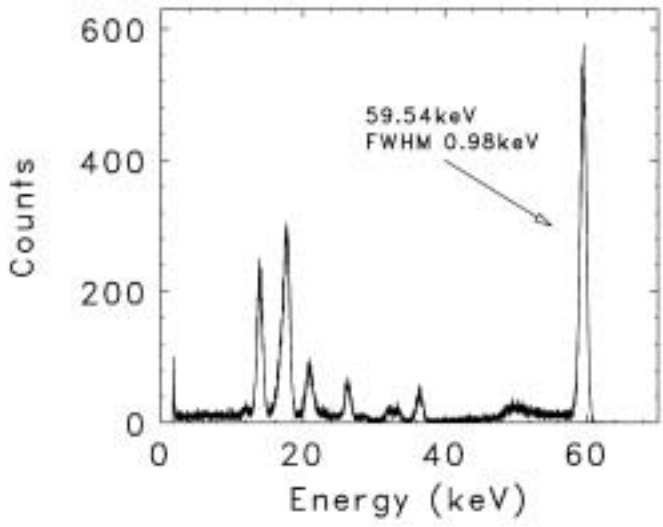

Figure 9.1.3. ^{241}Am spectra obtained with the CdTe diode detector operated at 20°C. The detector has a surface size of 2 x 2 mm and a thickness of 0.5 mm, with a guard ring surrounding the detection area. The time constant of the shaping amplifier is 0.5 μs.

to be the choice, since we need a fine position resolution of several 100 μm and a high energy resolution better than $\Delta E < 1$ keV. Among the range of semiconductor detectors available for hard X-ray detection, CdTe (and CZT) have a privileged position, because of their high densities and the high atomic numbers of their components, as well as wide bandgaps. Photoelectric absorption is the main process up to 300 keV for CdTe, compared with 60 keV for Si and 150 keV for Ge. Fig. 9.1.2 shows the efficiency of CdTe, Si and GaAs for a 60 keV photon as a function of the detector thickness. Even a detector with a thickness of 0.5 mm provides a good detection efficiency for the hard X-ray region overed by the XEUS supermirror.

Thanks to the remarkable progress in the technology of producing high-quality crystals of CdTe and CZT in the 1990s, large-area CdTe/CZT detectors are now available. The uniform charge transport properties of the wafer are a very important aspect for fabricating large-area strip or pixel detectors. A CdTe crystal grown by the Travelling Heater Method (THM-CdTe) would be one choice, because we can obtain a highly uniform wafer as large as 2 x 2 cm. Grain boundaries and Te inclusions, which degrade the spectrum, are very rare in the wafer. Fig. 9.1.3 shows the spectrum taken with the CdTe diode detector produced from a single crystal of CdTe. The detector is operated at room temperature (20°C).

CdTe pixel detector

The current goal for the CdTe or CZT detector to be used in the HXC is a pixel detector with both a fine position resolution of 200 μm and a high-energy resolution of better than 1 keV (FWHM) in the energy range 5-80 keV.

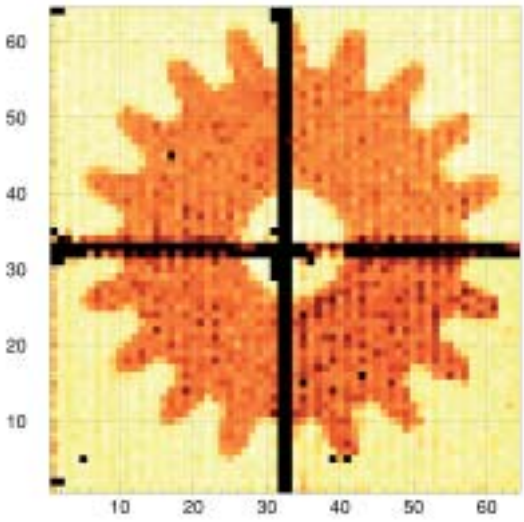

Figure 9.1.4. Radiograph of a toothed wheel obtained with a CdTe pixel detector developed under a collaboration between ISAS and Bonn University. The pixels are 200 x 200 μm. The 60 keV line from ^{241}Am was used to take an image.

In order to cover the field of view of the telescope, the detector should have an area of 16 cm^2. If the maximum energy obtained by the supermirror is up to 80 keV, the detector thickness of 0.5-1 mm is sufficient. With this thickness, we can apply sufficient bias voltage to collect the full charge produced in the device. Full charge collection is very important to reduce the low-energy tail often seen in the thick CdTe and CZT detectors. Fast timing of a few μs will be required for the active shielding, which is necessary to achieve a low background environment in space.

To realise fine pitch (finer than several hundred μm) CdTe and/or CZT pixel detectors, a readout system for more than 10 000 independent channels will be the key technology. A simple and robust connection technology needs to be established, because high compression and/or high ambient temperature would damage the CdTe and CZT crystal. Fig. 9.1.4 is a radiograpic image obtained with fine-pixel detectors developed under a collaboration between ISAS and Bonn University (D). The size of the pixels is 200 x 200 μm. They are directly bump-bonded to a 2-D photon counting ASIC (MPEC2) by using newly developed gold-stud bump-bonding technology. The development of the low-noise ASIC for pixel detectors by using deep sub-μm CMOS technology is now underway. The requirement for the power consumption is 200 μW per pixel.

As shown in Fig. 9.1.5, four detectors, each of area 2 x 2 cm, will be tiled to obtain a total 4 x 4 cm. Three ASICs will be mounted below the CdTe crystal to process the signal.

HXC characteristics	
Pixel size	200 μm
Minimum threshold	3-5 keV
Maximum energy	80 keV
Energy resolution (FWHM)	0.5-1 keV
Operating condition	0-20°C
Average count rate	500 s^{-1} for the entire array
Peak count rate	100 s^{-1} pix^{-1}
Time resolution	10 μs
Power	< 200 μW pix^{-1}

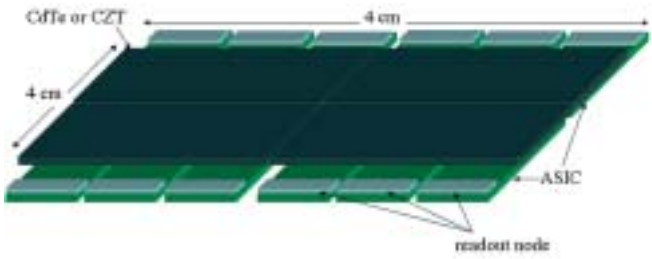

Figure 9.1.5. Schematic of the CdTe pixel detector for the HXC. Four detectors, each 2 x 2 cm, will be tiled. Three ASICs will be mounted below the CdTe crystal to process the signal.

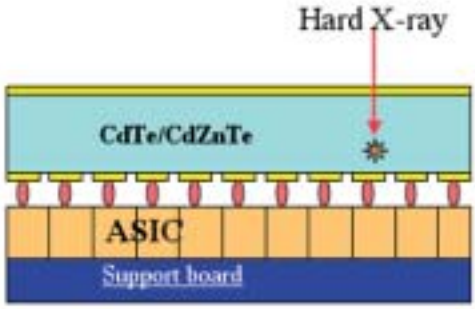

Figure 9.1.6. Schematic of the CdTe pixel detector.

HXC

Schematics for the HXC are shown in Figs. 9.1.5 and 9.1.6. Signals from the individual pixel electrode formed on the surface of the CdTe wafer is fed into the readout circuit built in the ASIC. The area of the circuit is the same as the pixel size of the CdTe detector. Each circuit consists of CSA, shaping amplifier, comparator and sample/hold. The trigger is generated by the OR signal made from outputs of comparators for all channels.

In order to achieve high sensitivity in the hard X-ray region, a low background environment is important. As shown in Fig. 9.1.1, Silicon Strip Detectors (SSDs) are proposed for the active shield. Silicon is low-Z material, so activated lines do not contaminate to the soft X-ray detector. In Fig. 9.1.1, an additional BGO shield surrounds the SSD and CdTe pixel. How K-escapes and L-escapes affect the background for both HXC and WFI need to be studied further.

If the high timing resolution and high energy resolution can be achieved for the soft X-ray detector, it will allow combination of the soft X-ray detector and the hard X-ray detector as a polarisation detector through Compton scattering. Compton scattering is modulated with polarisation at larger scattering angles. Since the Compton and photoabsorption cross-sections are equal in Si at 60 keV, polarisation measurements can be made at around this if there is a low energy threshold in the scatter for the low-energy detector. This combined use of APS and HXC will allow polarimetry to be performed from 40 keV to 70 keV. Compared with the low-energy polarimeter (Section 9.4), it will operate on a more limited number of brighter sources but many models predict that polarisation increases in the hard X-ray band, so these few measurements could be of the highest astrophysical interest.

9.2 Fast X-ray timing detector

Scientific case

Fast X-ray timing to probe general relativity in strong gravity fields

The X-rays generated in the inner accretion flows around black holes and neutron stars carry information about regions of the strongly curved space-time in the vicinity of these objects. This is a regime in which there are important predictions of general relativity still to be tested. High-resolution X-ray spectroscopy and fast-timing studies can both be used to diagnose the orbital motion of the accreting matter in the immediate vicinity of the collapsed star, where the effects of strong gravity become important.

With the discovery of ms aperiodic X-ray time variability (or so called quasi-periodic oscillations) from accreting black holes and neutron stars, and brightness burst oscillations in neutron stars, the Rossi X-ray Timing Explorer (RXTE) has clearly demonstrated that fast X-ray timing has the potential to measure accurately the motion of matter in strong gravity fields and to constrain masses and radii of neutron stars, and hence the equation of state of dense matter.

XEUS is designed to perform imaging and spectroscopic observations of the most distant X-ray sources to trace the origin and evolution of hot matter back to the early ages of the Universe. To achieve this goal, XEUS requires a huge collecting area. The same requirement applies to fast X-ray timing studies, for which extremely good photon statistics are needed. After the XEUS Munich workshop, testing general relativity in the strong field regime through sub-ms timing and spectroscopy of bright X-ray binaries was identified as an important scientific objective of the mission.

In view of its unprecedented mirror aperture, XEUS will provide a better-than order of magnitude improvement in sensitivity for timing studies over RXTE. XEUS will enable for the first time the testing of the most fundamental predictions of general relativity, such as frame dragging effects and fully relativistic periastron precession. In addition, XEUS will allow, in exquisite detail, the waveform of coherent brightness X-ray burst oscillations to be studied. The waveform is directly affected by gravitational light deflection and relativistic Doppler shifts, and yields direct constraints on the mass and radius of the neutron star, and hence the equation of state of its high-density core. The properties of the neutron star cores have been the subject of considerable speculation, and remain a major issue in modern physics. Similarly, the modelling of the waveform of the high-frequency quasi-periodic oscillations (which will for the first time be observed on their coherence time scales) can place important constraints on the mass and spin of the black hole.

A fast-timing capability on XEUS would also extend its field of applications, by allowing the study of the X-ray variability of a wide class of objects, such as low-mass X-ray binaries in external galaxies (owing to the zero background, kHz quasi-periodic oscillations could be detected up to around 20 keV for the brightest objects), accreting and isolated pulsars, accreting

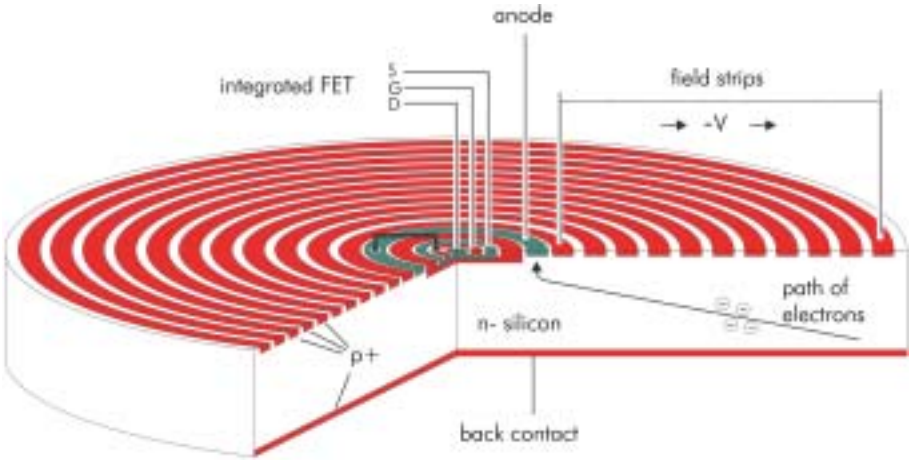

Figure 9.2.1. Cross-section of a cylindrical SDD. Electrons are guided by an electric field towards the small collecting anode at the centre. The first transistor of the amplifying electronics is integrated on the detector ship.

white dwarfs and X-ray transients (especially the so-called micro-quasars). Accretion and jet formation are crucial to understanding aspects of astrophysics from normal stars to super-massive black holes. The fast-timing capability can be combined with good energy resolution and broadband coverage to allow time-resolved spectroscopic observations. For instance, the space-time geometry close to black holes could be probed using variability in the Fe K line.

Science requirements

The science requirements derive from the ability of the fast-timing capability to observe the brightest X-ray sources in the sky, mostly X-ray binaries, either transient or persistent. Simulations using the current effective area of the mirrors show that the Crab would produce about 250 kcount s^{-1} and about 800 kcount s^{-1} in XEUS Phase-A and -B, respectively. Sco X-1, bright transients and X-ray bursts can be ten times brighter. This leads to a requirement to be able to handle up to 3 Mcount s^{-1} (Phase-A) and 10 Mcount s^{-1} (Phase-B). In addition, the arrival time of each photon should be recorded with a timing resolution of about 10 μs, the energy resolution of the detector should be around 200 eV (i.e. a factor of 10 improvement over current instrumentation for timing studies) and, finally, the detector energy range should cover the high-energy response of the mirrors (as timing signals tend to become stronger at higher energies).

Detector implementation

In the current XEUS detector baseline, the Wide-Field Imager has the highest count rate capabilities. However, even in the most optimistic case, it will be able to provide timing information only up to 500 kcount s^{-1} (by using a fast window mode). This means that an alternative solution should be considered.

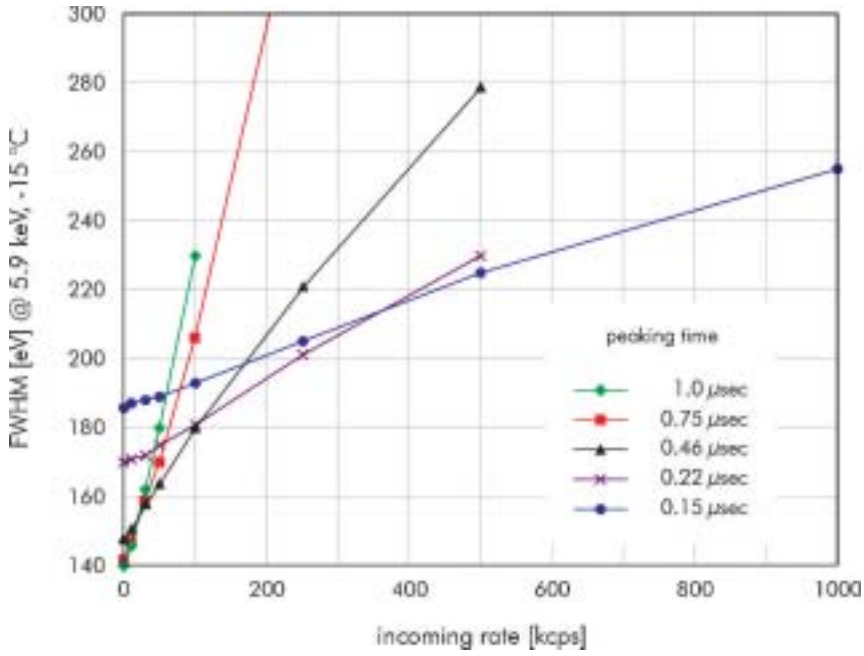

Figure 9.2.2. Energy resolution of a single SDD as a function of the incoming rate of photons for various peaking time constants (the shaping time constant of the amplifier is about half the peaking time). The fastest shaping time constant used in these measurements is 70 ns (50 ns is also possible), for which even at the highest incoming rate an energy resolution better than 260 eV is achieved.

Among the fast X-ray detectors currently available, Silicon Drift Detectors (SDDs) are the most promising. The SDD is a completely depleted volume of silicon in which an arrangement of increasingly negatively biased rings drive the electrons generated by the impact of ionising radiation towards a small readout node in the centre of the device. The time needed for the electrons to drift is much less than 1 μs. The main advantage of SDDs over conventional PIN diodes is their small physical size and consequently the small capacitance of the anode, which translates to a capability to handle very high count rates simultaneously with good energy resolution. To take full advantage of the small capacitance, the first transistor of the amplifying electronics is integrated onto the detector chip (Fig. 9.2.1). The stray capacitance of the interconnection between the detector and amplifier is thus minimised and, furthermore, the system becomes practically insensitive to mechanical vibrations and electronic pickup.

Even for 1 Mcount s^{-1}, using a very fast shaping time constant of 75 ns, energy resolution of less than 260 eV at 5.9 keV has been measured for a moderately cooled detector (–15°C). In Fig. 9.2.2, the energy resolution at 5.9 keV is shown as a function of count rate for different shaping times, and indicates that, for a count rate of 100 kcount s^{-1}, an energy resolution of better than 200 eV can be obtained.

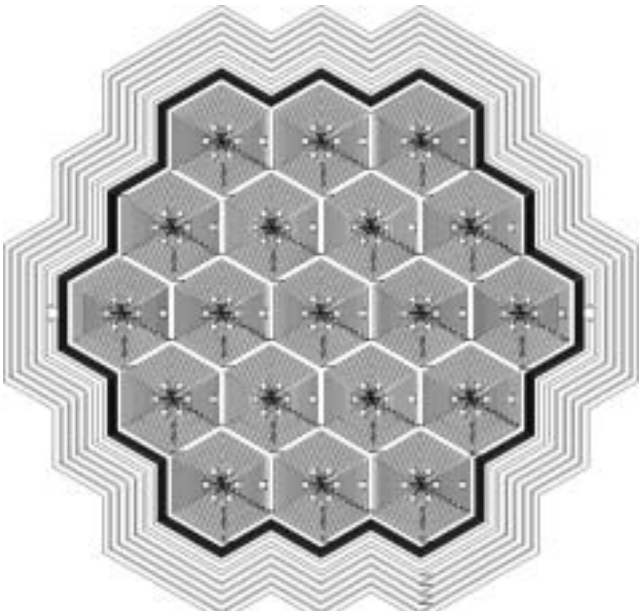

Figure 9.2.3. SDD array made of 19 hexagonal cells of 5 mm². The overall size of the detector is about 1 cm². Such a detector, operating out of focus, has capabilities matching the requirements of the XEUS fast-timing instrument.

For timing studies, dead time is always a critical issue. Dead time will include contributions from the signal rise time, the charge-sensitive amplifier and the shaping amplifier. The first two of these can be very short, and the limiting contribution is that of the amplifier, where a trade-off between speed and energy resolution is necessary. Shaping time constants as short as 50 ns have been found to be usable. This translates to a minimum feasible dead time of about 100 ns. Using currently available devices and pipelining techniques, the analogue-digital conversion stage is not a limiting factor at these speeds.

A 100 ns dead time per event corresponds to a 1% dead time for a source producing 100 kcount s^{-1}. To handle 1 Mcount s^{-1}, one must therefore distribute the focal beam over 10 pixels or so. The best and easiest solution could be a detector made of an ensemble of about 10 separate SDDs on a single wafer. Such SDD arrays already exist, as shown in Fig. 9.2.3. This detector should therefore be operated out of focus. For XEUS Phase-A, the out-of-focus distance is of the order of 15 cm. This could be accomplished either by a mechanical construction or by changing the distance between the detector and mirror spacecraft. Although this will require a careful study, both solutions appear to be feasible within the current XEUS mission design. The requirements in terms of real estate on the focal plane are not constraining, in particular because no complicated cooling systems will be

necessary. Finally, the SDD array could be implemented easily on the side of the wide field imager chip.

By observing bright X-ray sources, the detector will be exposed to high radiation doses, so its radiation hardness must be considered. The main limitation in the maximum acceptable dose arises from the JFET connected to the collecting anode on the back of the device. High-energy photons absorbed in the transistor region increase the amount of oxide charge and interface traps, thus reducing the charge carrier lifetimes and contributing to increase the leakage current. Laboratory measurements indicate, however, that a 300 μm-thick SDD survives a radiation dose of 10^{13} incoming high-energy photons (energies above 12 keV). This is equivalent to a continuous exposition of 3 yr at 10^5 photons s^{-1}. Similarly, the detector will be exposed to particles at a moderate rate (1-2 cm^{-2} s^{-1}). Again, the XMM-Newton EPIC PN cameras, which use similar detector technology, have not shown any loss of performance in space since launch. So, the device selected can be clearly considered as radiation-hard.

As mentioned above, a high-energy extension (above 40 keV) is proposed for the mirrors. SDDs are currently produced with thicknesses of up to 500 μm, which is adequate to cover the energy range below 10 keV. Although there are efforts to make thicker devices, the best match of the high-energy response of the mirrors will require the SDD array to be associated with a higher density detector located underneath. Among the potential high-energy semiconductor detectors, CZT or CdTe could be considered. Such detectors would both ensure the overlap in energy range with the SDD array, and provide a flat energy response up to around 100 keV and 10 μs timing resolution.

The goal is to send to the ground the time and energy information of every photon. For most sources, data compression will make this possible (within a 2 Mbit s^{-1} data rate) without compromising either time or energy resolution. For the very brightest sources, this can still be done with a restricted number of energy channels.

9.3 Extended field of view imager

Scientific case

Given the increased plate scale of the XEUS optics, there is a case to be made for an extension to the field coverage of the WFI, the prime goals being serendipitous science and extended-object work. A mosaic 'ring' of detectors around the inner APS array could accomplish this.

The formation of super-massive black holes is very probably an integral feature of the initial galaxy formation process. They should originate at high redshifts of $z > 5$, up to even 10. They are likely to have a luminosity in the 10^{43}-10^{44} erg s^{-1} range and the study of these, the first quasars, can be done only in the X-ray band. The study will aim to examine the evolution of these objects with redshift. Clearly, it is important to detect as many as possible in the deep looks that will be necessary to exploit the limiting sensitivity of XEUS at around 10^{-18} erg cm^{-2} s^{-1}.

At the same time, XEUS will also address the formation of the first galaxy groups, later to form clusters of galaxies. These groups follow the dark matter distribution resulting from inhomogeneities after the Big Bang, and can be recognised by spectral lines from the hot gas accumulating in the potential well created by the dark matter. The evolution of these groups with redshift is a key scientific aim.

WFI is the prime instrument for studies of the very high-redshift Universe, combining high efficiency with moderate energy resolution and a wide field of view. Because of the long focal distance of XEUS (50 m), the physical size of the focal plane is significantly larger than, for example, the CCD arrays of XMM-Newton. Because of the high throughput, the central region where pointing targets will be located requires the use of a fast counting detector, the APS, that allows high counting rates and a broad energy range coverage. The size of the APS is such as to cover a 7 arcmin square of the FOV. This is much larger than the FOV of the cryogenic imaging spectrometer, which is less than 1 arcmin, but is still much smaller than the XMM-Newton cameras, which cover a 30 arcmin-diameter FOV. As the XEUS mirror will have good off-axis performance, an extension of the FOV should be considered.

The mirror PSF degrades only 30% at a field off-axis angle of 10 arcmin, and where the effective area remains as high as 75% of the on-axis value. Given the expected performance of the XEUS mirror, the extension of the FOV to a diameter of 15 arcmin would more than double the number of exploitable scientific objects per deep field observation. Based on log N-log$S$ indices in the soft (0.5-2 keV) and hard (2-10 keV) bands of 0.6 and 0.4, respectively, we estimate that an increase in detectable sources by a factor 2 can be achieved in the hard band by extending the field diameter to ~ 12 arcmin, while the soft band source counts can increase by ~70%.

Detector technology

A possible way of implementing the FOV extension is a ring of large-area

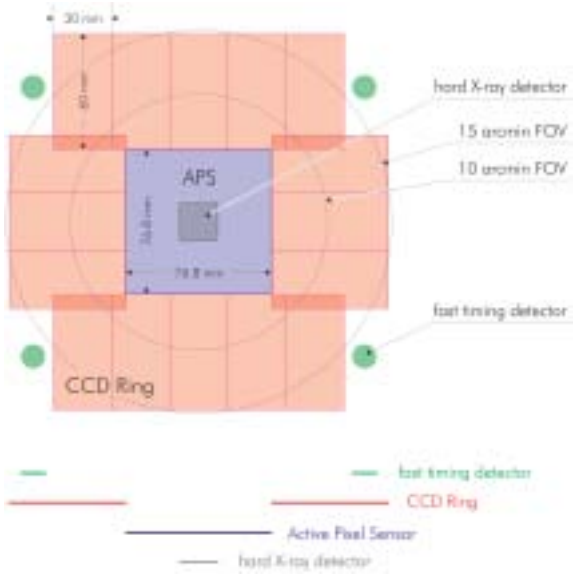

Figure 9.3.1. Focal plane geometry of the Extended Wide-Field Imager.

CCDs (either pn- or MOS-type) around the central imager, providing an independent subsystem to the WFI to fit within defined thermal, mechanical and electrical interfaces. The tentative scheme of the Extended Wide Field Imager (E-WFI) is outlined in Fig. 9.3.1.

Layout

Optimum layout of the focal plane will require an extensive study of the XEUS focal surface properties, the individual instrument characteristics, the system architecture to be used, and the size and associated yield of CCDs. The mosaic array options for the E-WFI are varied, with a trade-off to be made between a few ultra-large CCDs and many 'smaller' detectors, each having a higher production yield. One example is shown in Fig. 9.3.1; the baseline is a 3 x 6 cm detector format which is standard for contemporary astronomical detectors. In this example, the E-WFI detection ring is formed using a mosaic of 16 detectors. Overlapping sensitive areas of the detectors will minimise the dead space between adjacent modules. Other options for packaging might move the NFI1 and NFI2 instruments closer to the central APS detector, with the E-WFI filling the gaps between these structures.

Readout modes

The detectors of the E-WFI ring will not be performing a target-science role, so it is not planned to implement a variety of complex operating modes. The CCDs will be operated in one basic frame transfer mode routinely covering the whole of the outer field. A windowing mode similar to that used on XMM-Newton could be included for bright sources but would complicate the array's readout cycle.

9.4 Polarisation detector

Scientific case

Numerous predictions about the polarisation to be expected from most X-ray sources have been made. The polarisation may derive from:

— emission processes: cyclotron, synchrotron, non-thermal bremmstrahlung;
— scattering on aspherical accreting plasmas: discs, blobs, columns;
— resonant scattering of lines in hot plasmas;
— vacuum polarisation and birefringence through extreme magnetic fields.

This physics applies to most X-ray emitting objects. Polarimetry would add to energy and time two further observable quantities (the amount and angle of polarisation), constraining any model and interpretation. Predictions are available on many classes of sources:

X-ray pulsators

The polarisation of the cyclotron emission and the different scattering cross-section, in the presence of a strong magnetic field, produces a high degree of linear polarisation varying with energy and phase. With a pencil beam, the degree of polarisation will be anti-correlated with the luminosity, while for a fan beam it will be correlated. We will actually see the magnetic axis swinging around the rotation axis projected on the sky. All the geometry of the system will be completely frozen.

Isolated neutron stars

Radiation can be polarised when crossing an extreme magnetic field. Soft thermal X-ray radiation is produced by an atmosphere at T_{eff} = 0.3-3 x 10^6K. The opacity of a magnetised plasma depends on polarisation. While the effects of magnetic field on the spectrum are negligible the effects on polarisation are dramatic. The degree of polarisation (10-30%) depends on photon energy, T_{eff}, magnetic field and mass-to-radius ratio. In radio pulsars with thermal X-ray emission, phase resolved polarimetry will map the magnetic field. Even more dramatic effects are expected in Soft Gamma Repeaters, in the frame of the magnetar model.

Scattering in accretion discs and General Relativity effects

Intrinsically unpolarised radiation can be polarised by scattering, provided that scattering angles to the observer are selected by the system geometry. In accretion discs around compact objects, photons are Compton-scattered by high-energy electrons and the X-rays can be highly polarised either in the direction perpendicular to the major axis of the disc or in the direction parallel. The polarisation plane rotates continuously with energy because of light bending predicted by General Relativistic effects combined with the radial temperature distribution in the disc. This is a signature of a black hole.

AGN

In Seyfert galaxies and QSOs, the effects of scattering, kinematics and

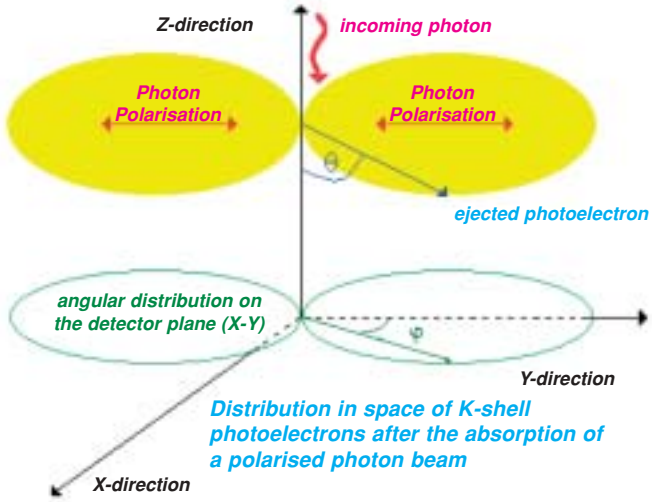

Figure 9.4.1. Physics of photoabsorption in a gas. The photoelectrons are ejected in directions that carry a significant memory of the photon's electric field.

General Relativity are all combined. Moreover, the disc/torus geometry produces significant selection effects in the scattering angles. Also, with a high accretion rate, the X-ray illuminated disc can be altered in its ionisation and temperature structure, producing polarised radiation at energies of 2-6 keV. Seyfert-2 galaxies can be highly polarised because the direct radiation is stopped by the edge-on disc and the detected radiation is mainly scattered. Blazar emission will be synchrotron at lower energies and is expected to be highly polarised (as in IR). At higher energies, inverse Compton will prevail and the degree of polarisation should decrease and the angle rotate. From the energy-resolved polarimetry, the geometry and energy distribution of the electrons within the jet can be studied.

To date, the use of Bragg polarisation for the Crab Nebula is a unique result.

Photoelectric polarimetry

Bragg polarimeters are dispersive and analyse a restricted angle at a time on a narrow band. Thomson-scattering polarimeters are not imaging and limited to $E > \sim 5$ keV. Thus conventional polarimetry would be limited to a handful of bright galactic sources at best.

The micropattern gas chamber (MPGC)

A recent development that improves significantly on the efficiency of previous techniques relies on the polarisation information in the photoelectron track imaged by a finely divided gas counter. Electrons ejected via the photoelectric effect are emitted in a distribution that peaks in the direction of the photon's electric field (Fig. 9.4.1).

The track of electron/ion pairs, produced by collisions in the gas, is straight

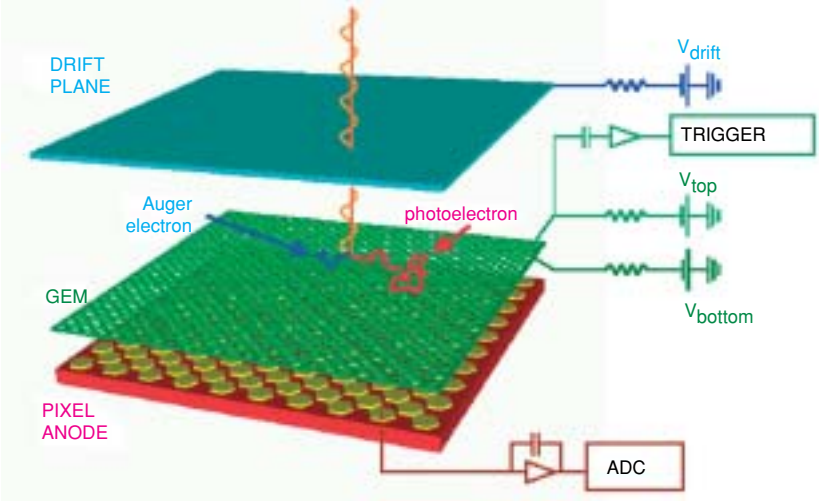

Figure 9.4.2. The Micropattern Gas Chamber. The photon is absorbed in the drift gap. The photoelectron track drifts to the Gas Electron Multiplier, which is formed by microscopic holes in a polyimide foil. A high E-field across the foil creates the high linear amplification and the charge is collected by a pixellated anode. On trigger from the GEM, the signals are processed to give the track image projected onto the detector plane.

at the beginning, where a good memory of polarisation is preserved, and random in the late part, where most of the energy is released. In a parallel drift field, the charges are translated to sensing elements of a detector. From the analysis of these signals, the original direction of the photoelectrons can be reconstructed. If the radiation is polarised, these tracks will be asymmetric.

The most promising implementation is the Micropattern Gas Chamber (MPGC). This comprises a thick detection/drift gas cell, a thin gas electron multiplier (GEM) stage, followed by a form of true 2-D readout encoder. Sensitivity to polarisation depends on the efficiency and the modulation factor. The first is mainly fixed by the gas composition, gas pressure and thickness of the absorption cell. The modulation factor depends on the track length versus the pixel size, on the gas composition and on the blurring of the track by diffusion in the drift. MPGC prototypes have been successfully tested. With suitable gas mixtures, modulation factors above 50% have been measured at 5 keV. The polarimeter needs no rotation – a substantial improvement over conventional techniques.

Detector technology

The polarimeter gas cell is based on conventional proportional counter technology. It includes a ceramic body and a thin window (50 μm Be or 0.9 μm polyimide). The drift field is defined by high voltage from an external supply fed through the body shaped by field-forming rings. Electrons drift to the GEM, which multiplies while preserving the shape of the track

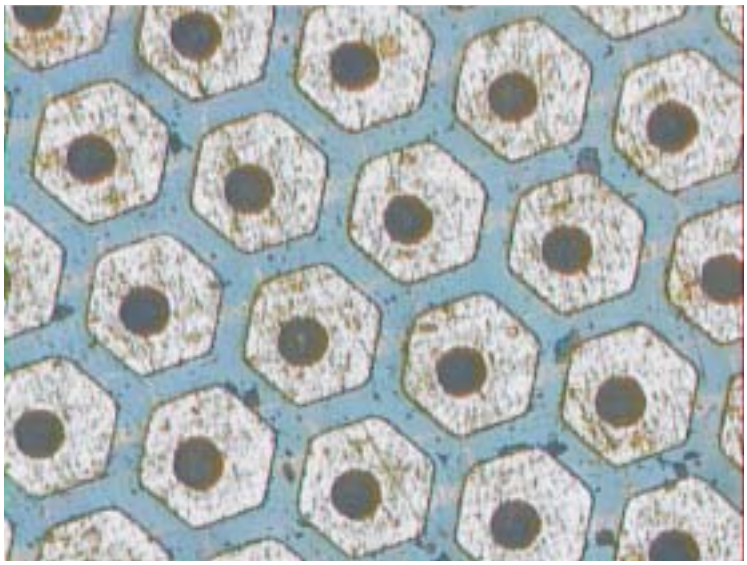

Figure 9.4.3. The readout plane of a prototype MSGC. The pads collect the charge that is routed through vias to lower layers.

(Fig. 9.4.2) and eventually collected by the detection plane covered with metallic pads disposed on an hexagonal pattern. Each pad is connected to an independent electronic chain.

In the current prototype the signal from the pads of 100 μm are collected through vias to different layers of a multi-layer advanced PCB and routed to ASIC VLSI chips. The largest detection plane developed so far includes 1024 pixels (3.6 mm diameter). Fig. 9.4.3 shows the pad plane of a prototype readout.

A new readout plane is under development, on 0.2 μm VLSI technology. The linear chain is below the projection of the 100 μm metal pad. Signals are multiplexed for serial routing. The capacity and the noise are very low. This technology allows for an almost indefinite replication with a consumption of ~ 1 W cm^{-2}. A chip of 16 000 pixels and 14 mm diameter (FOV of 1 arcmin) is foreseen.

Electronics

For each channel (Fig. 9.4.4), there is an independent charge preamplifier, a shaping amplifier, a discriminator and a signal holder. Hold signals are multiplexed and serially routed to the output. The signal from the GEM is preamplified and amplified and generates a logic pulse, which stores the time to tag the event. The GEM signal is also used to reject background (guard ring and pulse shape) and to evaluate the energy. The logic pulse from the GEM drives the demultiplexing, and A/D conversion of the signals from

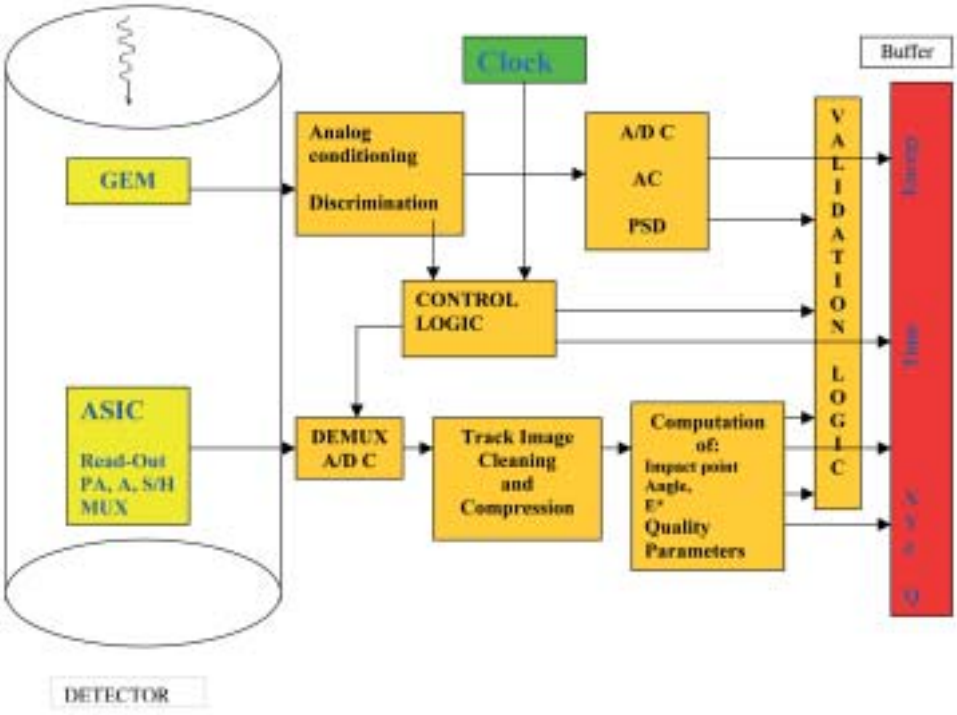

Figure 9.4.4. The readout and analysis electronics.

the ASIC, producing an image of the event. After removing isolated pixels (due to electronic noise or to non-X-ray events), the image is analysed by a processor that derives the impact point and the azimuth angle of the initial part of the track. Parameters related to the quality of the result (asymmetry of the track, goodness of fits, consistency of the energy computed by adding the charge of the pixels with the energy measured with the GEM, etc) will be computed. The data for the validated event are recorded on a buffer as a string with time, x, y, ϕ, E and quality parameters.

Baseline configuration

The main characteristics of the proposed polarimeter are:

Filling gas	Ne 80% DME 20% 1 atm
Conversion/drift gap	10 mm
GEM thickness	50 μm gold-clad Kapton
GEM hole	40 μm diameter, 60 μm pitch
Drift voltage (window to GEM)	–1000 V
GEM voltage	600 V
Readout pixel	100 μm
Pixel	16 000 on hexagonal pattern
Diameter	14 mm
FOV	1 arcmin

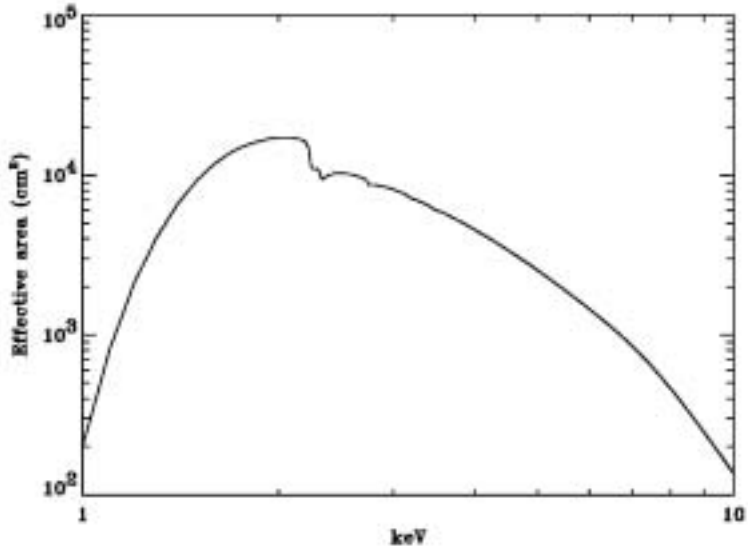

Figure 9.4.5. Effective area of the proposed device combined with XEUS1. Polarimetry can be performed above 2 keV.

With the aim of evaluating the capabilities of such a device, a conservative configuration is proposed. The optimal configuration of an MPGC for XEUS1 will result from complex study and testing, while for XEUS MSC2 a version more tuned to the low energies can be envisaged.

The polarimeter measures the absorption point with a precision of 2-3 pixels. This is well matched with the PSF of the optics and the blurring due to the finite absorption depth is negligible. The polarimeter fully exploits the quality of the optics, has good timing and the spectral resolution of a good proportional counter, suitable for energy-resolved polarimetry of continua.

The effective area of the MSC1 optics plus MPGC detector is shown in Fig. 9.4.5. By using modulation factors computed with a Monte Carlo code, we assume that the instrument has good polarimetric capabilities above 2 keV. The minimum polarisation detectable (99%) in 10^5 s on a set of AGNs with the proposed configuration is:

Cen-A	0.6%
NGC 4151	0.7%
NGC 5548	0.8%
MCG 6-30-15	1.2%
Circinus Galaxy	2.8%
IC 429A	0.7%
Fairall 9	1.6%
MK 501 (outburst)	0.5%
MK 421	0.7%
3C 273	0.9%

Acronyms

A/D	analogue/digital
ADC	analogue-to-digital converter
ADR	adiabatic demagnetising refrigerator
AGN	active galactic nuclei
AM	amplitude modulation
ANC	adaptive noise cancellation
AOCS	attitude and orbit control system
APD	active pixel detector
APF	additional positive feedback
APS	active pixel sensor
ASIC	application-specific integrated circuit
BGO	bismuth germanate
BSSR	Bias Supply & Signal Readout
CDF-S	Chandra Deep Field - South
CMOS	complementary metal oxide superconductor
CPA	chromic potassium alum
CSA	charge sensitive amplifier
CZT	cadmium zinc telluride
dADR	double adiabatic demagnetising refrigerator
DEPFET	depleted field effect transistor
DEPMOS	depletion mode metal oxide semiconductor
DGG	dysprosium gallium garnet
DMUX	demultiplexer
DROID	distributed readout strip detector
DSC	detector spacecraft
DSP	digital signal processor
E-WFI	Extended Wide-Field Imager
EMI	electromagnetic interference
FDM	frequency division multiplexing
FET	field effect transistor
FIB	focused ion beam
FLL	flux locked loop
FOV	field of view
FPGA	field programmable gate array
FTO	fellow traveller orbit
FWHM	full-width half maximum
GEM	gas electron multiplier
GOODS	Great Observatories Origins Deep Survey
GSFC	NASA Goddard Space Flight Center
GRB	gamma-ray burst

HDF	Hubble Deep Field (North & South)
HEW	half energy width
HK	housekeeping
HSC	^{3}He sorption cooler
HST	Hubble Space Telescope
HXC	hard X-ray camera
HV	high voltage
ICM	inter-cluster medium
ICU	Instrument Control Unit
I/F	intermediate frequency
ISS	International Space Station
JCMT	James Clerk Maxwell Telescope
JFET	junction field effect transistor
J-T	Joule Thompson
JWST	James Webb Space Telescope
LLNL	Lawrence Livermore National Laboratory (USA)
MIP	minimum ionising particle
MMS	Matra Marconi Space
MOS	metal oxide semiconductor
MOSFET	metal oxide semiconductor field effect transistor
MPGC	micropattern gas chamber
MSC	mirror spacecraft
MSSL	Mullard Space Science Laboratory (UK)
MUX	multiplexer
NCE	NFI camera electronics
NCH	NFI camera head
NDR	non-destructive redout
NFI	narrow-field instrument
NIR	near-infrared
NIST	National Institute of Standards and Technology
NTD	neutron transmutation doped
OCS	Orbital Control System
PA	preamplifier
PCB	printed circuit board
PCC	phase-change capacitor
PCM	phase-change material
PSD	position sensitive detector
PSF	point spread function
QE	quantum efficiency
QSO	quasi-stellar object

RAL	Rutherford Appleton Laboratory (UK)
RNDR	repetitive non-destructive readout
ROI	region of interest
RT	risetime
RXTE	Rossi X-ray Timing Explorer
SBT	Service des Basses Températures of CEA-Grenoble (F)
SCUBA	Superconducting Common User Bolometer Array
SDD	silicon drift detector
SEB	SQUID FLL Electronics Box
S/H	sample and hold
SIRTF	Space Infra-Red Telescope Facility
SN	supernova
SNR	signal-to-noise ratio; supernova remnant
SPT	stationary plasma thruster
SQUID	superconducting quantum interference device
SRON	Space Research Organization Netherlands
SSM	second surface mirror
STJ	superconducting tunnel junction
STP	standard temperature and pressure
TBD	to be determined
TDM	time division multiplexing
TES	transition edge sensor
THM	travelling heater method
UV	ultraviolet
VLSI	very large-scale integration
VTT	Valtion Teknillinen Tutkimuskeskus (State Technical Research Centre, FIN)
WFI	wide-field instrument
XEUS	X-ray Evolving Universe Spectroscopy mission
XRB	X-ray burster
XUV	extreme ultraviolet